UNIVERSITY OF CALIFORNIA,
IRVINE

Mixed-Mode Fracture and Fatigue Analysis of Cracked 3D Complex Structures using a 3D SGBEM-FEM Alternating Method

THESIS

submitted in partial satisfaction of the requirements
for the degree of

MASTER OF SCIENCE

in Mechanical and Aerospace Engineering

by

Sharada Bhavanam

Thesis Committee:
Distinguished Professor Satya N. Atluri, Chair
Associate Professor Lorenzo Valdevit
Assistant Professor Timothy J. Rupert

2014

TABLE OF CONTENTS

LIST OF FIGURES

LIST OF TABLES

ACKNOWLEDGEMENTS

First and foremost, I would like to express my sincere thanks to my advisor and the chair of my thesis committee Professor Satya N. Atluri. I would like to thank him for his continuous guidance and support in my research endeavor and it is an honor to learn under his guidance as well as to work as part of his research team.

I would also like to express my sincere thanks to Dr. Leiting Dong for his continuous guidance throughout the research process. I would like to thank him further for taking the time and effort to address the problems facing my research right away and giving me exceptional advice in achieving my goals for my research project. I would also like to thank my colleague Longgang Tian for letting me bounce ideas off of him concerning my research and also giving me excellent input on my research. Without the support and guidance from these incredible people, I would not have been able to write this thesis. A portion of the text on the analysis of cracked I-beam of this thesis is also a reprint of the material in the journal of *Theoretical and Applied Fracture Mechanics*. The co-authors Dr. Leiting Dong and Dr. Satya N. Atluri listed in this publication directed and supervised the research regarding the analysis of 3D complex structures using 3D SGBEM-FEM Alternating Method, which forms the basis for this thesis. Furthermore, I would also like to acknowledge my colleague and co-author Longgang Tian for his incredible effort and help on the published material as well as my other co-author Nam Phan for the contribution to the publication. Permission to use copyrighted material was granted by the publisher Elsevier Limited, please refer to the permission letter attached to the manuscript.

Last, but not least, I would especially like to thank my father, my mother and my sister for supporting me unconditionally and for teaching me the value of hard work during this entire process of earning my Master's Degree.

ABSTRACT OF THE THESIS

Mixed-Mode Fracture and Fatigue Analysis of Cracked 3D Structures using a 3D SGBEM-FEM Alternating Method

By

Sharada Bhavanam

Master of Science in Mechanical and Aerospace Engineering

University of California, Irvine, 2014

Distinguished Professor Satya N. Atluri, Chair

The aim of this thesis is to numerically evaluate the mixed-mode Stress Intensity Factors (SIFs) of complex 3D structural geometries with arbitrary 3D cracks using the Symmetric Galerkin Boundary Element Method-Finite Element Method (SGBEM-FEM) Alternating Method. Various structural geometries with different loading scenarios and crack configurations were examined in this thesis to understand the behavior and trends of the mixed-mode SIFs as well as the fatigue life for these complex structural geometries. Although some 3D structures have empirical and numerical solutions that are readily available in the open literature, some do not; therefore this thesis presents the results of fracture and fatigue analyses of these 3D complex structures using the SGBEM-FEM Alternating Method to serve as reference for future studies.

Furthermore, there are advantages of using the SGBEM-FEM Alternating Method compared to traditional FEM methods. For example, the fatigue-crack-growth and fatigue life can be better estimated for a structure because different fatigue models (i.e. Walker, Paris, and NASGRO) can be used within the same framework of the SGBEM-FEM Alternating Method. The FEM (un-cracked structure)/BEM(crack model) meshes are modeled independently, which speeds up the computation process and reduces the cost of human labor. A simple coarse mesh

can be used for all fracture and fatigue analyses of complex structures. In this thesis, simple coarse meshes were used for 3D complex structures, which were below 5000 elements as compared to traditional FEM, which require meshes where the elements range on the order of ~250,000 to ~10^6 and sometimes even more than that.

CHAPTER 1: INTRODUCTION

Most finite element numerical analyses concerning with the area of fracture and fatigue analyses of mechanical, civil and aircraft structures do not use SGBEM-FEM Alternating Method despite its many advantages. Commercial softwares that are available nowadays utilize traditional Finite Element Methods (FEM) or Extended Finite Element Method (XFEM) for the analysis of complex 3D structures with arbitrary 3D cracks. Current finite element methods require immense amounts of human labor in order to generate meshes for the analyses of fracture mechanics parameters (i.e. Mode I, Mode II, Mode III Stress Intensity Factors) and fatigue life estimations of these cracked 3D structures. The traditional finite element method (FEM) and the boundary element method (BEM) are still used today to compute the fracture mechanics parameters for these 3D structures with arbitrary 3D cracks. A publication by Cisilino and Aliabadi [1] and Mi and Aliabbadi [2] shows the traditional boundary element that was used for the evaluation of linear and non-linear fracture mechanics problems. In fact, some commercial codes are now keen on using the traditional BEM therefore outweighing the popularity of the traditional FEM [3]. It is important to note that these fracture mechanics parameters are crucial for the understanding of the damage tolerance analysis of complex structures as well as for assessing structural integrity of these complex structures [4].

The Symmetric Galerkin Boundary Element Method (SGBEM) was first proposed by Sergio Sirtori in 1979 for linear elastic analyses of simple structures, which proposes the symmetric formulation of Boundary Integral Equations (BIEs) [5], these symmetric BIEs are also shown in Chapter 2 for the analysis of the traction BIEs for the computation of SIFs. It wasn't until later on that the SGBEM would further be used heavily for fracture mechanics analysis of complex structures, earlier examples of the implementation of SGBEM was applied

only for simple plate structures. Before the implementation of SGBEM, traditional BEM-FEM coupling was used to compute the SIFs but the drawback of this as stated by Bonnet, Maier, and Polizzotto [3] is that it produces a non-symmetrical coefficient matrix. For most fracture mechanics analysis of 3D structures, BEM-FEM coupling was widely used to approach the 3D analysis of fracture and fatigue of cracked complex structures, an example of this type of coupling was used by Frangi and Novati for fracture mechanics analysis of various three-dimensional structures with cracks [6]. Another important feature of the SGBEM-FEM Alternating Method is that it has better convergence properties compared to BEM-FEM coupling because the BEM-FEM coupling uses the standard method of collocation approach as outlined by Hsiao et al [7] and [8].

It should be noted that even though SGBEM is gaining popularity, there was no implementation of the coupling of SGBEM-FEM Alternating Method until recently. One of the few recent publications that use the coupling of SGBEM-FEM Alternating Method for analysis of cracks in three-dimensional anisotropic media is outlined by Rungamornrat and Mear [9]. Although there are a few publications regarding the SGBEM-FEM Alternating Method, but nonetheless more research on the evaluation of fracture and fatigue analysis of complex structures with cracks are considering this approach for straightforward computational simplicity.

Before computing the stress intensity factors and determining the fatigue life of a structure, it is important to understand how the global structure and the crack configuration are modeled and meshed. When modeling the mesh for the 3D crack as well as for the un-cracked global structure, the two are modeled and meshed independently. Meshing the 3D structure with a crack present would require constant re-meshing as the presence of a crack would require one

to refine and update meshes and this is one of the problems that the SGBEM-FEM Alternating Method takes into account thereby making the computational process a bit more simpler. Modeling the FEM and BEM meshes independently proves to be advantageous as it saves computational time, cost and increases the speed of outputting numerical results. The arbitrary 3D crack could be planar, non-planar, surface or embedded crack in the global structure. Several examples of different crack configurations in complex 3D structural geometries are presented in the numerical results section of this thesis. The crack surface is modeled using the SGBEM and is discretized using an 8-noded quadrilateral boundary elements whereas the global un-cracked structure is modeled using 10-noded tetrahedron Finite Elements.

The main advantage of using SGBEM for modeling cracks is that it is actually easier to create a boundary element mesh separately for the crack and avoid treating sharp corners instead of going through the complicated effort of creating a mesh for a cracked 3D structure using the traditional FEM which would mean hours of local mesh-refinement at the crack fronts for fracture and fatigue analysis. Although the traditional BEM for crack modeling has certain beneficial advantages, it is also important to consider the downsides of the traditional BEM. One of the downsides of using the traditional BEM for the crack modeling is that there is the presence of non-symmetrical coefficient matrix as well as the application of hyper singular boundary integral equations [10]. This is where the SGBEM proves to be very convenient because the SGBEM has a symmetrical coefficient matrix of the system of equations [3] unlike traditional and dual BEMs [1,2] because SGBEM uses non-hyper singular boundary integral equations thereby making it much more desirable for modeling cracks and estimating fatigue-crack-growth.

In order to address the pressing downside of the traditional BEM, the SGBEM takes care of boundary integral equations of elasticity in the Galerkin weak form unlike the method of

collocations that is used to satisfy the boundary integral equations of the traditional BEM [7,8]. It should be noted that the SGBEM also uses weakly singular kernels [11], which are then removed through a mathematical transformation (which is explained in the theory section of the thesis) so the boundary element matrices can be integrated using the Gaussian quadrature rule.

The advantage of using the SGBEM-FEM Alternating Method is that it alternates between the crude FEM solution of the un-cracked global structure and the SGBEM solution for the small region enveloping the arbitrary 3D crack or simply put, the local cracked subdomain [12]. Traditional FEM is not accurate for modeling cracks and crack growth because it uses simple polynomial interpolations by approximating the stress and strain singularities using polynomial FEM shapes [13]. As mentioned earlier, the crack surface is modeled and discretized using 8-noded quadrilateral boundary elements but also the crack itself is modeled as a distribution of displacement discontinuities [12]. To model the crack and the crack growth efficiently where the traditional FEM fails to do so, embedded-singular elements were developed by Tong, Pian and Lasry [14] and Atluri, Kobayashi and Nakagaki [15]. Quarter-point singular elements developed by Henshell and Shaw [16] and Barsoum [17] were used for modeling the crack front and the crack tip to compute the stress intensity factors at the crack front for each crack step increment. Furthermore, an SGBEM 'super element' was developed by authors Dong and Atluri [18-21] for the direct coupling of SGBEM and FEM in fracture and fatigue analysis of complex 3D structures [13], which enables faster computational results in matters of seconds whereas traditional FEM software will take days. All the numerical examples studied in this paper were modeled by using a simple PC with an i7 core processor, this shows the simplicity of employing the SGBEM-FEM Alternating Method for fracture and fatigue analyses of complex 3D structures on simple PCs instead of using multi-parallel computing systems.

As stated earlier, when using the SGBEM-FEM Alternating method for the analyses of fatigue life and fracture mechanics parameters, a crude mesh was developed for both the crack configuration and for the un-cracked global structure. Unlike traditional FEMs, which require very refined meshes, the SGBEM-FEM Alternating Method does not require refined meshes but nonetheless refined meshes can still be used for SGBEM-FEM Alternating Method and the numerical results will still be accurate. Refined meshes were used for several 3D structures in this thesis but the main idea was to model a complex 3D structure by using simple FEMs and model the crack singularities by using SGBEMs so the computational time and effort required can be reduced greatly for the fracture and fatigue analyses of these structures [13].

In this thesis, several complex 3D structural geometries with different crack configurations were studied and the stress intensity factors were computed for the crack front at each crack step increment for each of the structural geometries. Fatigue crack growth and fatigue life were analyzed by using Paris Law in conjunction with SGBEM-FEM Alternating Method to study the damage tolerance of specific structures. For some 3D structures, empirical solutions and experimental results were provided in the open literature and these results were compared with the numerical results obtained from SGBEM-FEM Alternating Method thus validating the advantages of using the SGBEM-FEM Alternating Method for the analysis of complex 3D structures with arbitrary 3D cracks. Consequently, for other 3D structures, there were neither empirical solutions nor experimental solutions available in the open literature; hence the numerical simulations that are presented in this paper are to serve as a reference for future studies regarding the understanding of fracture and fatigue analyses of 3D complex structures with arbitrary 3D cracks.

CHAPTER 2: THEORY AND FORMULATION OF THE SGBEM-FEM ALTERNATING METHOD

Unlike the traditional and dual BEMs, which are characterized by hyper singular boundary integral equations which results in a non-symmetrical coefficient matrix, the SGBEM is characterized by weakly singular symmetric Galerkin boundary integral equations which were developed by Han and Atluri [22,23] with the application of non-hyper-singular boundary integral equations which were developed by Okada, Rajiyah and Atluri [24,25] thereby resulting in a symmetrical coefficient matrix. Like said before, SGBEM-FEM Alternating method alternates between the crude FEM solution and the SGBEM solution of the crack by imposing residual stresses at both the global and local boundaries hence the solution to the original problem is achieved by superposing the solution for each individual sub-problem as shown in Figure 2.1 [21].

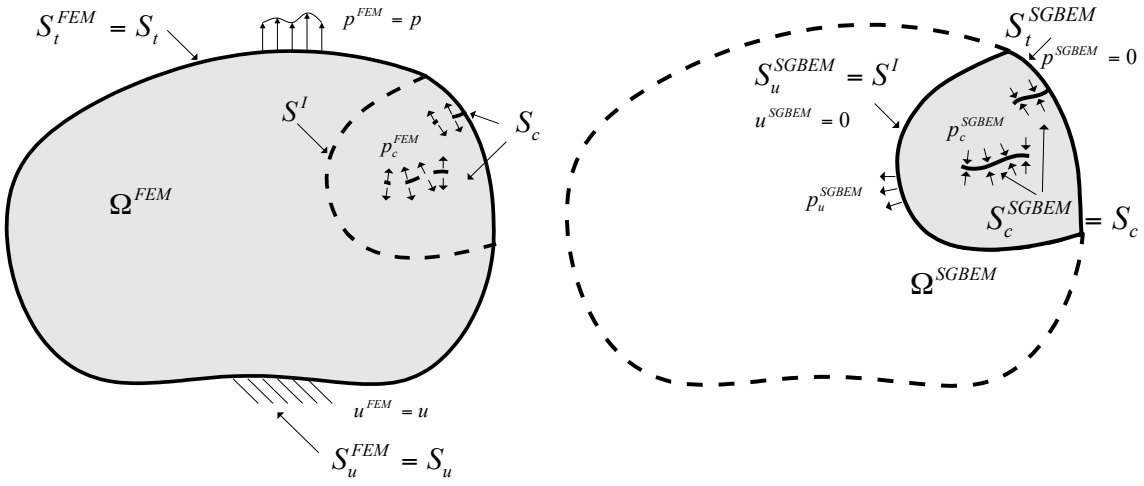

(a) (b)

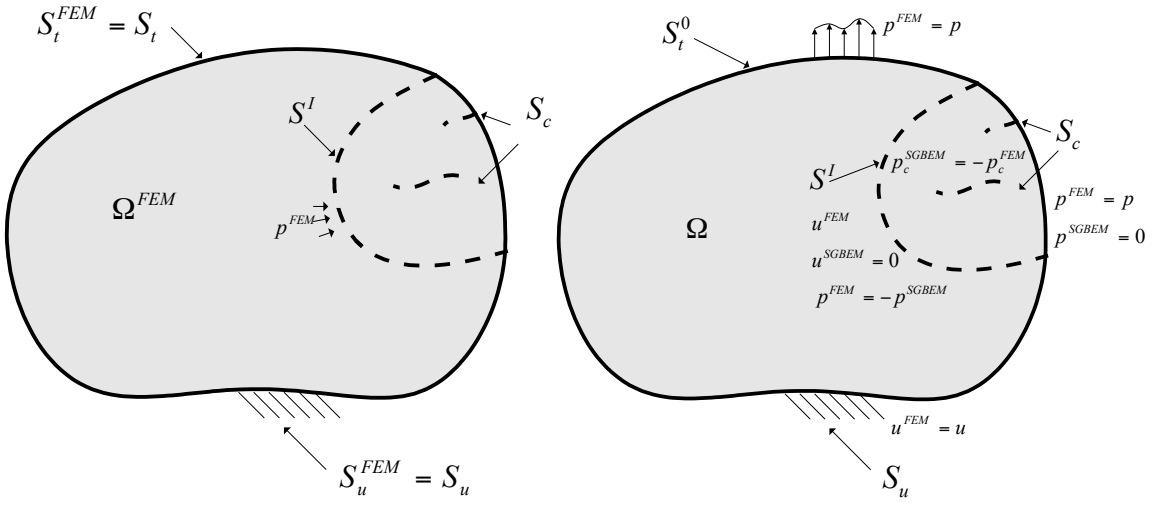

(c) (d)

Figure 2.1 Superposition Principle for SGBEM-FEM Alternating Method: (a) un-cracked body modeled by simple FEM, (b) local domain with arbitrary cracks modeled by SGBEM, (c) residual stresses on the FEM model, (d) alternating solution for the original problem.

To compute the displacements and tractions, Han and Atluri [22] developed 3D weakly-singular symmetric Galerkin boundary integral equations for the displacements and tractions for a domain of interest with a source point **x** and the target point ξ as shown in Figure 2.2.

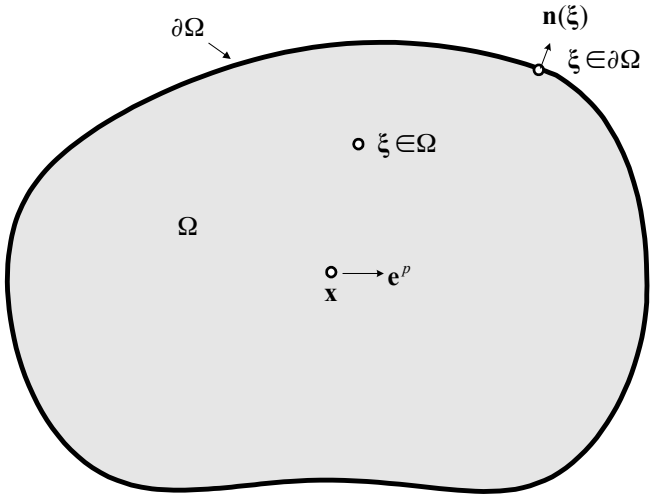

Figure 2.2 The solution domain with source point x and target point ξ.

The displacement boundary integral equation is shown below:

$$\begin{aligned}
&\frac{1}{2}\int_{\partial\Omega} v_p(\mathbf{x})u_p(\mathbf{x})dS_x \\
&= \int_{\partial\Omega} v_p(\mathbf{x})dS_x \int_{\partial\Omega} t_j(\xi)u_j^{*p}(\mathbf{x},\xi)dS_\xi \\
&+ \int_{\partial\Omega} v_p(\mathbf{x})dS_x \int_{\partial\Omega} D_i(\xi)u_j(\xi)G_{ij}^{*p}(\mathbf{x},\xi)dS_\xi \\
&+ \int_{\partial\Omega} v_p(\mathbf{x})dS_x \int_{\partial\Omega} n_i(\xi)u_j(\xi)\varphi_{ij}^{*p}(\mathbf{x},\xi)dS_\xi
\end{aligned} \tag{1}$$

In turn, the corresponding traction boundary integral equation is shown as the following:

$$\begin{aligned}
&-\frac{1}{2}\int_{\partial\Omega} w_b(\mathbf{x})t_b(\mathbf{x})dS_\mathbf{x} \\
&= \int_{\partial\Omega} D_a(\mathbf{x})w_b(\mathbf{x})dS_\mathbf{x} \int_{\partial\Omega} t_q(\xi)G_{ab}^{*q}(\mathbf{x},\xi)dS_\xi \\
&- \int_{\partial\Omega} w_b(\mathbf{x})dS_\mathbf{x} \int_{\partial\Omega} n_a(\mathbf{x})t_q(\xi)\varphi_{ab}^{*q}(\mathbf{x},\xi)dS_\xi \\
&+ \int_{\partial\Omega} D_a(\mathbf{x})w_b(\mathbf{x})dS_\mathbf{x} \int_{\partial\Omega} D_p(\xi)u_q(\xi)H_{abpq}^{*}(\mathbf{x},\xi)dS_\xi
\end{aligned} \tag{2}$$

where D_a is the surface tangential operator:

$$\begin{aligned}
D_a(\xi) &= n_r(\xi)e_{rsa}\frac{\partial}{\partial\xi_s} \\
D_a(\mathbf{x}) &= n_r(\mathbf{x})e_{rsa}\frac{\partial}{\partial x_s}
\end{aligned} \tag{3}$$

The weakly-singular kernels functions u_j^{*p}, G_{ab}^{*q}, φ_{ab}^{*q}, and H_{abpq}^{*} that are shown above in the boundary integral and the traction boundary integral equations (i.e. Eqs. (1), (2)) were derived in detail in the paper by Han and Atluri [22]. Furthermore, a symmetric system of equations can be obtained as shown in Eq. 4 by applying Eq. (1) to S_u for the given displacements and by applying Eq. (2) to S_t for the given tractions as depicted in Figure 2.3 below.

$$\begin{bmatrix} \mathbf{A}_{pp} & \mathbf{A}_{pq} & \mathbf{A}_{pr} \\ \mathbf{A}_{qp} & \mathbf{A}_{qq} & \mathbf{A}_{qr} \\ \mathbf{A}_{rp} & \mathbf{A}_{rq} & \mathbf{A}_{rr} \end{bmatrix} \begin{Bmatrix} \mathbf{p} \\ \mathbf{q} \\ \mathbf{r} \end{Bmatrix} = \begin{Bmatrix} \mathbf{f}_p \\ \mathbf{f}_q \\ \mathbf{f}_r \end{Bmatrix} \tag{4}$$

These variables **p**, **q**, **r** in the symmetric matrix denote the unknown tractions at S_u, unknown displacements at S_t and unknown displacement discontinuities at S_c as shown below in the solid with arbitrary cavities and cracks [13].

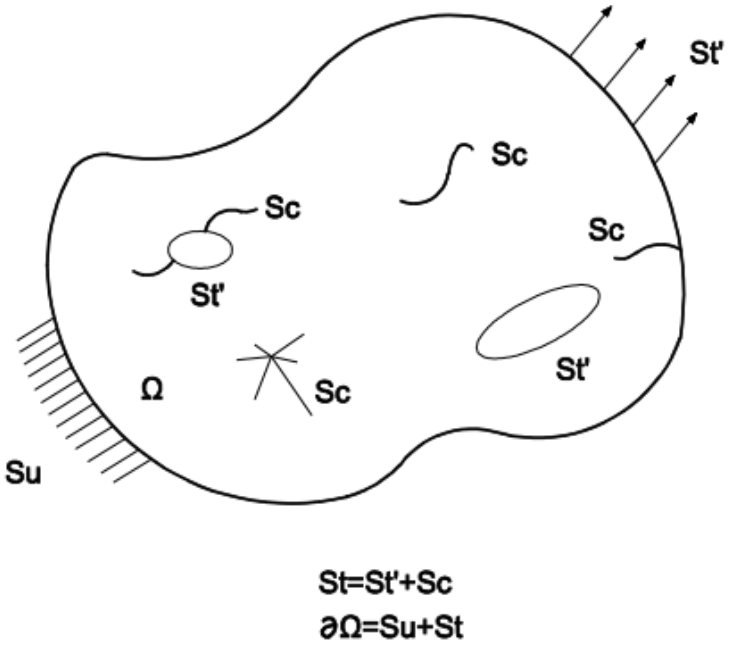

Figure 2.3 Solid with arbitrary cavities and cracks.

Once the displacements and tractions are computed at the boundary using the equations (1) to (4) mentioned above, the stress, strain and displacements at any point in the domain can be computed by using the non-hyper singular boundary integral equations developed by Okada, Rajiyah and Atluri as stated earlier [24,25]. There are two ways to compute the stress intensity factors and each method is just as effective as the other one. One of the methods was presented in detail from the paper by Nikishkov, Park and Atluri [12], the stress intensity factors can be

computed using the displacement discontinuity at the crack-front elements due to the singular quarter-point boundary elements at the crack face. The other way is that since the boundary integral equations are both path-independent and domain-independent integrals, therefore these boundary integral equations (Eqs. (1) & (2)) can also be used to compute the stress intensity factors. The following equations (Eqs. 5-7) shown below are used to compute the fracture mechanics parameters (i.e. mixed-mode stress intensity factors K_I, K_{II} and K_{III}) for linear elastic problems [12] for the numerical examples analyzed in this thesis.

Mode I Stress Intensity Factor: K_I

$$K_I = \frac{E}{(1-\nu^2)} \frac{u_3}{4\sqrt{\frac{2r}{\pi}}} \tag{5}$$

Mode II Stress Intensity Factor: K_{II}

$$K_{II} = \frac{E}{(1-\nu^2)} \frac{u_2}{4\sqrt{\frac{2r}{\pi}}} \tag{6}$$

Mode III Stress Intensity Factor: K_{III}

$$K_{III} = \frac{E}{(1+\nu)} \frac{u_1}{4\sqrt{\frac{2r}{\pi}}} \tag{7}$$

where E is Young's modulus, ν is Poisson's ratio, r is the distance from the point to the crack front, $u_1, u_2,$ and u_3 are the components of displacement discontinuities at points at the crack surface in a local crack front coordinate system and K_I, K_{II} and K_{III} are the mixed-mode stress intensity factors. Figure 2.4 shows the local crack front coordinate system used for the computation of the stress intensity factors, as shown below, the x_1 axis is aligned with the crack front coordinate system whereas the x_3 axis is normal to the crack surface.

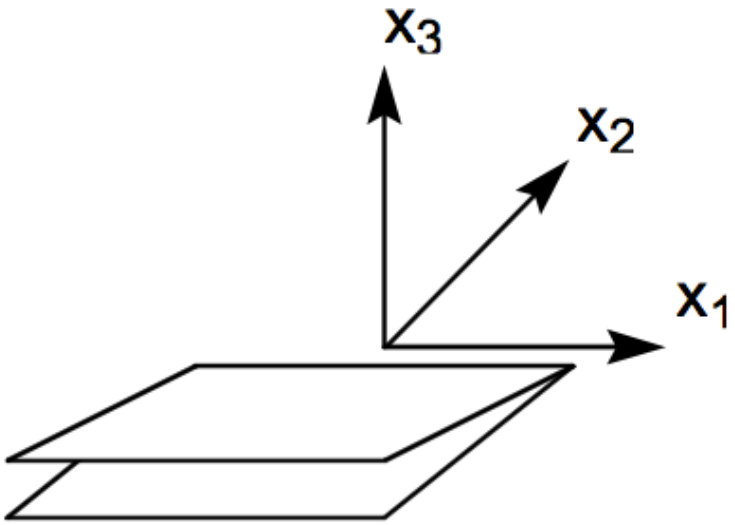

Figure 2.4 Local crack front coordinate system.

After computing the stress intensity factors, the fatigue life of the structure can also be predicted. One of the main advantages of SGBEM-FEM Alternating method is that since the FEM model and the crack model (BEM) are modeled independently, only the crack model will be changed when modeling the fatigue-crack-growth. Unlike other finite element model programs, for the SGBEM-FEM Alternating method, to model the fatigue growth of a crack, the crack-growth is modeled by adding a layer of additional elements at the crack-front to the existing crack model. Furthermore, the direction and magnitude of the crack advancement can be determined using the *J*-integral vector because the ranges of the *J*-integral components can be expressed in terms of the ranges of the stress intensity factors or typically the effective stress intensity factor ΔK_{eff} [2].

In the following section, which outlines the numerical examples analyzed using the SGBEM-FEM Alternating method, the Paris Law was mainly used to model the fatigue growth of a crack in a complex structure. The SGBEM-FEM has the capability of not only using just the Paris law to model the fatigue crack growth but also the NASGRO and Walker model to analyze

the fatigue crack growth in 3D complex structures. Even though the SGBEM-FEM Alternating Method cannot be employed for multi-scale large simulations but it is just as effective as current FEM programs that are used today for many computational solid mechanics problems.

CHAPTER 3: NUMERICAL EXAMPLES STUDIED BY USING THE SGBEM-FEM ALTERNATING METHOD

3.1 Quarter-Elliptical Crack in T-Butt Joint Subjected to either Normal or Shear Loading

The T-butt joint is widely used in many mechanical, civil and aircraft structures. The geometry and specifications of the T-butt joint analyzed in this thesis are clearly detailed in Table 3.1 and Figure 3.1. In this numerical example, the joint is subjected to either normal loading or shear loading which is applied to only on the top surface of the vertical plate attachment with a height H. The T-butt joint has the following material properties: Young's modulus of $E = 210{,}000\ N/mm^2$ and Poisson's ratio of $\nu = 0.30$. A quarter-elliptical crack is present in the corner where the bottom plate and the vertical plate are adjoined, this is also known as a weld root crack, see Figure 3.1. The quarter-elliptical crack has depth a and length c. A weld toe is formed when adjoining the two plates with the same width; hence this type of joint is known as a single-fillet welded joint with a weld angle θ and a weld leg L as shown in Figure 3.1. The joint is fixed at both ends of the horizontal base plate and the changes in stress intensity factors are analyzed by varying the different geometrical parameters for the T-butt joint.

Four geometrical parameters are varied for the joint and their effects on the stress intensity factors are analyzed in detail. The parameters that are varied are the following: variation of a/A (crack depth ratio), variation of a/c (crack shape ratio), variation of L/A (weld leg ratio), and variation of θ (weld angle). In the following subsections, numerical data and numerical plots obtained by the SGBEM-FEM Alternating Method are presented for each of these different parameters and their effects on the mixed-mode stress intensity factors.

As shown in Figure 3.1, the normal stress σ_{yy} acts in the upward y-direction and is applied on the top surface of the vertical attachment plate. For the case of shear loading, the

shear stress σ_{xy} was resolved in to a force F_{shear} for computational simplicity and applied on the top surface of the vertical plate, therefore the shear force will act in the x-axis direction. Each stress case is studied independently along with varying the four geometrical parameters mentioned above, the numerical results are presented in the subsections for both stress cases.

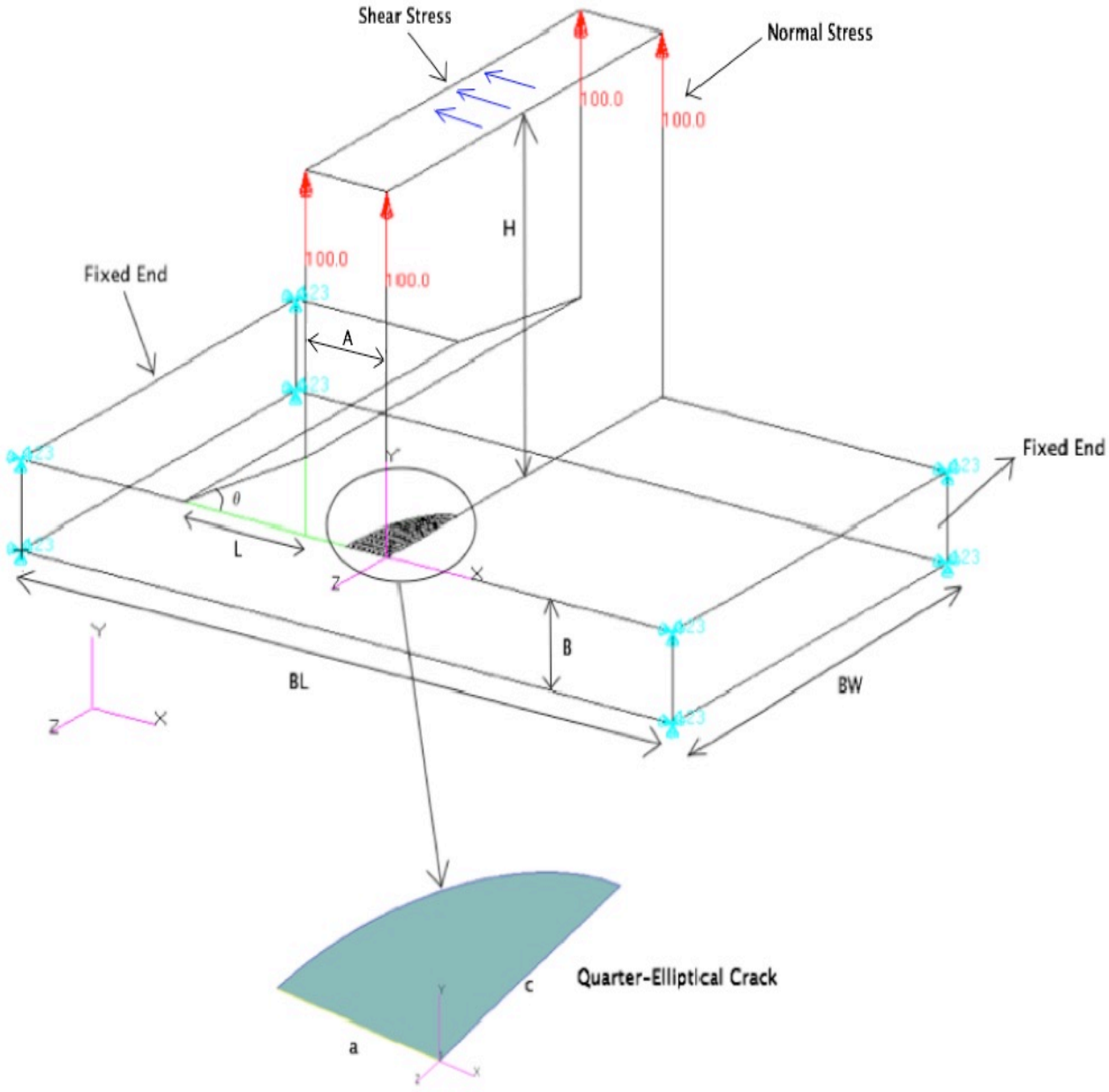

All dimensions in [mm]

Figure 3.1 T-butt joint with normal/shear loading.

Table 3.1 Dimensions for the T-butt joint with either normal stress or shear stress loading.

Dimension of the T-butt joint: units in [mm] (Refer to Figure 3.1)	
Horizontal Base Plate Length--***BL***	160
Horizontal Base Plate Width--***BW***	100
Vertical Attachment Plate Thickness--***A***	20
Horizontal Base Plate Thickness--***B***	20
Height of Vertical Attachment Plate--***H***	80

3.1.1 The effect of varying the crack depth ratio a/A (Normal Stress Loading)

The normal stress is applied on the top surface of the vertical attachment plate, which is $\sigma_{yy} = 100\ MPa$. In this section, five different crack depth ratios were studied for each of the different crack shape ratios and the effects of these parameters were studied on the mixed-mode stress intensity factors. The five crack depth ratios that were tested are the following: *a/A* = 0.01, 0.03, 0.10, 0.30 and 0.50. As *a/A* increases, the stress intensity factors also increase and this behavior is depicted in the plots shown below. Certain parameters were kept constant while *a/A* was changed. The weld angle θ was set to 60 degrees and the weld leg ratio *L/A* was set to 1.5, making the weld leg *L* = 30 mm. Figure 3.2 shows the finite element mesh of the structure with these fixed parameters as well as the Boundary element mesh for the crack surface model.

Five crack shape ratios (*a/c*) were studied ranging from *a/c* 0.2 to 1.0. Since the crack depth varies, the crack length also varies as it is dependent on the crack depth. Table 3.2 shows the dimensions of the of the crack surface models that were constructed for each corresponding crack depth ratio *a/A* for each of the crack shape ratio *a/c*. For example, for a crack depth ratio of *a/A* = 0.10 and with a crack shape ratio of *a/c* = 0.4, the crack depth is *a* = 2 mm and crack length is *c* = 5 mm.

Table 3.2 Crack surface dimensions for each crack depth ratio *a/A* with varying *a/c.*

Fixed Parameters: $\theta = 60°$, *L /A = 1.5*											
a/c		0.2		0.4		0.6		0.8		1.0	
Units: *a, c* [mm]		*a*	*c*	*a*	*c*	*a*	*c*	*a*	*c*	*a*	*c*
a/A	0.01	0.20	1	0.20	0.50	0.20	0.33	0.20	0.25	0.20	0.20
	0.03	0.60	3	0.60	1.5	0.60	1	0.60	0.75	0.60	0.60
	0.10	2	10	2	5	2	3.33	2	2.5	2	2
	0.30	6	30	6	15	6	10	6	7.5	6	6
	0.50	10	50	10	25	10	16.7	10	12.5	10	10

In Figure 3.2, the finite element mesh is shown for this specific case and the crack surface mesh is also shown. Note that the crack surface mesh will vary because the dimensions of the quarter-elliptical crack are changing for the different crack shape ratios along with crack depth ratios; therefore the crack configuration presented in Figure 3.2 is for a specific *a/A* case and it is shown as an example of how the quarter-elliptical crack is modeled. The finite elements for the global structure are modeled using 10-noded tetrahedron elements. For this specific case of geometry, the FEM structure is modeled using 3907 10-noded tetrahedron elements. The crack surface is modeled independently with 8-noded quadrilateral boundary elements. Please refer to Table 3.3 for the number of boundary elements used for each crack shape ratio configuration given the crack depth ratio. Note that there is not much change in the number of BEM elements used for different crack configurations as it is not required to refine meshes, which is one of the advantages of using the SGBEM-FEM Alternating method.

Table 3.3 FEM/BEM elements for each crack depth ratio *a/A* with varying *a/c.*

FEM Elements: 3907, BEM Elements shown for each case						
a/c		0.2	0.4	0.6	0.8	1.0
a/A	0.01	96	127	167	147	173
	0.03	96	127	161	145	173
	0.10	96	127	161	147	173
	0.30	96	127	161	145	173
	0.50	96	127	161	147	173

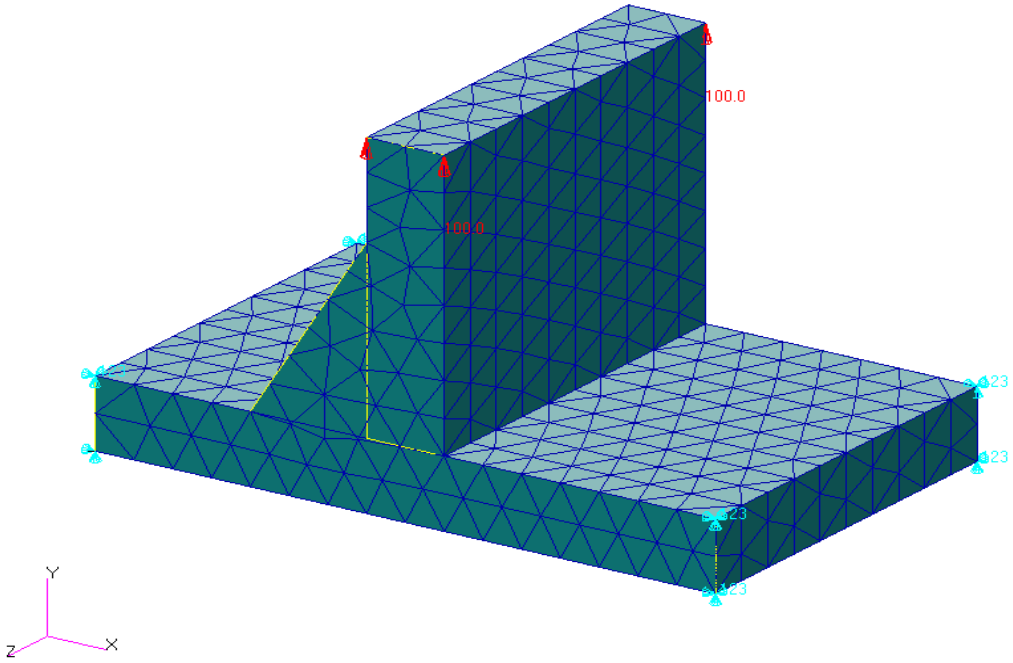

(a)

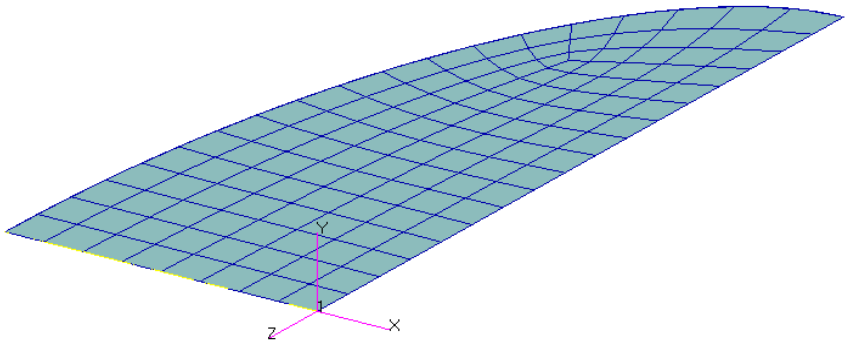

(b)

Figure 3.2 (a) Finite element mesh for the un-cracked structure modeled with 3907 10-noded tetrahedron elements, (b) Boundary element mesh for crack surface modeled with 8-noded quadrilateral elements, elements vary for different crack configurations, refer to Table 3.3.

The following plots shown below depict the mixed-mode stress intensity factors plotted against the crack depth ratio *a/A* for the various crack shape ratios. By observing the mode I SIF behavior, for an increasing crack depth ratio *a/A*, the SIFs tend to increase for the different crack shape ratios. For smaller crack shape ratios, the curve is steeper compared to the larger crack shape ratios as shown in Figure 3.3. Tables 3.4, 3.5 and 3.6 show the numerically obtained mixed mode stress intensity factors for each crack depth ratio *a/A* for different crack shape ratios *a/c*.

Table 3.4 Mode I SIFs for crack depth ratio effect *a/A* for normal stress loading.

$K_I\ [MPa \cdot \sqrt{mm}]$						
a/c		0.2	0.4	0.6	0.8	1.0
a/A	0.01	167.40	146.49	133.46	125.47	118.06
	0.03	319.23	261.53	236.10	220.47	203.32
	0.10	616.82	499.74	427.17	379.64	351.18
	0.30	864.06	687.83	580.93	530.23	482.51
	0.50	1005.20	726.86	595.18	510.19	455.39

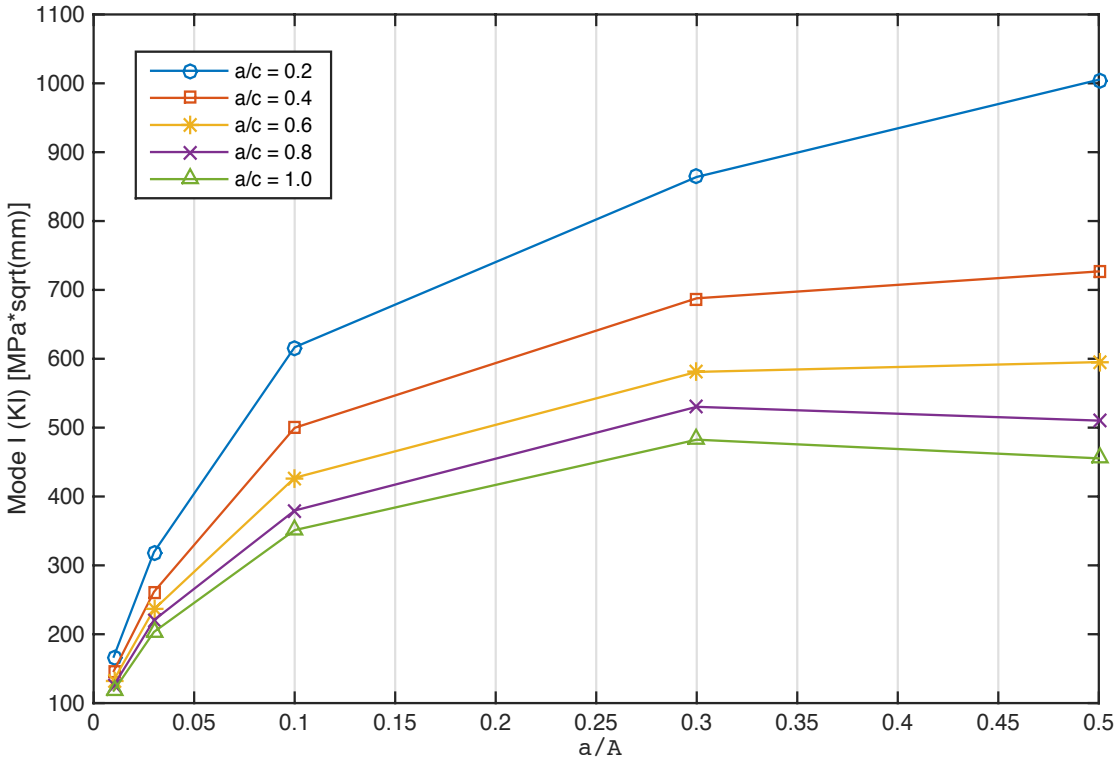

Figure 3.3 Mode I SIFs versus crack depth ratio *a/A* for different crack shape ratios for normal stress loading.

For mode II stress intensity factors, the same trend from mode I SIFs is observed. As the crack depth ratio increases, the stress intensity factors also increase for the different crack shape ratios, notice that for smaller crack shape ratios the curve is steeper and the SIFs are relatively higher compared to the SIFs for the larger crack shape ratios as shown in Figure 3.4. For smaller crack shape ratios, the crack depth is larger hence the higher SIFs are observed for smaller *a/c*.

Table 3.5 Mode II SIFs for crack depth ratio effect *a/A* for normal stress loading.

$K_{II}\ [MPa \cdot \sqrt{mm}]$						
a/c		0.2	0.4	0.6	0.8	1.0
a/A	0.01	74.17	61.61	50.97	40.06	37.22
	0.03	136.15	110.51	88.86	73.65	62.47
	0.10	254.90	192.89	150.65	121.10	99.06
	0.30	325.03	256.84	194.54	151.67	117.98
	0.50	380.00	258.16	198.56	147.38	107.92

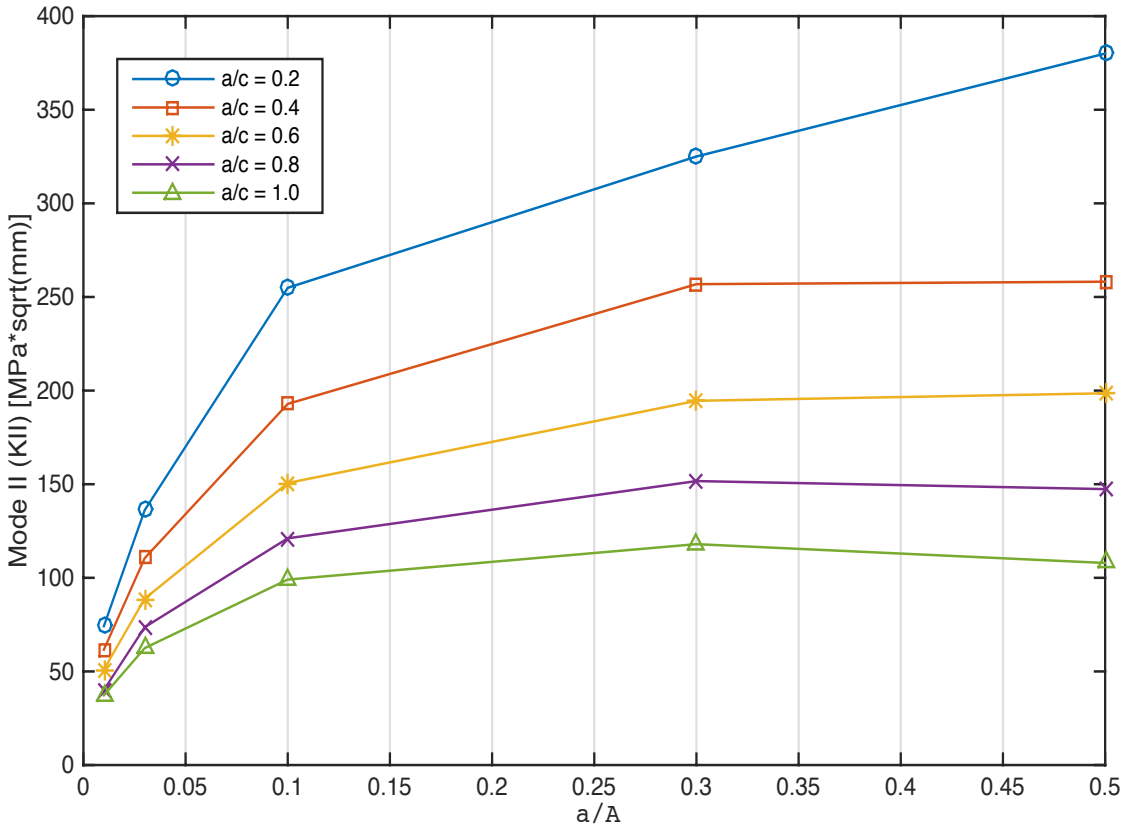

Figure 3.4 Mode II SIFs versus crack depth ratio *a/A* for different crack shape ratios for normal stress loading.

For mode III stress intensity factors, a slightly different behavior is observed. As the crack shape ratio increases, the curve becomes steeper hence the trend is reversed for the mode III stress intensity factors plotted against the crack depth ratio. Therefore, the larger the crack shape ratio, the steeper that curve is for mode III SIFs. Figure 3.5 depicts this trend. Although the trend is slightly reversed, it can still be seen that as the crack depth ratio increases, the mode III SIFs still increase for the different crack shape ratios.

Table 3.6 Mode III SIFs for crack depth ratio effect *a/A* for normal stress loading.

$K_{III}\ [MPa \cdot \sqrt{mm}]$						
a/c		0.2	0.4	0.6	0.8	1.0
a/A	0.01	17.48	25.19	31.48	32.28	37.92
	0.03	35.53	49.75	57.95	62.97	67.37
	0.10	64.49	99.39	111.71	118.52	122.71
	0.30	76.02	135.49	159.65	180.00	187.34
	0.50	72.91	126.02	166.38	184.67	186.27

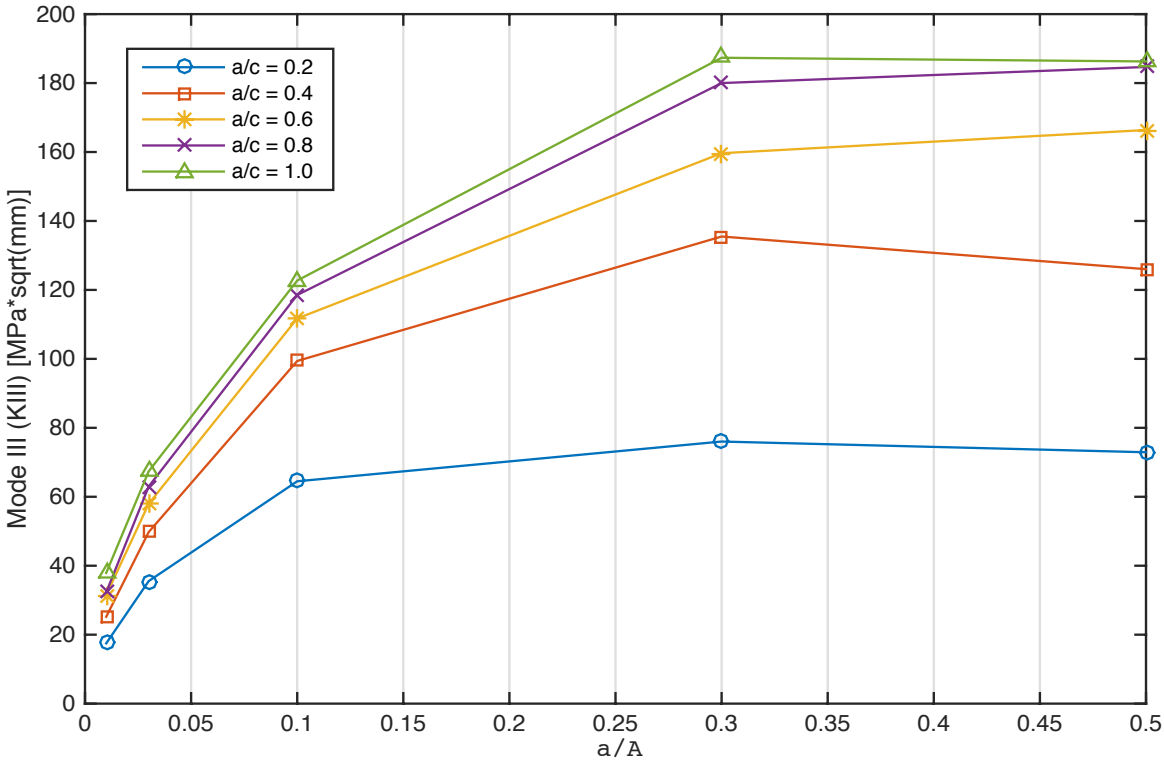

Figure 3.5 Mode III SIFs versus crack depth ratio *a/A* for different crack shape ratios for normal stress loading.

3.1.2 The effect of varying the crack shape ratio a/c (Normal Stress Loading)

In this section, the effect of the crack shape ratio is analyzed by varying the weld angle θ for the normal stress loading case. Three different weld angles are tested, which are $30°, 45°,$ and $60°$. Figures 3.6 (a) and (b) show the weld angles for $\theta = 30°$ and $\theta = 45°$ respectively. Figure 3.2 (a) already shows the case for the weld angle for $\theta = 60°$. The boundary elements vary according to each crack shape ratio, Table 3.7 shows the number of boundary elements used for the mesh of each crack surface model. Please refer to Figure 3.2 (b) as it already shows how the crack surface is modeled using 8-noded quadrilateral elements. Notice that there is not much change in the number of boundary elements used to model for each of the crack shape ratios for the different weld angles as shown in Table 3.7. We set a few parameters constant for the analyzing the effect of the crack shape ratio *a/c*. The crack depth ratio is fixed at *a/A* = 0.01, which means the crack depth is set to *a* = 2 mm while the quarter-elliptical crack length varies according to the crack shape ratio. The weld leg ratio is fixed at *L/A* = 1.5, hence making the weld leg *L* = 30 mm. Table 3.7 shows the crack lengths *c* for each crack shape ratio since the crack depth ratio *a/A* is fixed. The number of finite elements and boundary elements used for each crack configuration with different weld angles are also shown in Table 3.7.

Table 3.7 FEM/BEM elements and crack surface dimensions for studying the effect of crack shape ratio *a/c.*

Fixed Parameters: *L/A = 1.5, a/A = 0.10*				
θ [Degrees]		30°	45°	60°
Fixed: *a = 2 mm*		FEM: 3903	FEM: 3865	FEM: 3907
***c* [mm]**	***a/c***	BEM:	BEM:	BEM:
c = 10	0.2	96	96	96
c = 5	0.4	127	127	127
c = 3.33	0.6	161	161	161
c = 2.5	0.8	147	147	147
c = 2	1.0	173	173	173

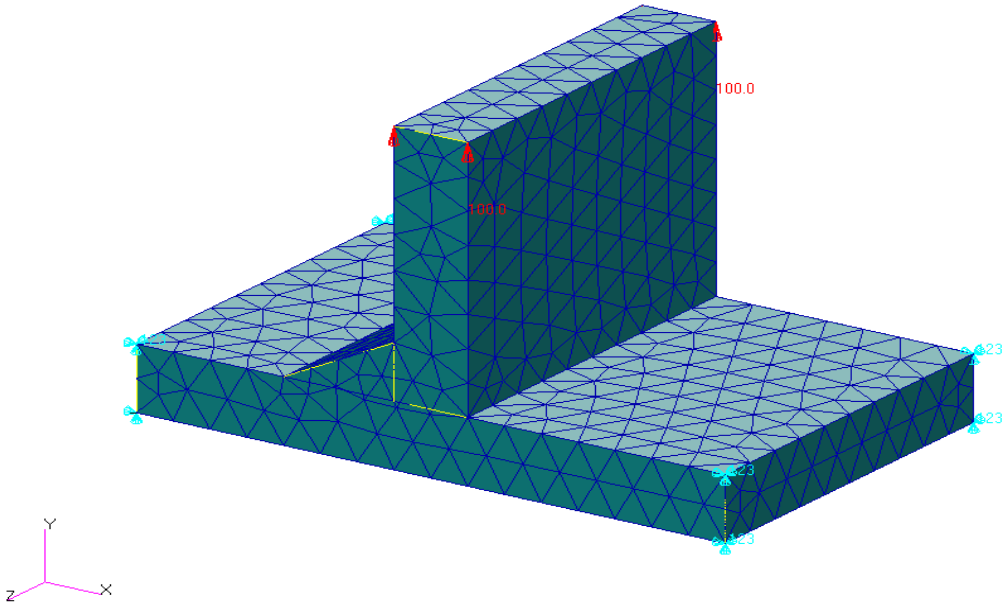

(a)

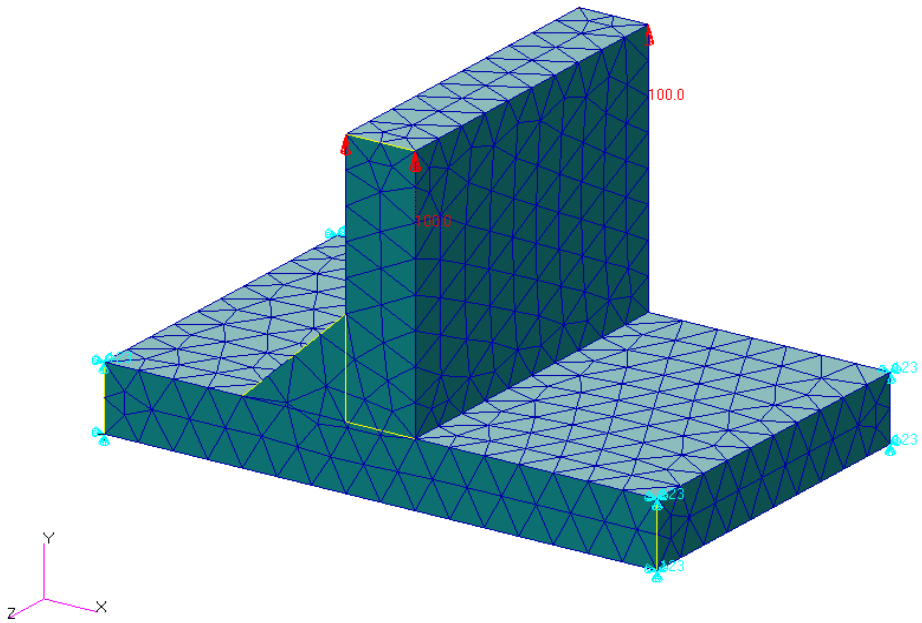

(b)

Figure 3.6 (a) Finite element mesh for the un-cracked structure modeled with 3903 10-noded tetrahedron elements for weld angle $\theta = 30°$ (b) Finite element mesh for the un-cracked structure modeled with 3865 10-noded tetrahedron elements for weld angle $\theta = 45°$.

It can be seen from Figure 3.7 that the mode I stress intensity factors decrease as the crack shape ratio increases for the different cases of weld angles. It can also be deducted from the behavior of the plot that as the weld angle increases, the mode I SIFs also increase. Table 3.8 shows the mode I SIFs numerically evaluated using the SGBEM-FEM Alternating Method.

Table 3.8 Mode I SIFs for crack shape ratio effect *a/c* for normal stress loading.

$K_I\ [MPa \cdot \sqrt{mm}]$				
θ [Degrees]		30°	45°	60°
a/c	0.2	538.18	594.87	616.82
	0.4	428.07	499.80	499.74
	0.6	359.96	422.80	427.17
	0.6	317.95	374.71	379.64
	1.0	291.89	343.12	351.18

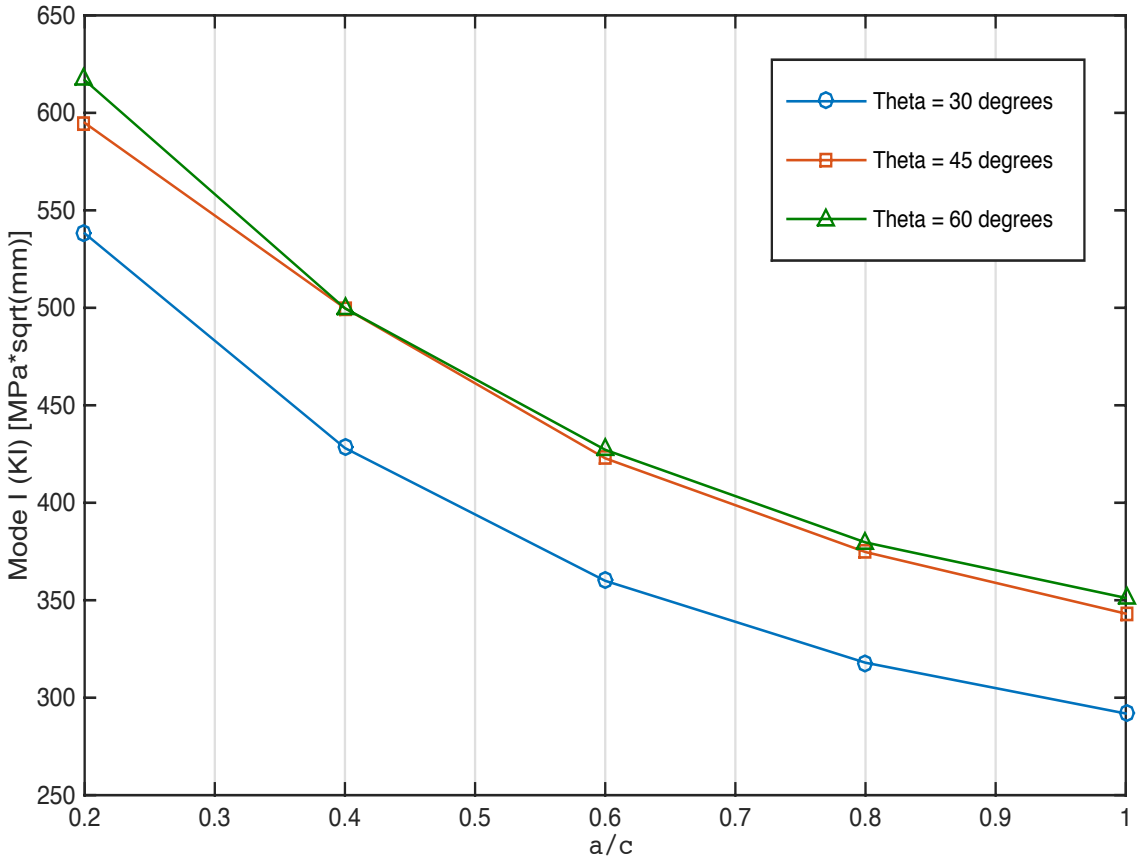

Figure 3.7 Mode I SIFs versus crack shape ratio *a/c* for different weld angles for normal stress loading.

In Figure 3.7, notice that there is not much difference in the mode I SIFs from changing the weld angle from 45° to 60° whereas there is a noticeable difference in the mode I stress intensity factors from changing the weld angle from 30° to 45°. Figure 3.8 shows the mode II stress intensity factors plotted against the crack shape ratio for the different weld angles. The numerically evaluated mode II SIFs are also shown in Table 3.9 for the different weld angles.

Table 3.9 Mode II SIFs for crack shape ratio effect *a/c* for normal stress loading.

K_{II} $[MPa \cdot \sqrt{mm}]$				
θ [Degrees]		30°	45°	60°
a/c	0.2	205.48	226.83	254.90
	0.4	167.65	182.65	192.89
	0.6	132.85	146.12	150.65
	0.6	105.86	117.38	121.10
	1.0	86.47	94.86	99.06

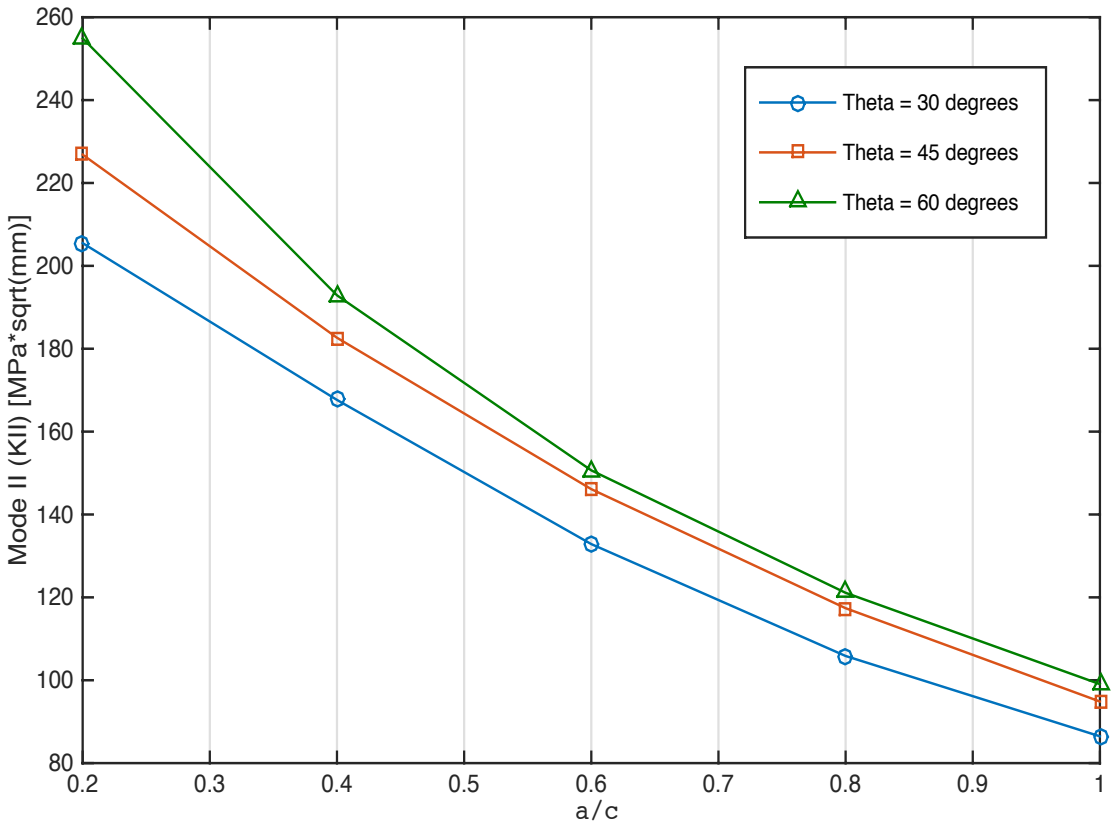

Figure 3.8 Mode II SIFs versus crack shape ratio *a/c* for different weld angles for normal stress loading.

The mode II SIFs curves are similar to the mode I SIFs curves in Figure 3.7. The higher the weld angle, the higher the mode II stress intensity factors. The stress intensity factors decrease as the crack shape ratio increases for all the different cases of weld angles. Notice now in Figure 3.8 that there is not much difference in the mode II stress intensity factors between the different weld angles. Table 3.10 and Figure 3.9 show the numerically computed mode III SIFs and the mode III SIFs plotted against the crack shape ratio for the different weld angles.

Table 3.10 Mode III SIFs for crack shape ratio effect *a/c* for normal stress loading.

K_{II} $[MPa \cdot \sqrt{mm}]$				
θ [Degrees]		30°	45°	60°
a/c	0.2	71.37	68.27	64.49
	0.4	103.94	101.36	99.39
	0.6	113.53	115.28	111.71
	0.6	119.31	123.04	118.52
	1.0	122.59	127.06	122.71

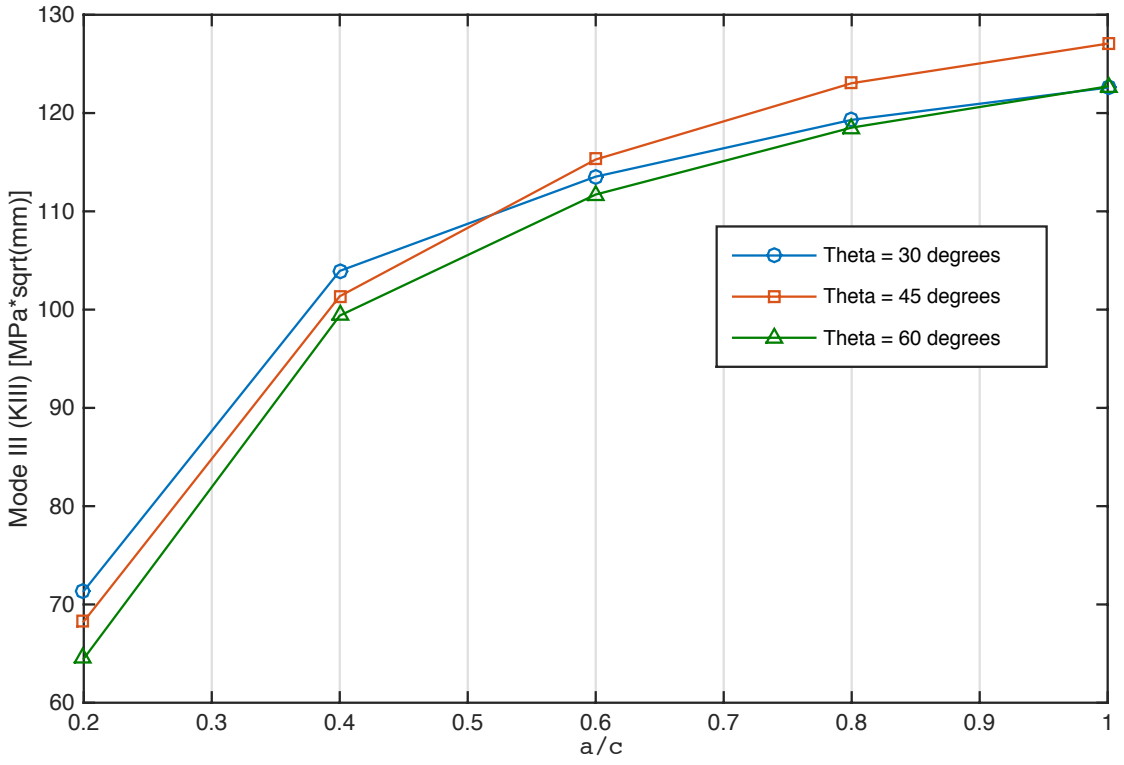

Figure 3.9 Mode III SIFs versus crack shape ratio *a/c* for different weld angles for normal stress loading.

In Figure 3.9, the mode III stress intensity factor curves are obviously reversed unlike the mode I and mode II SIFs. For mode III stress intensity factor curves, it can be seen that as the crack shape ratio increases, the mode III stress intensity factors also increase. Although there is not much difference in the mode III stress intensity factors for the different cases of the weld angles, it can be seen that with a combination of weld angle $\theta = 45°$ and a larger crack shape ratio produces the highest mode III stress intensity factor results compared to the other two weld angles with larger crack shape ratios, this can be seen in Figure 3.9.

3.1.3 The effect of varying the weld leg ratio L/A (Normal Stress Loading)

In this section, we study the effect of the weld leg ratio on the mixed-mode stress intensity factors. Five different weld leg ratios were tested, L/A = 0.5, 0.8, 1.0, 1.2 and 1.5 and the mixed-mode stress intensity factors are plotted against the weld leg ratio for the different crack shape ratios. A few parameters were fixed while the weld leg ratio was varied, the crack depth ratio is set to a/A = 0.10 and the weld angle is set to $\theta = 45°$. Table 3.11 shows the dimensions of the weld leg as the weld leg ratio is varied.

Table 3.11 Weld leg dimensions for various weld leg ratios.

Weld Leg Ratio (L/A)	Weld Leg (L) [mm]
L/A = 0.5	L = 10
L/A = 0.8	L = 16
L/A = 1.0	L = 20
L/A = 1.2	L = 24
L/A = 1.5	L = 30

The following figures below show the finite element mesh for each of the weld leg ratio, the finite element mesh for the case of weld leg ratio of L/A = 1.5, $\theta = 45°$, and a/A = 0.10 is already shown in Figure 3.6 (b). The crack mesh is modeled with 8-noded quadrilateral elements

(refer to Figure 3.2 (b)), the dimensions of the crack and the FEM/BEM elements for each weld leg ratio case are shown in Table 3.12.

Table 3.12 FEM/BEM elements and crack surface dimensions for studying the effect of weld leg ratio *L/A*.

Fixed Parameters: $\theta = 45°$ $a/A = 0.10$						
a/c		0.2	0.4	0.6	0.8	1.0
Fixed: *a = 2 mm*		*c = 10 mm*	*c = 5 mm*	*c = 3.33 mm*	*c = 2.5 mm*	*c = 2 mm*
L/A	0.5	FEM Elements: 3965				
		BEM: 96	BEM: 127	BEM: 161	BEM: 147	BEM: 173
	0.8	FEM Elements: 3902				
		BEM: 96	BEM: 127	BEM: 161	BEM: 147	BEM: 173
	1.0	FEM Elements: 3913				
		BEM: 96	BEM: 127	BEM: 161	BEM: 147	BEM: 173
	1.2	FEM Elements: 3803				
		BEM: 96	BEM: 127	BEM: 161	BEM: 147	BEM: 173
	1.5	FEM Elements: 3865				
		BEM: 96	BEM: 127	BEM: 161	BEM: 147	BEM: 173

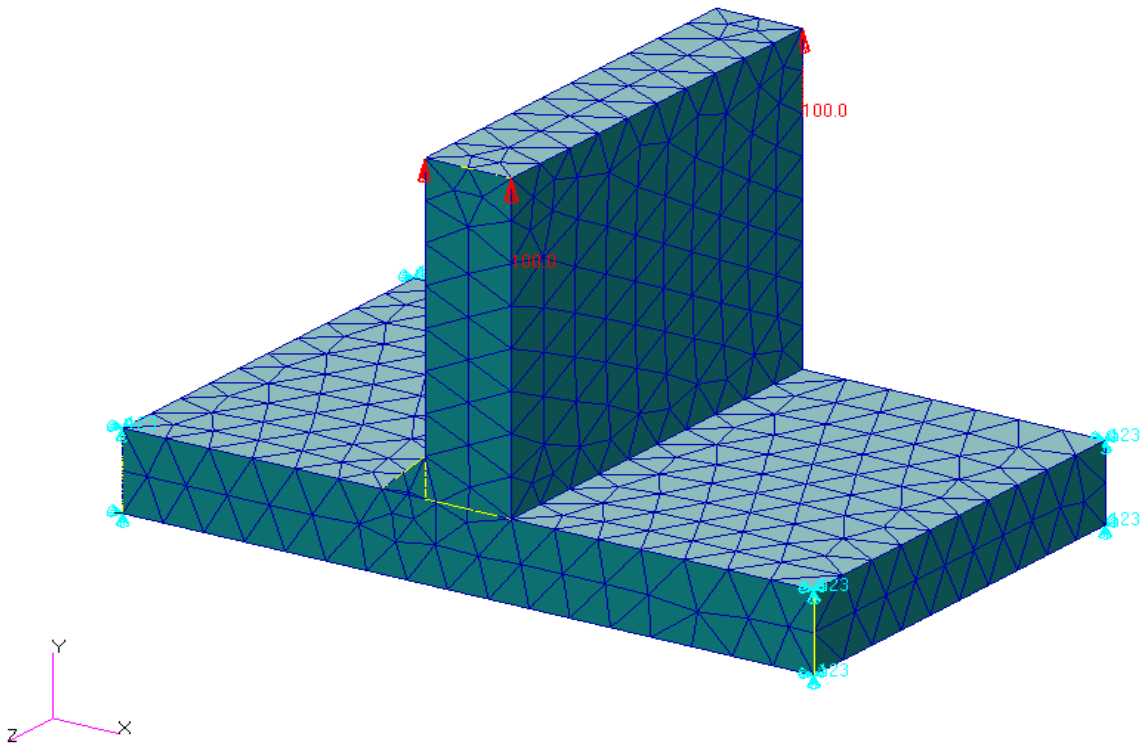

(a)

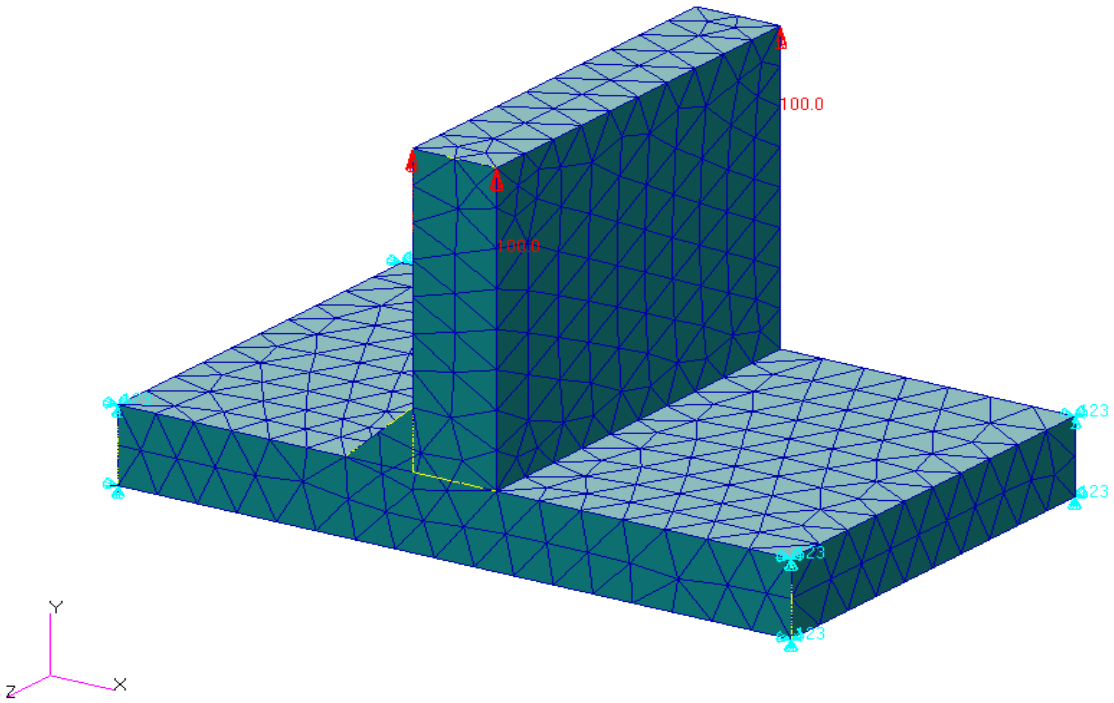

(b)

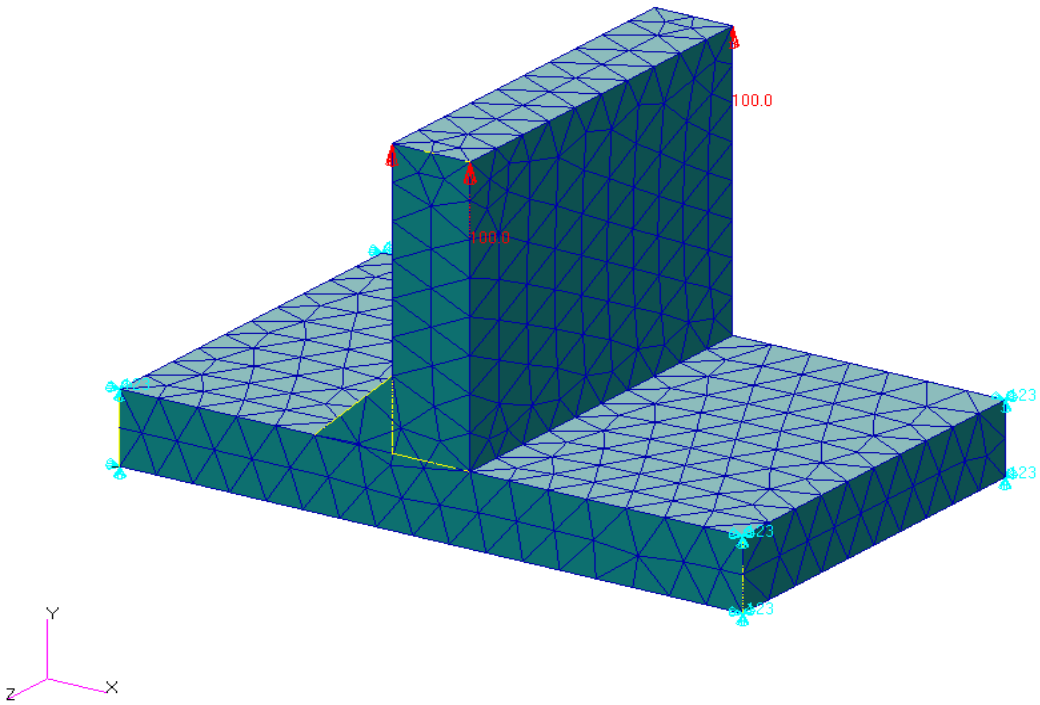

(c)

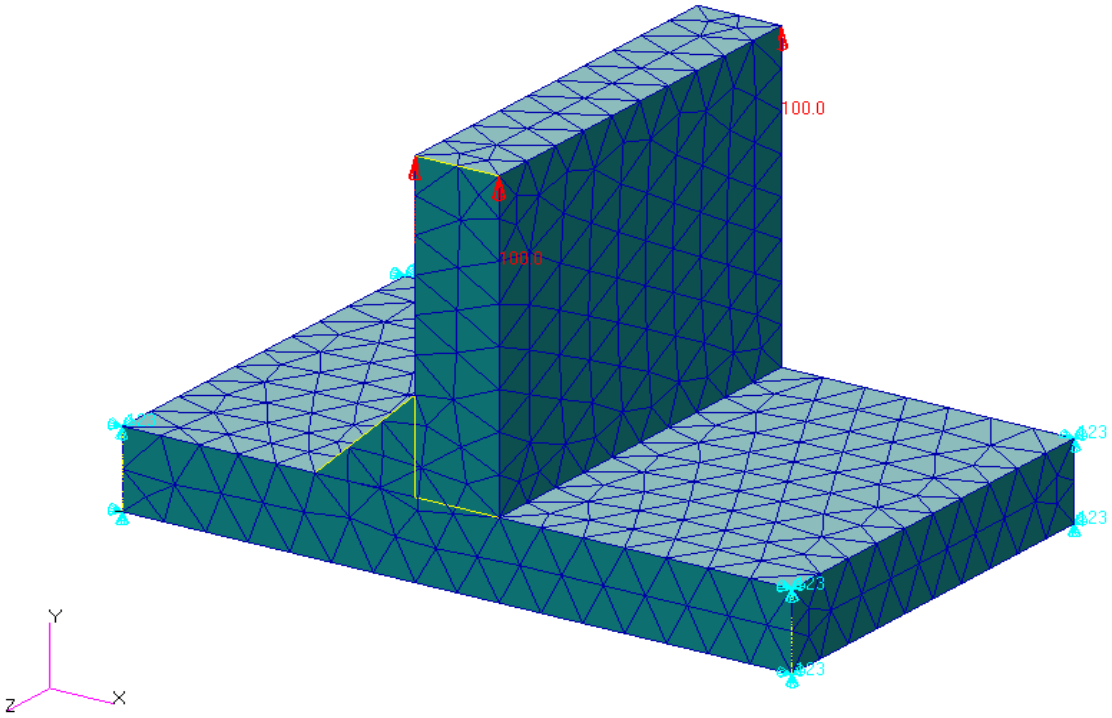

(d)

Figure 3.10 Finite element meshes for un-cracked structure for (a) weld leg ratio of *L/A* = 0.5 modeled with 3965 10-noded tetrahedron elements, (b) weld leg ratio of *L/A* = 0.8 modeled with 3902 10-noded tetrahedron elements, (c) weld leg ratio of *L/A* = 1.0 modeled with 3913 10-noded tetrahedron elements, (d) weld leg ratio of *L/A* = 1.2 modeled with 3803 10-noded tetrahedron elements.

The following table, Table 3.13 shows the mode I stress intensity factors for the various weld leg ratios. From the plot (Figure 3.11), the stress intensity factors increase as the weld leg ratio is increased. For a smaller crack shape ratios, the stress intensity factors are higher compared to the larger crack shape ratios where the stress intensity factors are lower. For the weld leg ratio of *L/A* = 1.2, the stress intensity factors slightly decrease for all the different crack shape ratios as shown in Figure 3.11 but in general, increasing the weld leg ratio further results in an increase in the mode I stress intensity factors for all the different crack shape ratios.

Table 3.13 Mode I SIFs for weld leg ratio effect *L/A* for normal stress loading.

$K_I\ [MPa \cdot \sqrt{mm}]$						
a/c		0.2	0.4	0.6	0.8	1.0
L/A	0.5	452.01	338.48	271.31	232.29	209.12
	0.8	516.34	395.48	340.35	280.50	254.59
	1.0	571.95	459.93	381.91	336.54	308.13
	1.2	549.19	436.44	366.70	326.99	300.11
	1.5	594.87	499.80	422.80	374.71	343.12

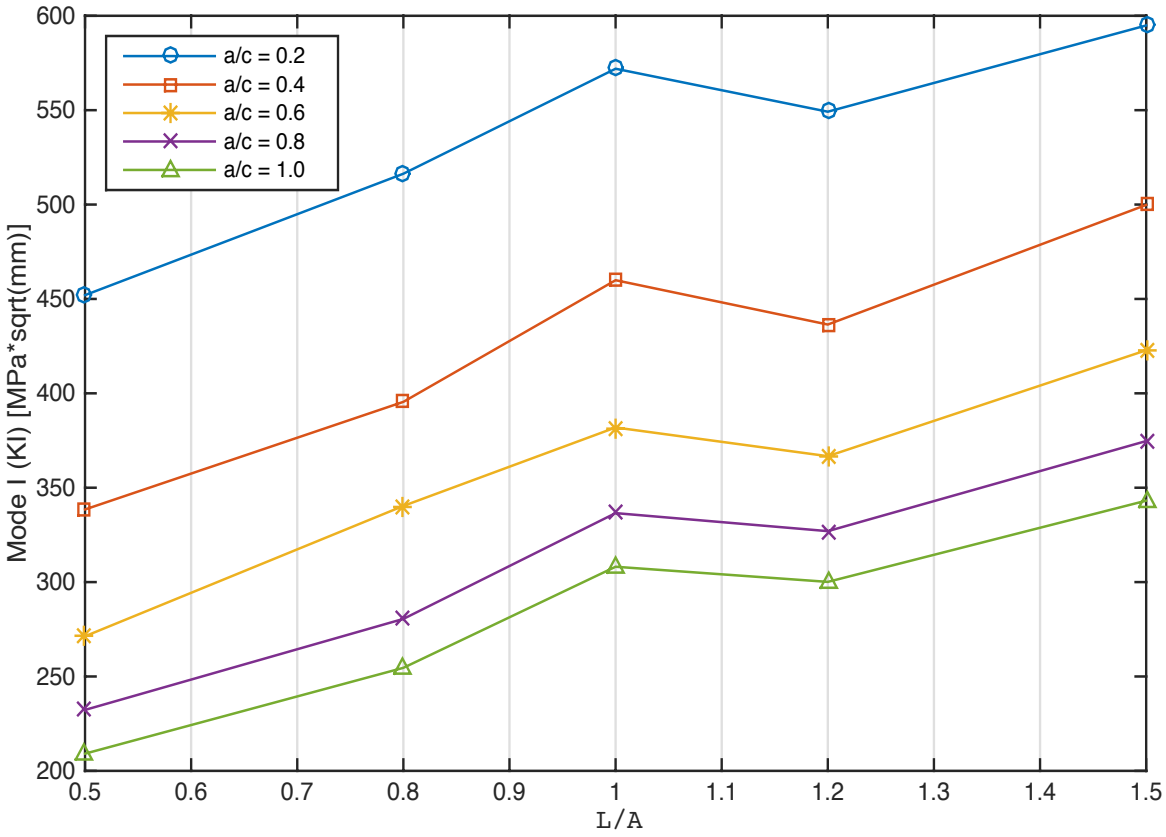

Figure 3.11 Mode I SIFs versus weld leg ratio *L/A* for different crack shape ratios for normal stress loading.

Table 3.14 and Figure 3.13 show the mode II stress intensity factors for the weld leg ratio effect. The trend depicted for mode II SIFs curves are similar to that of the mode I SIFs curves but it should be noted that for mode II SIFs, it can be seen that the highest mode II stress

intensity factors result with a weld leg ratio of *L/A* = 1.0 but as the weld leg ratio is further increased, it can be seen that the mode II SIFs start to slightly decrease.

Table 3.14 Mode II SIFs for weld leg ratio effect *L/A* for normal stress loading.

$K_{II}\ [MPa \cdot \sqrt{mm}]$						
a/c		0.2	0.4	0.6	0.8	1.0
L/A	0.5	228.89	175.82	137.41	108.54	87.38
	0.8	246.58	189.31	149.22	115.53	92.76
	1.0	255.65	196.30	149.80	117.01	92.86
	1.2	214.44	172.28	137.79	111.40	91.81
	1.5	226.83	182.65	146.12	117.38	94.86

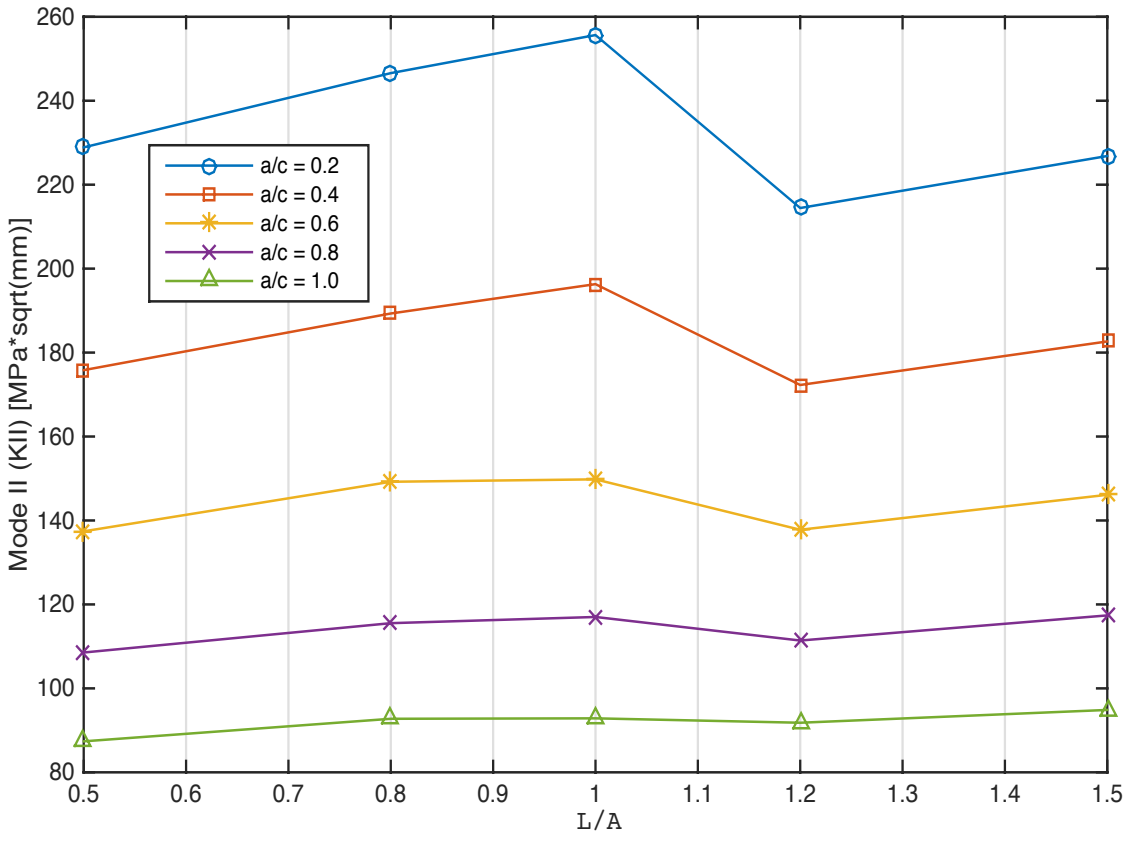

Figure 3.12 Mode II SIFs versus weld leg ratio *L/A* for different crack shape ratios for normal stress loading.

Table 3.15 and Figure 3.13 show the mode III stress intensity factors for the weld leg ratio effect. For mode III SIFs, the curves are similar to mode I and mode II and the mode III stress intensity factors are the highest when the weld leg ratio is set to *L/A* = 1.0 for the different

crack shape ratios. As the weld leg ratio is increased, the mode III SIFs start to slightly increase after the sudden dip for the weld leg ratio of L/A = 1.2 for all the different crack shape ratios. For mode I and mode II SIFs, the smaller the crack shape ratio, the higher the stress intensity factors but for the mode III SIFs, the larger the crack shape ratio, the higher the stress intensity factors. This noticeable behavior for mode III SIFs for weld leg ratio effect can be seen in Figure 3.13.

Table 3.15 Mode III SIFs for weld leg ratio effect *L/A* for normal stress loading.

$K_{III}\ [MPa \cdot \sqrt{mm}]$						
a/c		0.2	0.4	0.6	0.8	1.0
L/A	0.5	65.35	95.21	106.68	112.19	115.27
	0.8	72.54	103.88	112.39	121.24	124.28
	1.0	82.21	120.59	128.77	131.72	133.78
	1.2	63.83	99.21	109.85	116.18	120.78
	1.5	68.27	101.36	115.28	123.04	127.06

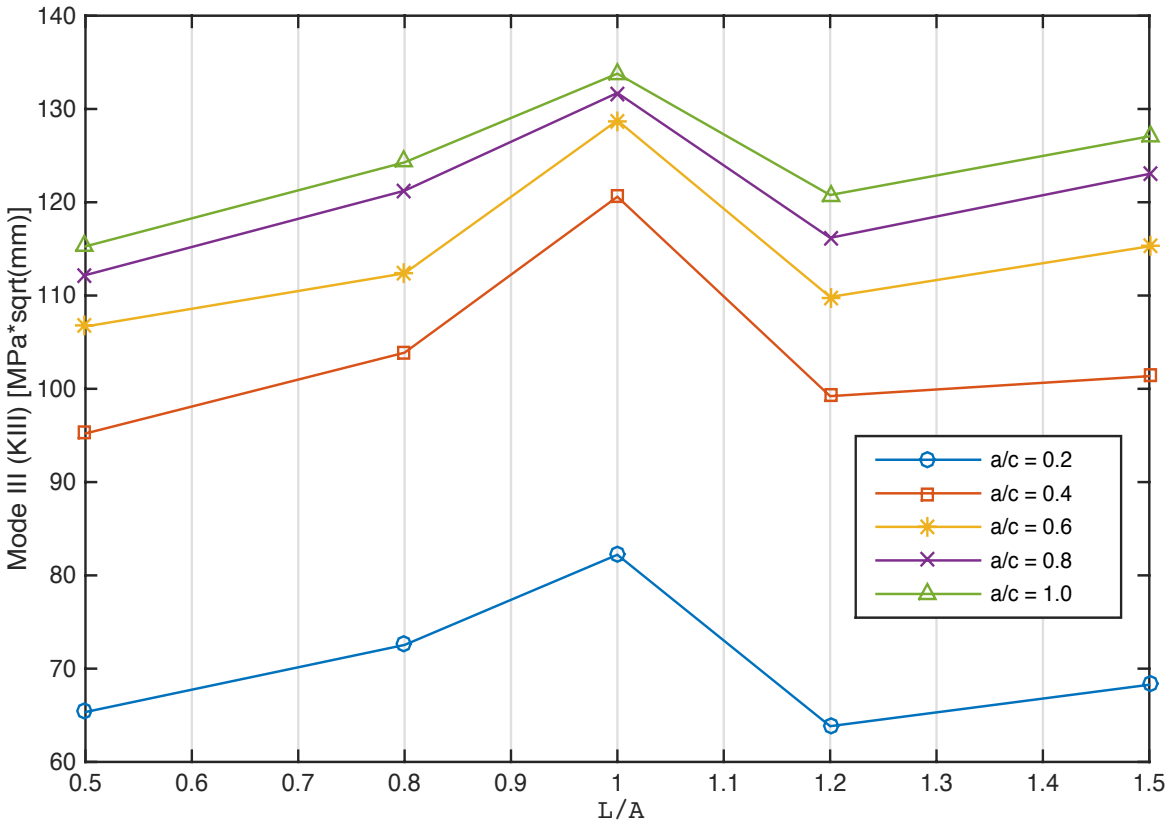

Figure 3.13 Mode III SIFs versus weld leg ratio *L/A* for different crack shape ratios for normal stress loading.

3.1.4 The effect of varying the weld angle θ (Normal Stress Loading)

In this section, the weld angle is varied for the T-butt joint to study the effect on mixed-mode SIFs. Three different weld angles are considered, $\theta = 30°, 45°$ and $60°$. The parameters that are fixed for this case are the weld leg ratio *L/A* and the crack depth ratio *a/A*. The weld leg ratio is set to *L/A* = 0.5 making the weld leg to be set at *L* = 10 mm and the crack depth ratio is set to *a/A* = 0.10. Figure 3.14 (a) and (b) show the meshes for the weld angles $\theta = 30°$ and $\theta = 60°$. The finite element mesh for the case of $\theta = 45°$ with the weld leg ratio and crack depth ratio of 0.5 and 0.10 respectively is already shown in Figure 3.10 (a). Table 3.16 shows the FEM/BEM elements for the different weld angles for the normal stress loading case. The crack surface mesh is modeled with 8-noded quadrilateral elements as shown in Figure 3.2 (b) while the FEM mesh is modeled using 10-noded tetrahedron elements.

Table 3.16 FEM/BEM elements and crack surface dimensions for studying the effect of weld angle θ.

Fixed Parameters: *L/A = 0.5, a/A = 0.10*						
a/c		0.2	0.4	0.6	0.8	1.0
Fixed: *a = 2 mm*		*c = 10 mm*	*c = 5 mm*	*c = 3.33 mm*	*c = 2.5 mm*	*c = 2 mm*
θ [Degrees]	30°	FEM Elements: 3940				
		BEM: 96	BEM: 127	BEM: 161	BEM: 147	BEM: 173
	45°	FEM Elements: 3965				
		BEM: 96	BEM: 127	BEM: 161	BEM: 147	BEM: 173
	60°	FEM Elements: 3886				
		BEM: 96	BEM: 127	BEM: 161	BEM: 147	BEM: 173

The meshes for the three different weld angles are shown below in Figure 3.14 (a) and (b). It is crucial to note at this point that for all the FEM and BEM meshes modeled for the T-butt joint does not exceed 5000 elements. This is one of the advantages of using the SGBEM-FEM Alternating Method, a simple coarse mesh can be used for the analysis of fracture mechanics parameters for 3D complex structures.

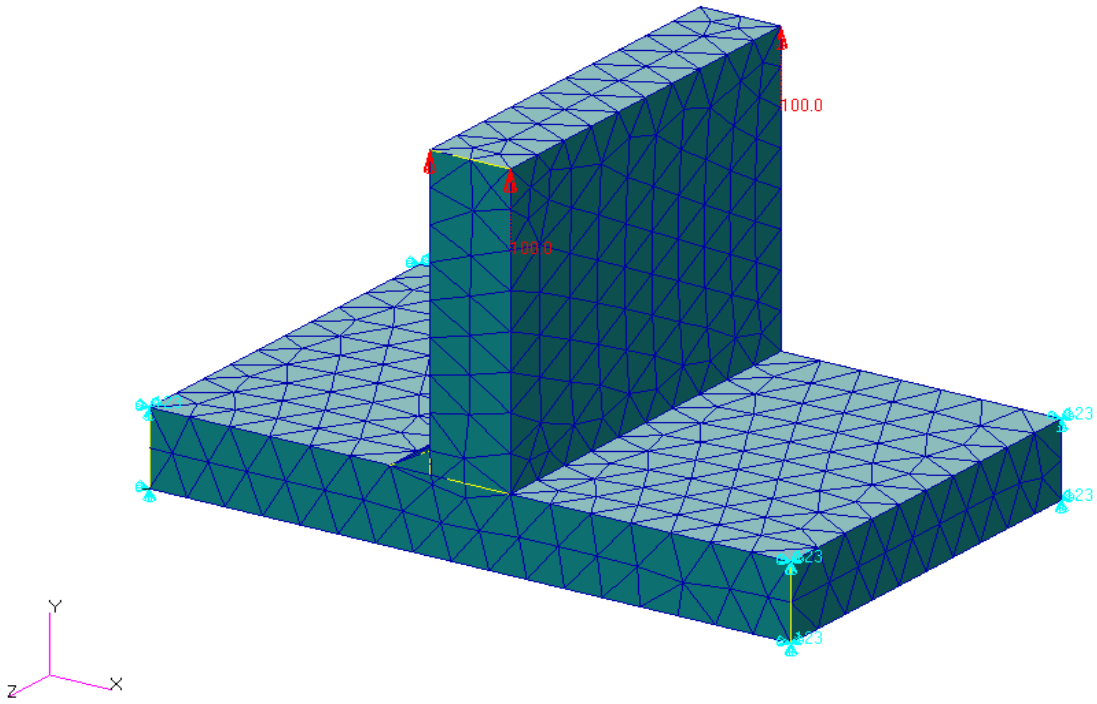

(a)

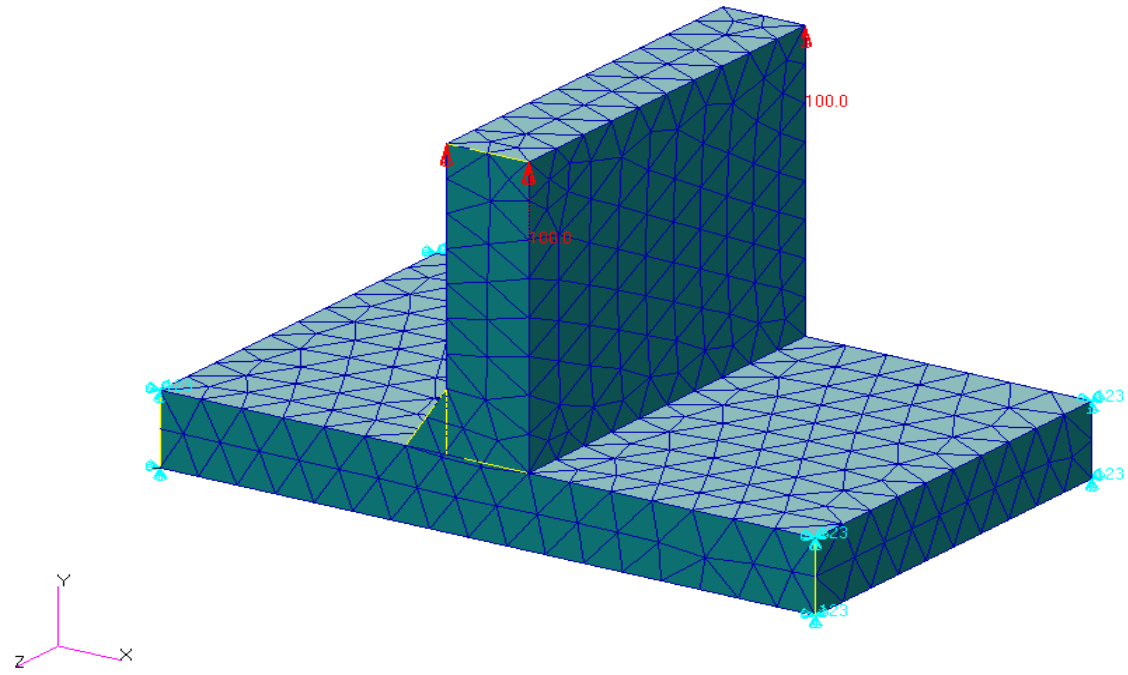

(b)

Figure 3.14 Finite element meshes for un-cracked structure for (a) weld angle $\theta = 30°$ modeled with 3940 10-noded tetrahedron elements, (b) weld angle $\theta = 60°$ modeled with 3886 10-noded tetrahedron elements.

Table 3.17 below shows the numerically obtained mode I stress intensity factors for the different weld angles. Figure 3.15 shows the mode I stress intensity factors plotted against the weld angles. As the weld angle is increased, the mode I stress intensity factors increase for all the different crack shape ratios. It can also be seen from Figure 3.15 that for a smaller crack shape ratio, the mode I SIFs are higher for the different weld angles as compared to the larger crack shape ratios where the mode I SIFs are lower for the different weld angles.

Table 3.17 Mode I SIFs for weld angle effect θ for normal stress loading.

$K_I\ [MPa \cdot \sqrt{mm}]$					
a/c	0.2	0.4	0.6	0.8	1.0
θ [Degrees]					
30°	428.25	323.93	258.44	220.18	197.29
45°	452.01	338.48	271.31	232.29	209.12
60°	448.70	345.69	286.08	248.38	227.18

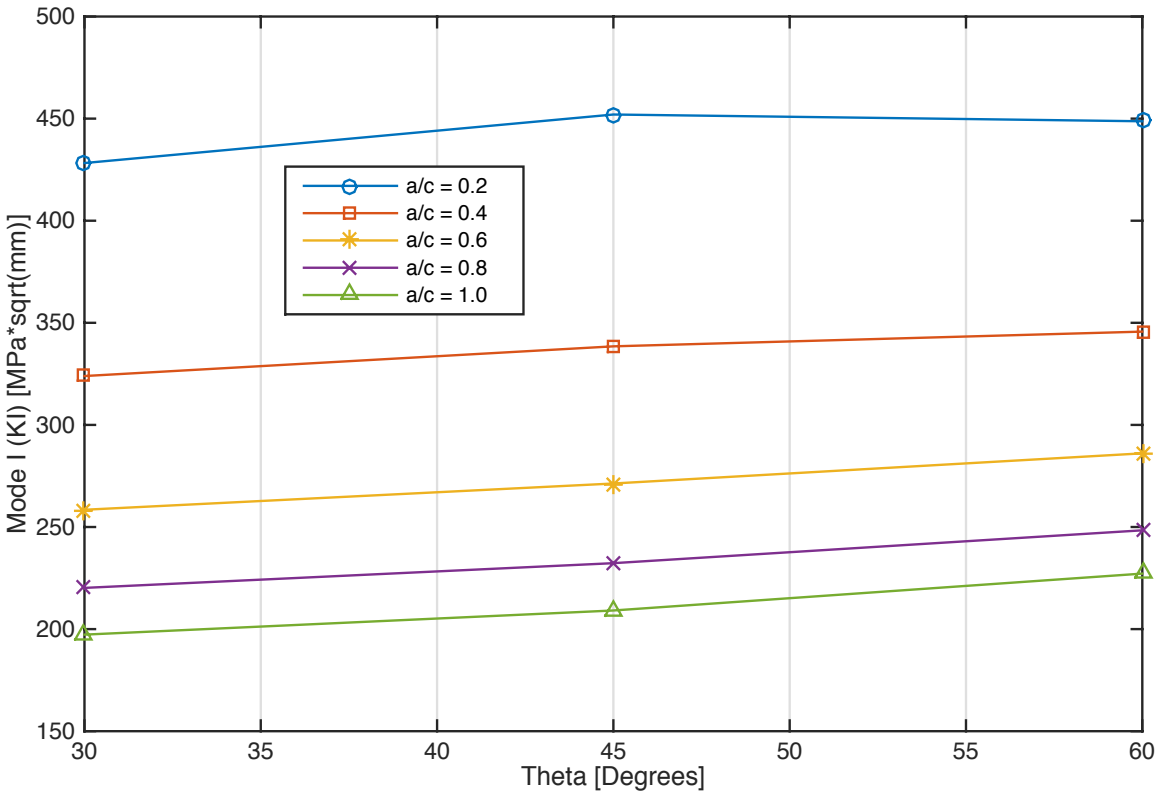

Figure 3.15 Mode I SIFs versus weld angle θ for different crack shape ratios for normal stress loading.

For mode II stress intensity factors, the behavior that is observed is the opposite of mode I SIFs trend. As the weld angle is increased, the mode II stress intensity factors decrease for the different crack shape ratios. As observed in Figure 3.16, for smaller crack shape ratios, the mode II stress intensity factors are higher for the different weld angles as compared to larger crack shape ratios where the stress intensity factors are lower for the different weld angles. Table 3.18 and Figure 3.16 show this behavior for the mode II SIFs behavior for the weld angle effect.

Table 3.18 Mode II SIFs for weld angle effect θ for normal stress loading.

$K_{II}\ [MPa \cdot \sqrt{mm}]$					
a/c	0.2	0.4	0.6	0.8	1.0
θ [Degrees]					
30°	260.75	195.96	150.26	117.41	92.46
45°	228.89	175.82	137.41	108.54	87.38
60°	216.31	172.67	132.23	105.83	83.94

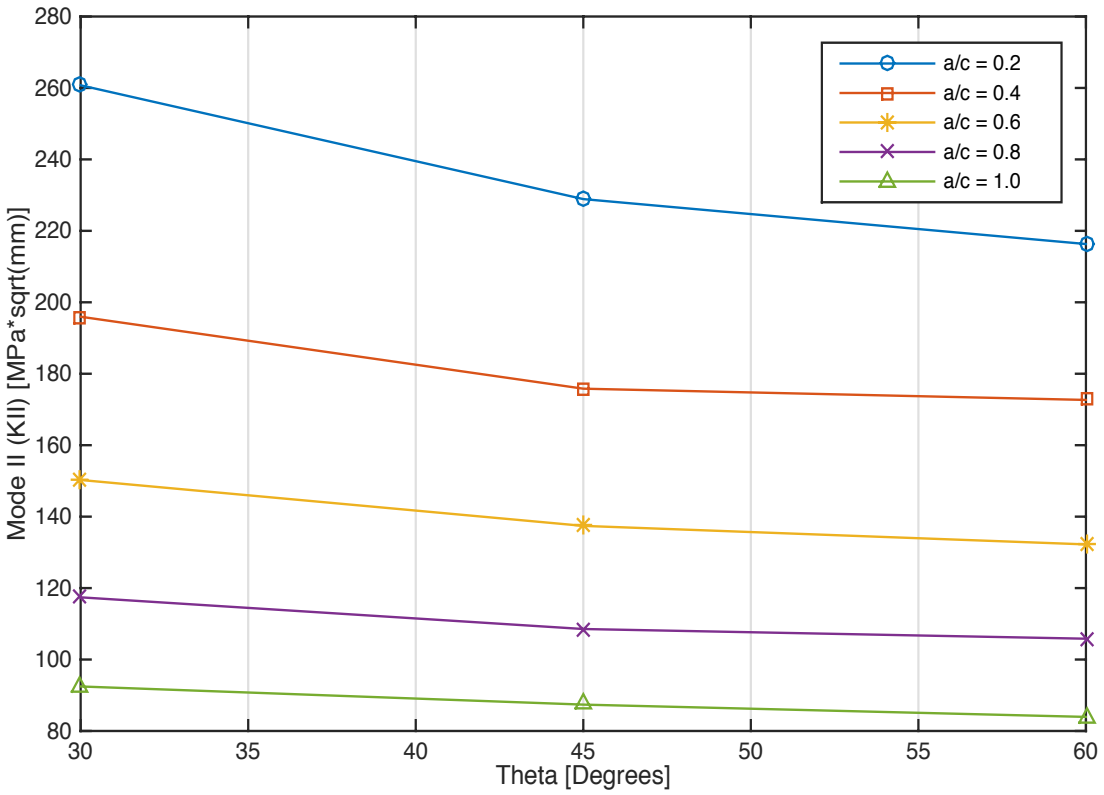

Figure 3.16 Mode II SIFs versus weld angle θ for different crack shape ratios for normal stress loading.

From Figure 3.17, the mode III SIFs behavior for the different weld angles with varying crack shape ratios, it can be seen that there is a sudden dip for all the different crack shape ratios when the weld angle is set to $\theta = 45°$. There is a slight increase again in the mode III SIFs as the weld angle is continuously increased for all the different crack shape ratios. A noticeable trend that is seen throughout the mode III SIFs plots is that the larger the crack shape ratio, the higher the mode III SIFs. Hence it can be seen in Figure 3.17 that for a larger crack shape ratio, the mode III stress intensity factors are significantly higher compared to a smaller crack shape ratio.

Table 3.19 Mode III SIFs for weld angle effect θ for normal stress loading.

$K_{III}\ [MPa \cdot \sqrt{mm}]$					
a/c	0.2	0.4	0.6	0.8	1.0
θ [Degrees]					
30°	85.58	117.27	126.36	129.77	130.80
45°	65.35	95.21	106.68	112.19	115.27
60°	64.29	100.19	114.01	119.59	123.10

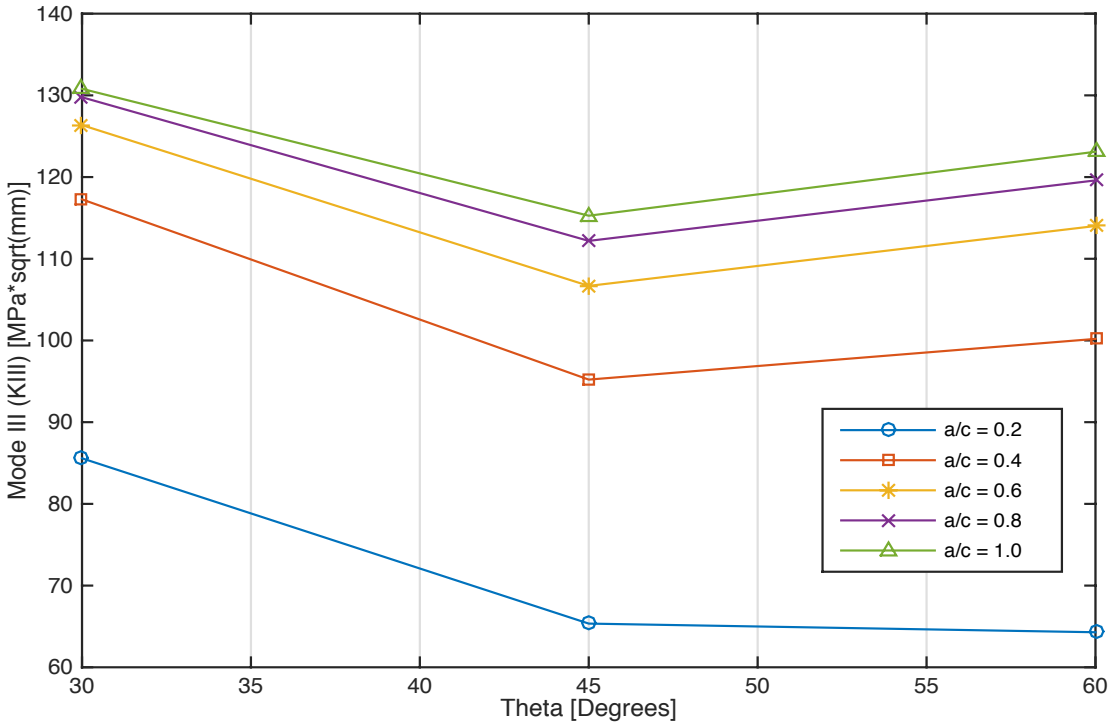

Figure 3.17 Mode III SIFs versus weld angle θ for different crack shape ratios for normal stress loading.

3.1.5 T-butt joint subjected to shear force loading

In this section, the T-butt joint is subjected to shear loading and the geometrical parameters are varied accordingly to study the effects on the mixed-mode SIFs for each case. The shear stress $\sigma_{xy} = 100\ MPa$ is resolved in to a shear force for computational simplicity. The computed value for the shear force is $F_{shear} = 200{,}000\ MPa$. It should be noted in this section that the only thing that is changed in the FEM model is the load application. The elements used for the meshes do not change at all, therefore there is no need to refine the meshes for analyzing the effects of varying the geometrical parameters for the T-butt joint for the case of shear stress loading. The boundary elements used for the crack surface model for each specific case study are the same as previous. Figure 3.18 shows an example mesh for the T-butt joint for a specific case of fixed geometric parameters with the application of the shear force.

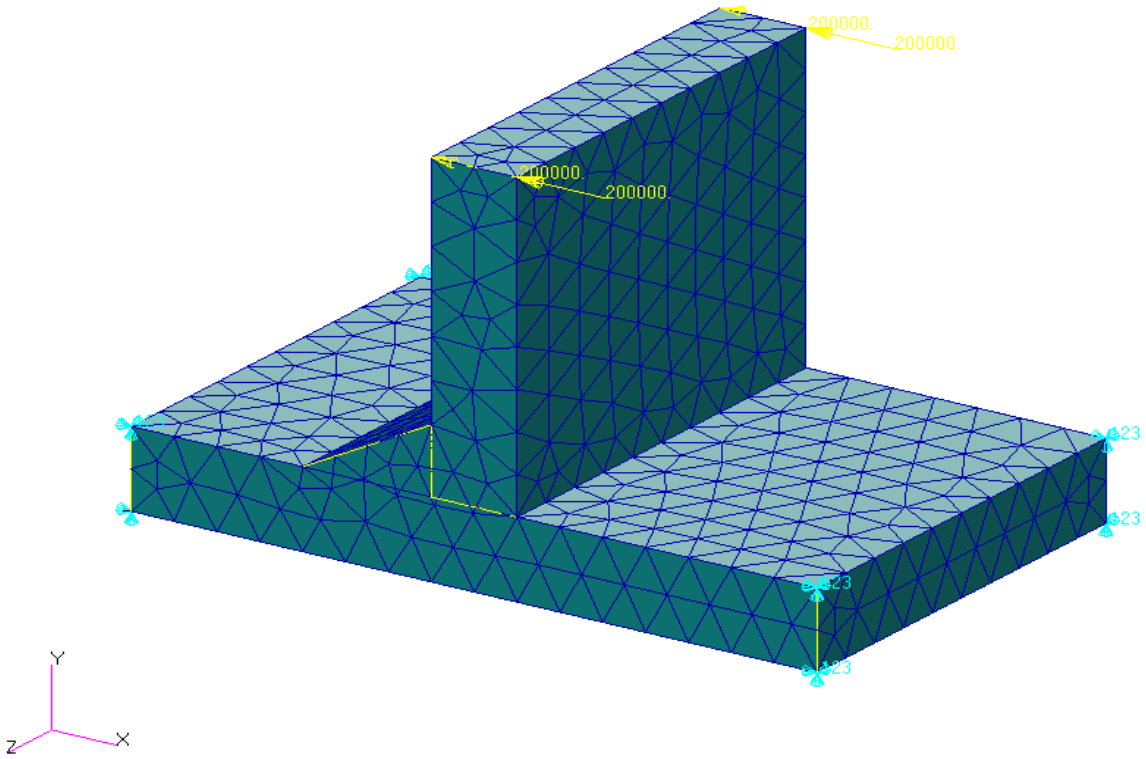

Figure 3.18 Example of finite element mesh of the un-cracked global structure with the application of shear force.

3.1.6 The effect of varying the crack depth ratio a/A (Shear Force Loading)

The number of elements used for the FEM mesh and for the BEM mesh for the crack surface model do not change for the crack depth ratio effect, refer to Table 3.2 and 3.3 for the crack surface dimensions, the FEM/BEM elements, and the fixed parameters for this case. Table 3.20 and Figure 3.19 show mode I SIFs for *a/A* effect under shear loading. A comparison will be done between the mixed-mode SIFs obtained for both normal loading and shear loading cases.

Table 3.20 Mode I SIFs for crack depth ratio effect *a/A* for shear force loading.

$K_I\ [MPa \cdot \sqrt{mm}]$						
a/c		0.2	0.4	0.6	0.8	1.0
a/A	0.01	33451.37	29546.62	27003.31	25531.43	23944.77
	0.03	62805.84	52512.77	47924.85	44983.82	41780.43
	0.10	121613.41	100655.21	87627.26	78851.54	73480.64
	0.30	187152.67	150129.84	128811.04	118031.74	108430.34
	0.50	234009.53	171807.74	142854.99	124631.73	112869.76

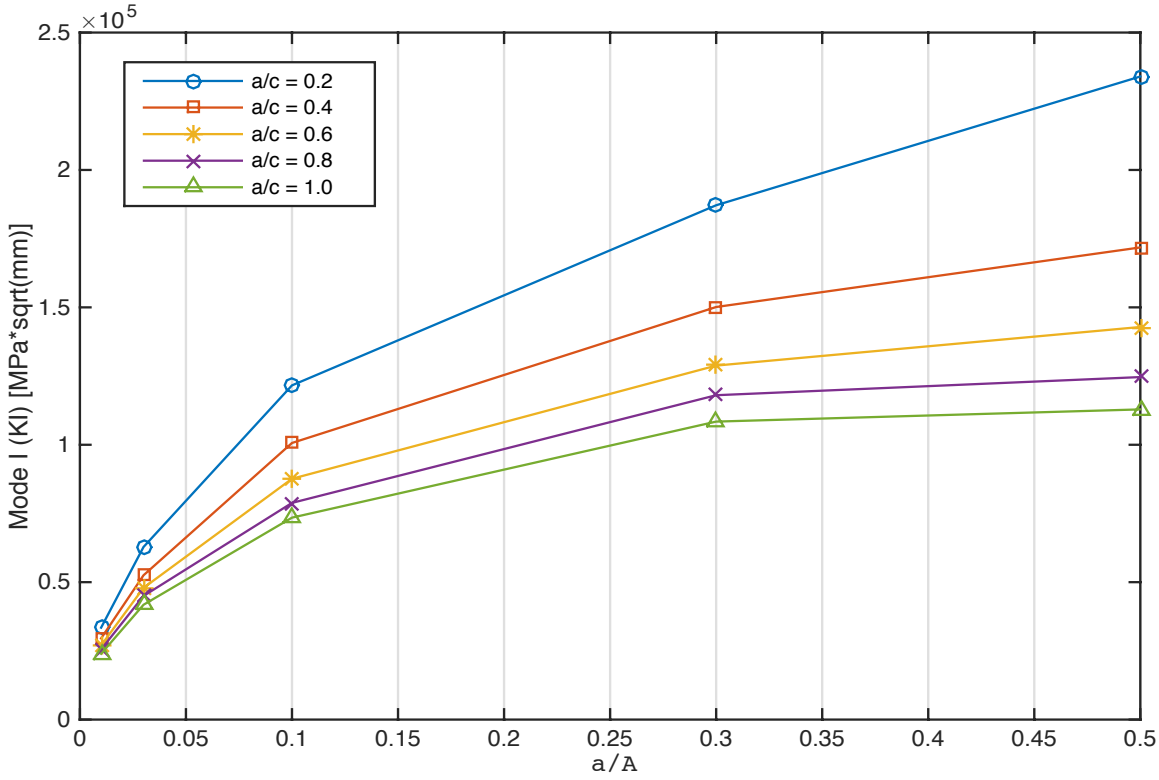

Figure 3.19 Mode I SIFs versus crack depth ratio *a/A* for different crack shape ratios for shear force loading.

As seen in Figure 3.19, for the crack depth ratio effect *a/A* for shear loading, the same trend is observed for the shear case in comparison with the normal stress loading case shown in Figure 3.3. It can be deducted for the shear loading case that with a smaller crack shape ratio the mode I SIFs are higher as seen by the steepness of the smaller crack shape ratio curves compared to the larger crack shape ratios. It can also be seen that as the crack depth ratio is increased, the mode I SIFs increase for all the different crack shape ratios as seen in Figure 3.19. Table 3.21 and Figure 3.20 show the mode II SIFs for the crack depth ratio effect under shear force loading.

Table 3.21 Mode II SIFs for crack depth ratio effect *a/A* for shear force loading.

$K_{II}\ [MPa \cdot \sqrt{mm}]$						
a/c		0.2	0.4	0.6	0.8	1.0
a/A	0.01	10011.95	8427.59	7069.60	5719.98	5540.43
	0.03	18838.73	15217.65	12118.21	10295.21	9024.78
	0.10	35947.68	25340.37	19344.68	15594.48	12959.57
	0.30	39483.89	27383.87	18342.06	13171.81	9464.34
	0.50	40911.39	18511.69	10568.08	4729.24	813.46

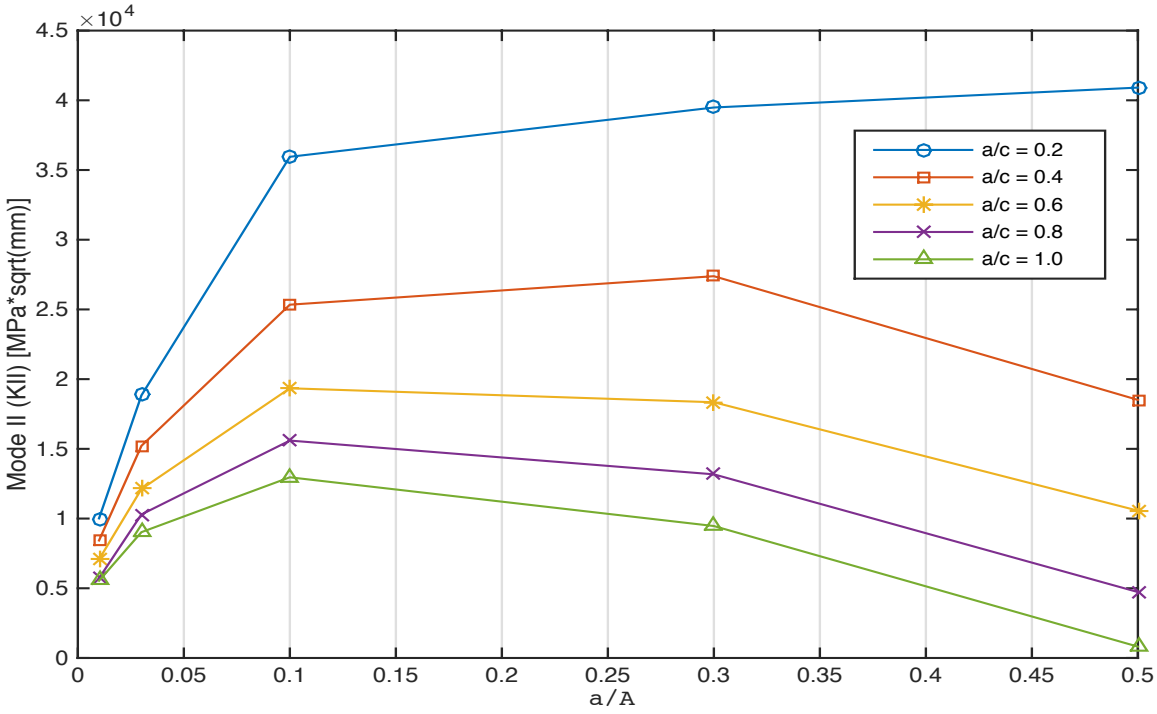

Figure 3.20 Mode II SIFs versus crack depth ratio *a/A* for different crack shape ratios for shear force loading.

For mode II, as the crack depth ratio is increased, the mode II SIFs decrease as seen in Figure 3.20. For a smaller crack shape ratio, the mode II SIFs are higher compared to the larger crack shape ratios where they are lower. In comparison to the normal loading case for the *a/A* effect, the mode II SIFs shown in Figure 3.4 increase as the crack depth ratio is increased which is the opposite of the observed mode II behavior for the shear loading case shown in Figure 3.20. Table 3.22 and Figure 3.21 show the mode III SIFs obtained for the crack depth ratio effect *a/A*.

Table 3.22 Mode III SIFs for crack depth ratio effect *a/A* for shear force loading.

$K_{III}\ [MPa \cdot \sqrt{mm}]$						
a/c		0.2	0.4	0.6	0.8	1.0
a/A	0.01	1206.02	2487.61	3514.91	3633.20	4662.49
	0.03	2766.54	5081.70	6387.99	7186.30	7936.50
	0.10	4073.85	10303.21	12253.10	13232.14	13882.92
	0.30	1699.93	10719.34	14296.55	17152.36	17903.07
	0.50	785.10	6032.66	11201.89	12778.14	11954.22

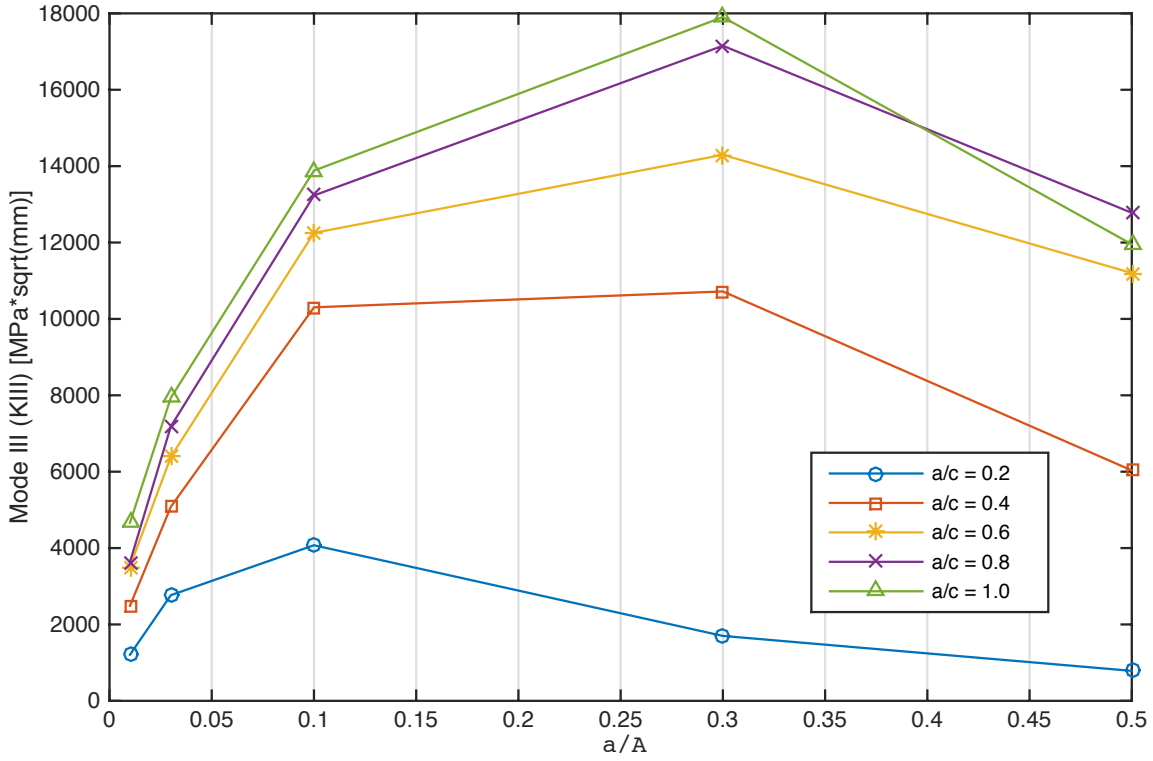

Figure 3.21 Mode III SIFs versus crack depth ratio *a/A* for different crack shape ratios for shear force loading.

It can be observed from Figure 3.21 that for an increasing crack depth ratio *a/A*, the mode III SIFs decrease. For mode I/II, the smaller crack shape ratios produce the highest SIFs as shown by the steepness of the curves but for mode III, it can be seen that for a larger crack shape ratio, the mode III SIFs are higher as shown by steepness of the larger *a/c* curve in Figure 3.21. By comparing both the loading cases for the crack depth ratio *a/A* effect of mode III fracture, it can be seen that for the normal stress loading (Figure 3.5) the same behavior is observed as for the shear loading case (Figure 3.21). Therefore, it can be concluded that for mode III SIFs for the crack depth ratio *a/A* effect, both loading cases produce similar trends.

3.1.7 The effect of varying the crack shape ratio a/c (Shear Force Loading)

In this section, the effect of the crack shape ratio *a/c* is studied by varying the weld angles for the shear force loading scenario. The FEM meshes used for studying the crack shape ratio effect for the different weld angles are already shown in Figure 3.6 (a), (b) and Figure 3.2 (a). The FEM/BEM elements, crack shape dimensions and the fixed parameters for this case are already shown in Table 3.7. Note that the FEM/BEM elements do not change at all which is one of the advantages of employing the SGBEM-FEM Alternating Method. Table 3.23 and Figure 3.22 show the numerically obtained mode I SIFs for the crack shape ratio effect for shear force loading case.

Table 3.23 Mode I SIFs for crack shape ratio effect *a/c* for shear force loading.

$K_I\ [MPa \cdot \sqrt{mm}]$				
θ [Degrees]		30°	45°	60°
a/c	0.2	199466.18	148559.44	121613.41
	0.4	167494.87	127956.45	100655.21
	0.6	147106.21	112031.15	87627.26
	0.6	133078.15	101598.86	78851.54
	1.0	124206.43	94321.94	73480.64

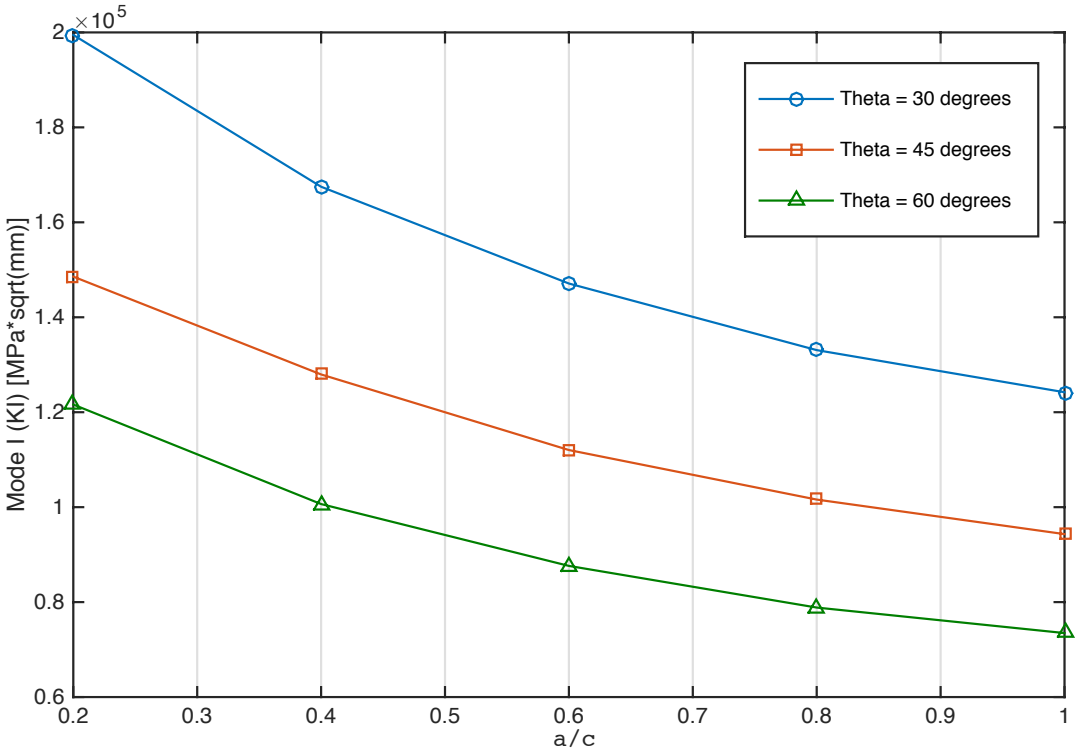

Figure 3.22 Mode I SIFs versus crack shape ratio *a/c* for different weld angles for shear force loading.

Figure 3.22 shows that as the crack shape ratio increases, the mode I SIFs decrease for all the different weld angles. It can also be deduced that increasing the weld angle decreases the mode I SIFs for the shear loading case. By comparing the normal and shear loading cases for the crack shape ratio effect, it can be seen that for the normal loading case (Figure 3.7) increasing the weld angle increases the mode I SIFs whereas for the shear loading case, it is the opposite behavior. Table 3.24 and Figure 3.23 show the mode II SIFs for *a/c* effect for shear loading case.

Table 3.24 Mode II SIFs for crack shape ratio effect *a/c* for shear force loading.

K_{II} $[MPa \cdot \sqrt{mm}]$				
θ [Degrees]		30°	45°	60°
a/c	0.2	14281.58	28790.31	35947.68
	0.4	7383.56	20608.15	25340.37
	0.6	4804.78	15918.55	19344.68
	0.6	3487.09	12920.28	15594.48
	1.0	3807.29	10894.64	12959.57

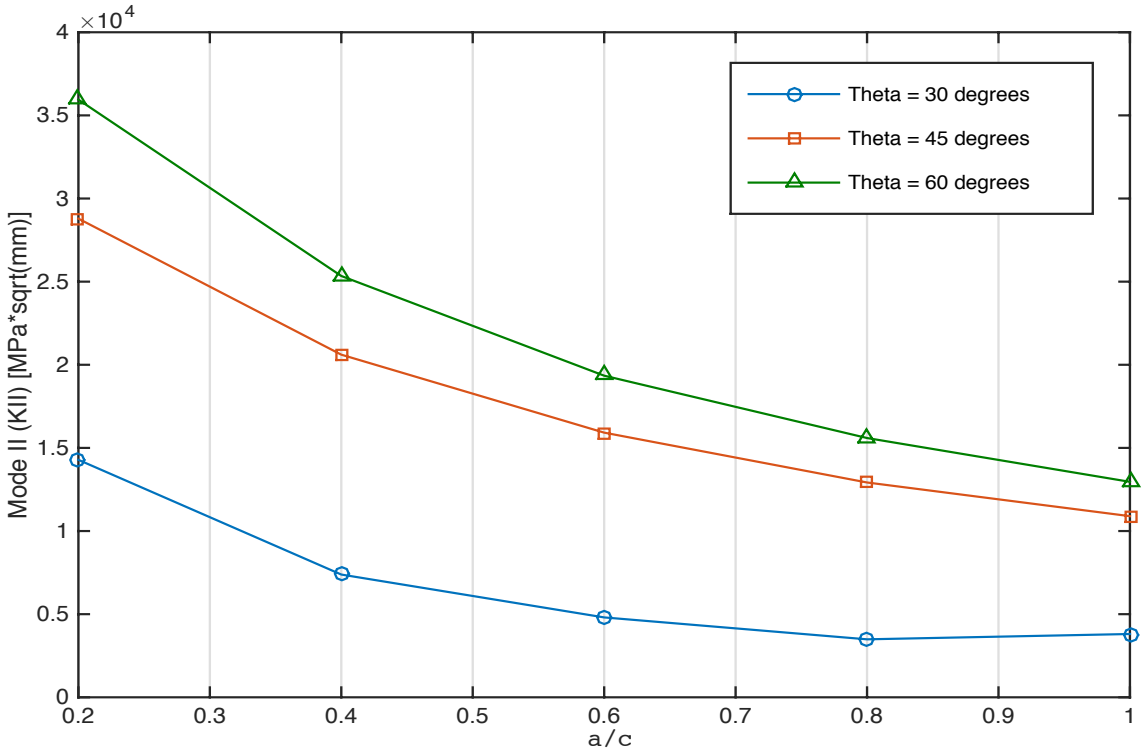

Figure 3.23 Mode II SIFs versus crack shape ratio *a/c* for different weld angles for shear force loading.

For mode II SIFs, it can be seen that as the crack shape ratio is increased, the mode II SIFs decrease for all the different weld angles. It can also be seen that increasing the weld angle increases the mode II SIFs, which can be seen in Figure 3.23. By comparing the mode II SIFs for both the normal (see Figure 3.8) and shear loading cases for the *a/c* effect, it can be concluded that the trends are identical and exhibit the same behavior as described. Table 3.25 and Figure 3.24 show the mode III SIFs for the crack shape ratio *a/c* effect for the shear force loading case.

Table 3.25 Mode III SIFs for crack shape ratio effect *a/c* for shear force loading.

$K_{III}\ [MPa \cdot \sqrt{mm}]$				
θ [Degrees]		30°	45°	60°
a/c	0.2	-5657.55	678.35	4073.85
	0.4	174.16	7239.21	10303.21
	0.6	1084.49	9398.21	12253.10
	0.6	1978.68	10560.87	13232.14
	1.0	2165.61	11295.39	13882.92

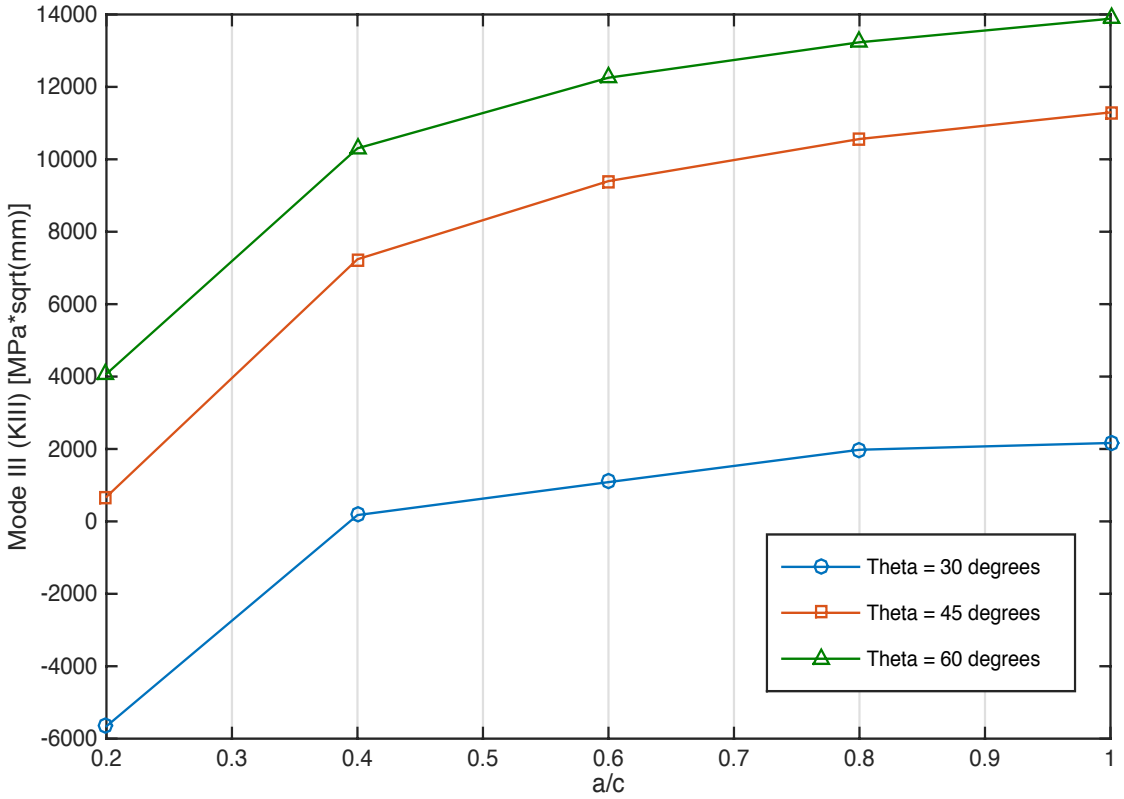

Figure 3.24 Mode III SIFs versus crack shape ratio *a/c* for different weld angles for shear force loading.

In Figure 3.24, it can be see that for mode III SIFs, as the crack shape ratio increases the mode III SIFs increase for all the different weld angles. The mode III SIFs also increase when the weld angle is increased. In comparison, the trend is similar to the trend observed for the normal loading case (see Figure 3.9) but it should be noted that for the normal loading case, the mode III SIFs do not vary much in the numerical sense hence it can be seen that the curves overlap for the different weld angles. For the shear loading case, there is more of a pronounced effect for changing the weld angle therefore when the weld angle is varied it can be seen that there is a huge difference in the mode III stress intensity factors for the crack shape ratio *a/c* effect for the shear force loading case as shown in Figure 3.24.

3.1.8 The effect of varying the weld leg ratio L/A (Shear Force Loading)

The weld leg ratio is varied for the T-butt joint in order to study the effect on the mixed-mode SIFs. The Finite element meshes for the different weld leg ratios are already shown in Figure 3.12 (a), (b), (c), (d) and Figure 3.6 (b). As stated earlier, the FEM/BEM elements are the same for all the different weld leg ratios studied, which is one of the advantages of the SGBEM-FEM Alternating Method. The FEM/BEM elements, the crack shape dimensions, and the fixed parameters for this case are already shown in Table 3.12. Furthermore, Table 3.26 shows the numerically computed mode I SIFs for the weld leg ratio effect under shear force loading for different crack shape ratios and Figure 3.25 shows the mode I SIFs plotted against the weld leg ratio for the different crack shape ratios under shear force loading.

Table 3.26 Mode I SIFs for weld leg ratio effect *L/A* for shear force loading.

$K_I\ [MPa \cdot \sqrt{mm}]$						
a/c		0.2	0.4	0.6	0.8	1.0
L/A	0.5	288463.21	245809.10	218676.75	200526.69	187753.89
	0.8	228443.65	190621.95	178474.81	152270.47	141943.78
	1.0	214162.80	183096.74	159543.70	145154.27	134907.07
	1.2	175386.54	146399.15	127333.90	115791.67	107405.98
	1.5	148559.44	127956.45	112031.15	101598.86	94321.94

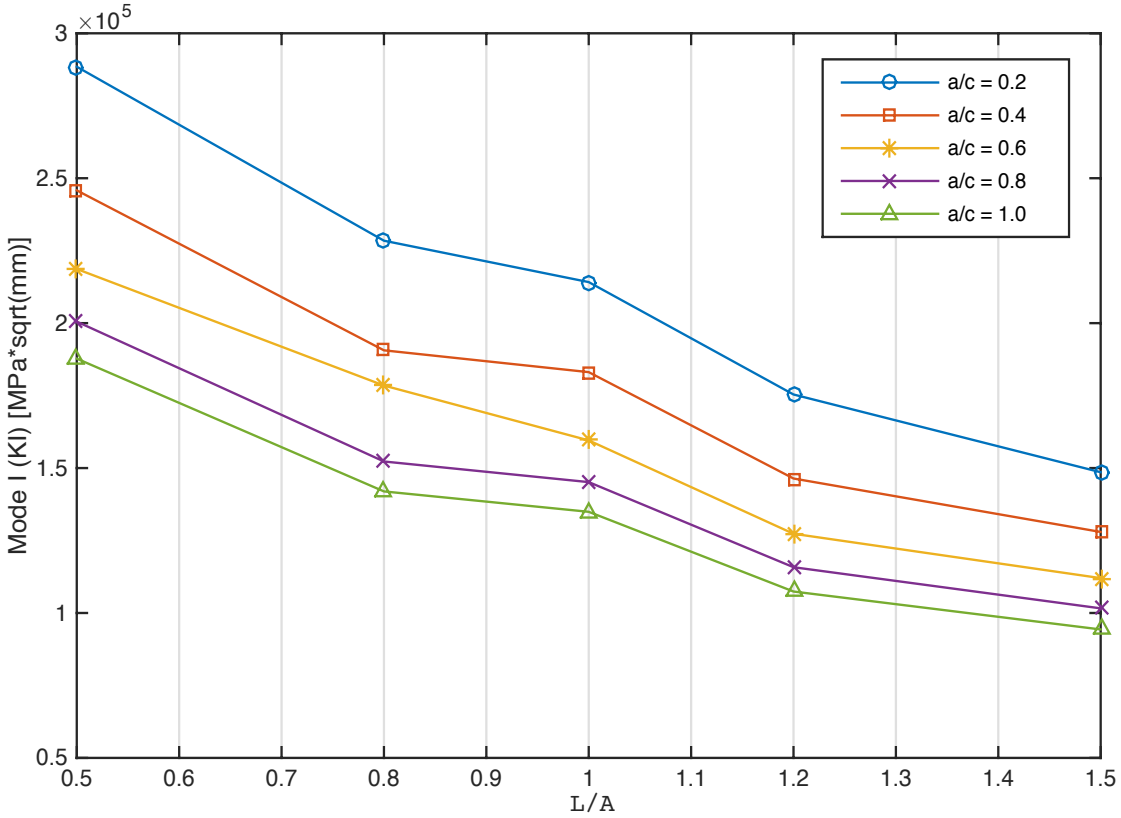

Figure 3.25 Mode I SIFs versus weld leg ratio *L/A* for different crack shape ratios for shear force loading.

From Figure 3.25, we see that as the weld leg ratio is increased, the mode I SIFs decrease for all the different crack shape ratios. It should also be noted that the mode I SIFs are higher for the smaller crack shape ratios. For the normal loading case for the weld leg ratio effect (see Figure 3.11), the opposite behavior is observed. Therefore, for normal loading case, the mode I SIFs increase as the weld leg ratio is increased and for shear loading case, the mode I SIFs decrease as the weld leg ratio is increased for the different crack shape ratios. Continuing with the analysis of the T-butt joint, Table 3.27 and Figure 3.26 show the mode II SIFs obtained for the weld leg ratio effect under shear loading.

Table 3.27 Mode II SIFs for weld leg ratio effect *L/A* for shear force loading.

$K_{II}\ [MPa \cdot \sqrt{mm}]$						
a/c		0.2	0.4	0.6	0.8	1.0
L/A	0.5	15855.13	1537.86	-2601.32	-2811.20	-1863.65
	0.8	22930.96	9091.99	6055.31	2879.84	2878.96
	1.0	28978.34	16562.21	10721.44	8165.33	7116.68
	1.2	23773.65	15002.43	11266.26	9288.11	8250.25
	1.5	28790.31	20608.15	15918.55	12920.28	10894.64

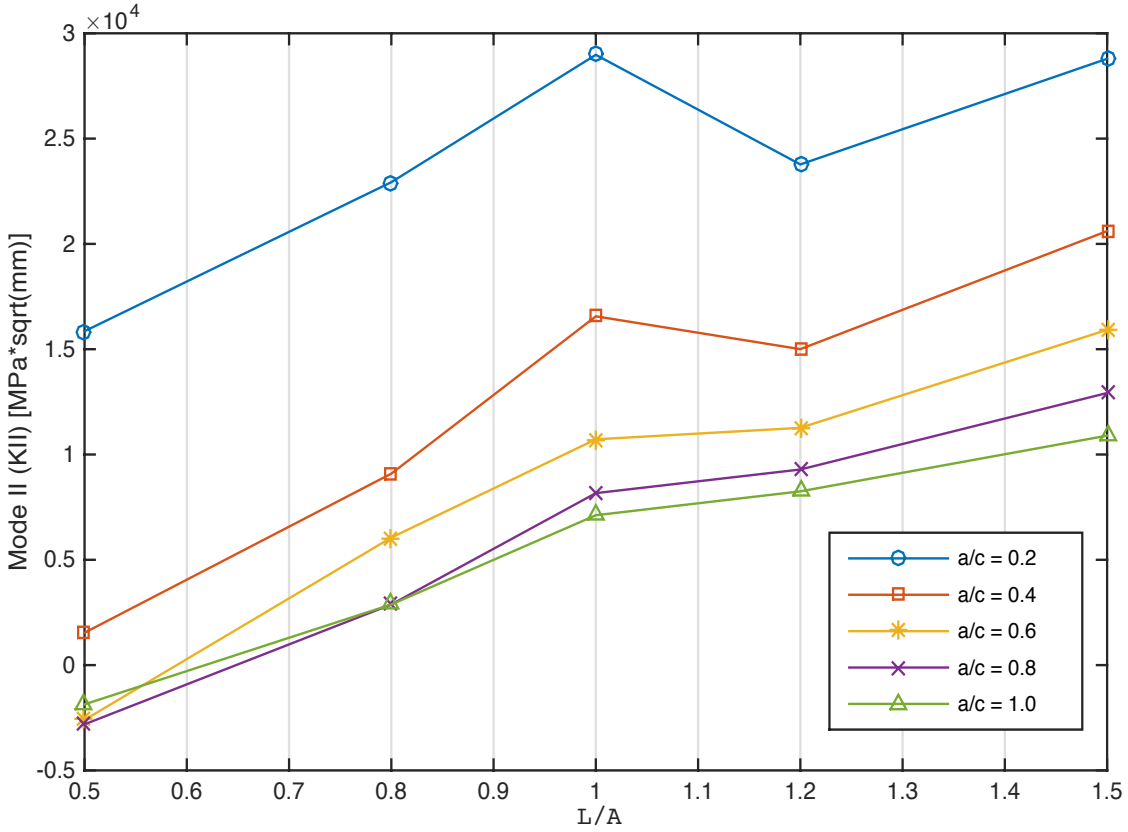

Figure 3.26 Mode II SIFs versus weld leg ratio *L/A* for different crack shape ratios for shear force loading.

As shown in Figure 3.26, we see that as the weld leg ratio is increased, the mode II SIFs increase for all the different crack shape ratios. Another important observation is that for smaller crack shape ratios, the mode II SIFs are higher compared to the mode II SIFs of larger crack shape ratios. By comparing the two loading cases, for the normal loading case (see Figure 3.12), it can be seen that as the weld leg ratio is increased the mode II SIFs decrease slightly whereas

for the shear loading case, we see that as the weld leg ratio is increased the mode II SIFs increase which resembles the behavior of the mode I SIFs plot for the normal loading case for the weld leg ratio effect (see Figure 3.11). For mode III fracture, Table 3.28 and Figure 3.27 show the numerical results obtained for the weld leg ratio effect with shear load application.

Table 3.28 Mode III SIFs for weld leg ratio effect *L/A* for shear force loading.

$K_{III}\ [MPa\cdot\sqrt{mm}]$						
a/c		0.2	0.4	0.6	0.8	1.0
L/A	0.5	-9799.82	-4406.87	-4370.12	-5207.28	-5349.47
	0.8	-6606.15	-1126.52	-2134.64	-352.91	15.27
	1.0	-3222.23	4274.15	5084.81	4747.41	5294.59
	1.2	-3897.72	3381.26	5051.98	5904.96	6833.88
	1.5	678.35	7239.21	9398.21	10560.87	11295.39

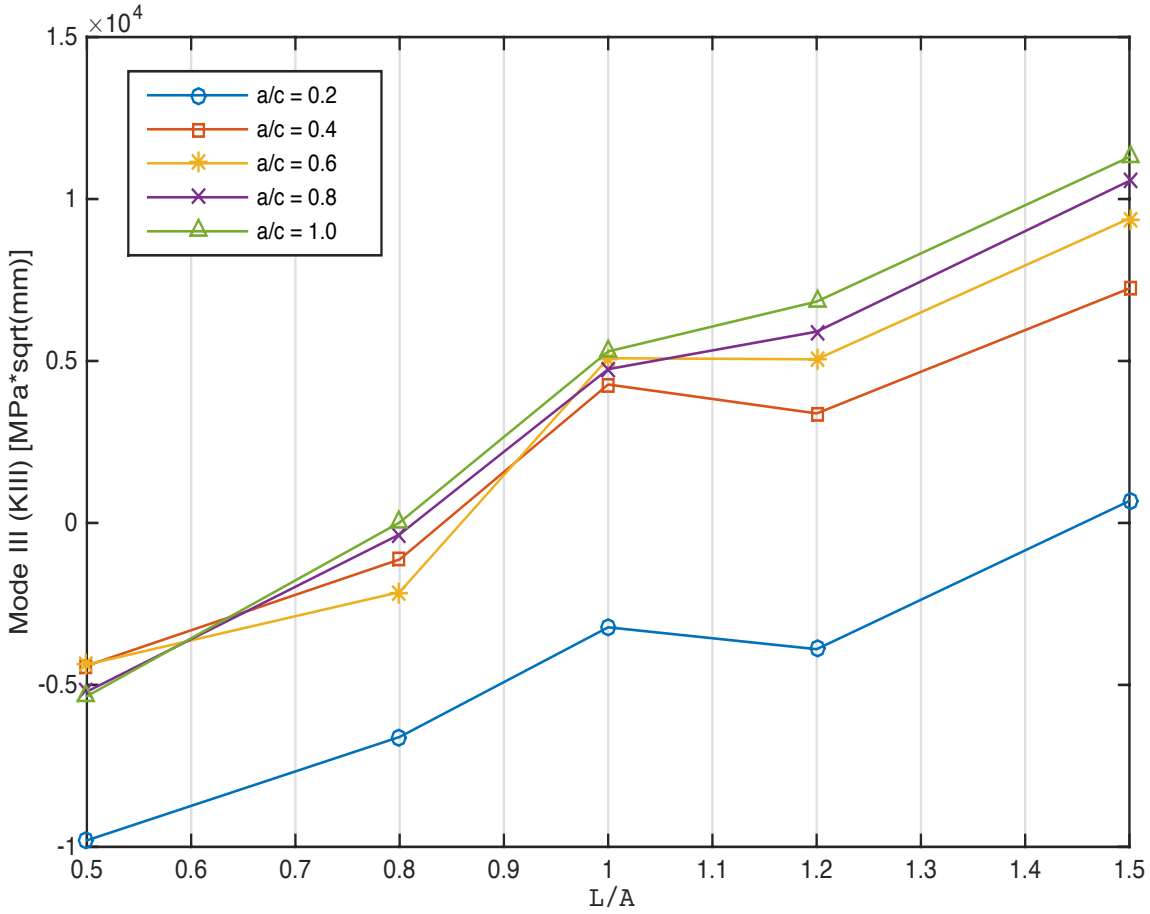

Figure 3.27 Mode III SIFs versus weld leg ratio *L/A* for different crack shape ratios for shear force loading.

By studying the mode III behavior from Figure 3.27, it can be seen that as the weld leg ratio is increased the mode III SIFs increase for the different crack shape ratios. Notice that for the mode III behavior, the larger the crack shape ratio, the higher the mode III SIFs and the opposite for the smaller crack shape ratios. The mode III facture behavior is consistent throughout for all the different geometrical variations studied for the T-butt joint, meaning larger crack shape ratios will tend to produce higher mixed-mode SIFs than smaller crack shape ratios.

3.1.9 The effect of varying the weld angle θ (Shear Force Loading)

In this section, the effect of the weld angle is studied for all the different crack shape ratios under shear load application. The FEM/BEM elements, crack shape dimensions and the fixed parameters for this case are already shown in Table 3.16. Therefore, the FEM/BEM elements are the same as before and the normal load is replaced with shear force load now. Figure 3.14 (a), Figure 3.10 (a) and Figure 3.14 (b) show the meshes for the different weld angles. Table 3.29 and Figure 3.28 show the mode I SIFs obtained for the weld angle effect θ with shear load application.

Table 3.29 Mode I SIFs for weld angle effect θ for shear force loading.

$K_I\ [MPa \cdot \sqrt{mm}]$					
a/c	0.2	0.4	0.6	0.8	1.0
θ [Degrees]					
30°	332247.15	287150.67	253824.91	232254.76	217532.83
45°	288463.21	245809.10	218676.75	200526.69	187753.89
60°	240433.27	207607.06	187368.80	170340.56	160471.71

Deducing from Figure 3.28, the mode I SIFs for the weld angle effect under shear force loading decrease as the weld angle is increased for all the different crack shape ratios. It should also be noted that smaller crack shape ratios tend to produce the highest mode I SIFs than larger crack shape ratios as is the case observed in Figure 3.28.

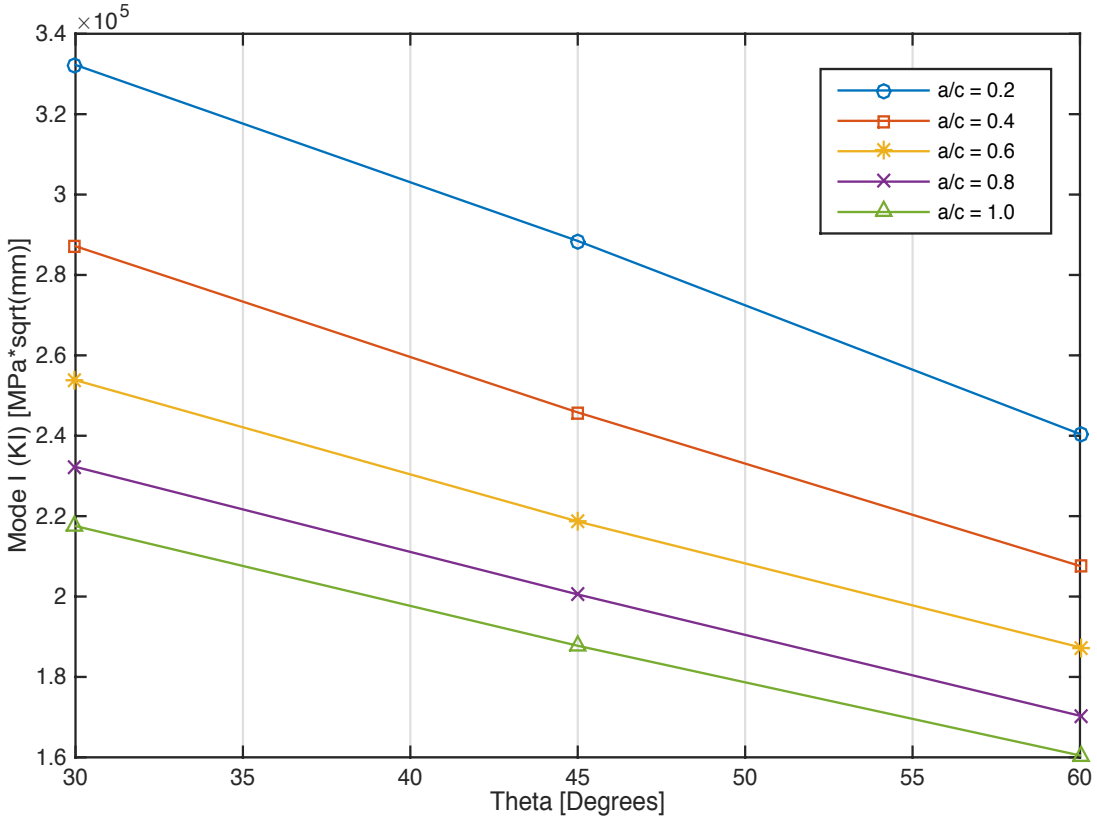

Figure 3.28 Mode I SIFs versus weld angle θ for different crack shape ratios for shear force loading.

By comparing the two different loading scenarios for mode I SIFs for the weld angle effect, it can be seen that for the normal loading case (see Figure 3.15), we see that as the weld angle is increased the mode I SIFs increase for all the different crack shape ratios whereas for the shear loading case, as the weld angle is increased, the mode I SIFs decrease. For mode II SIFs, Table 3.30 and Figure 3.29 show the numerical results obtained for the different weld angles.

Table 3.30 Mode II SIFs for weld angle effect θ for shear force loading.

$K_{II}\ [MPa \cdot \sqrt{mm}]$					
a/c	0.2	0.4	0.6	0.8	1.0
θ [Degrees]					
30°	24016.77	1930.47	-2888.02	-3731.69	-2626.68
45°	15855.13	1537.86	-2601.32	-2811.20	-1863.65
60°	16581.23	3852.93	-1964.76	-169.77	310.19

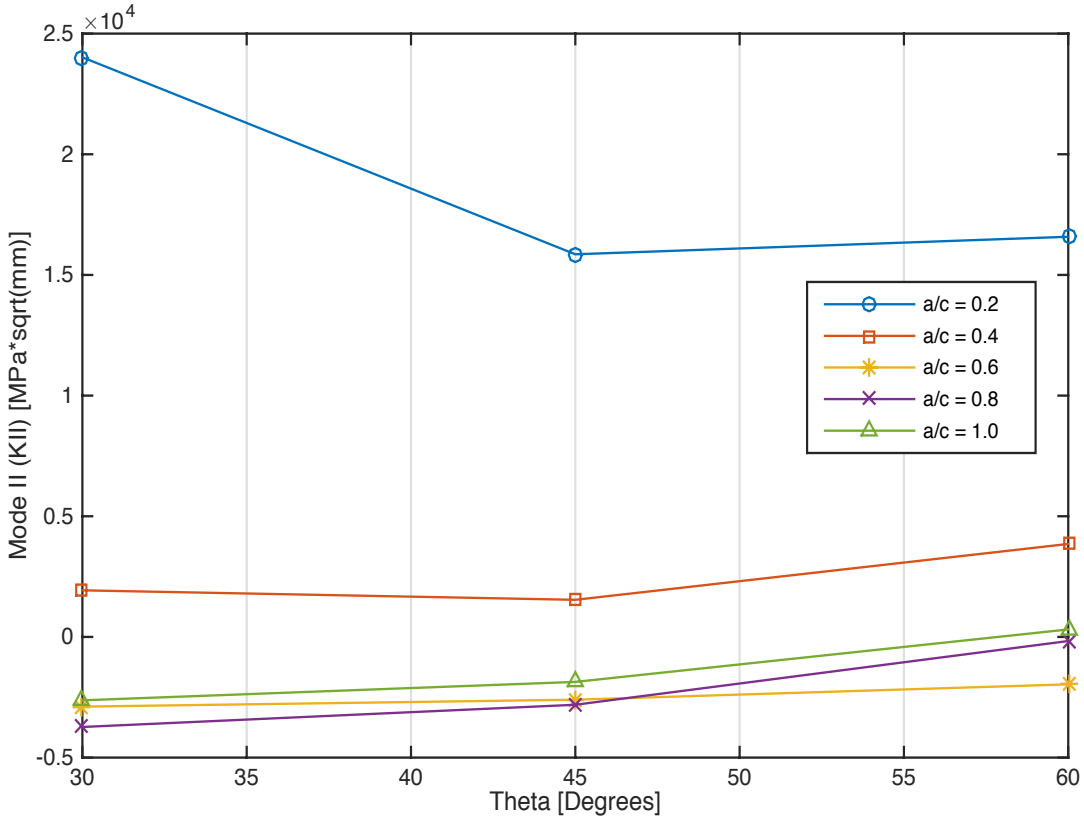

Figure 3.29 Mode II SIFs versus weld angle θ for different crack shape ratios for shear force loading.

In Figure 3.29, it can be seen that for mode II SIFs for the weld angle effect, a smaller crack shape ratio and an increasing weld angle leads to an increase in the mode II SIFs. For a larger crack shape ratio and an increasing weld angle leads to a decrease in the mode II SIFs as seen in Figure 3.29. By comparing both the shear and normal loading cases for the mode II fracture of weld angle effect, it can be seen that for the normal stress case (see Figure 3.16), the mode II SIFs decrease as the weld angle is increased for the different crack shape ratios whereas for the shear loading case there is no general trend present and it varies between the different crack shape ratios as seen above. For the last mixed mode fracture, mode III, Table 3.31 and

Figure 3.30 show the numerical results obtained for the weld angle effect of the T-butt joint subjected to shear loading.

Table 3.31 Mode III SIFs for weld angle effect θ for shear force loading.

$K_{II}\ [MPa \cdot \sqrt{mm}]$					
a/c	0.2	0.4	0.6	0.8	1.0
θ [Degrees]					
30°	-7563.59	-3465.97	-4815.39	-6806.13	-7152.17
45°	-9799.82	-4406.87	-4370.12	-5207.28	-5349.47
60°	-9316.00	-3784.90	-2842.22	-3323.05	-3154.82

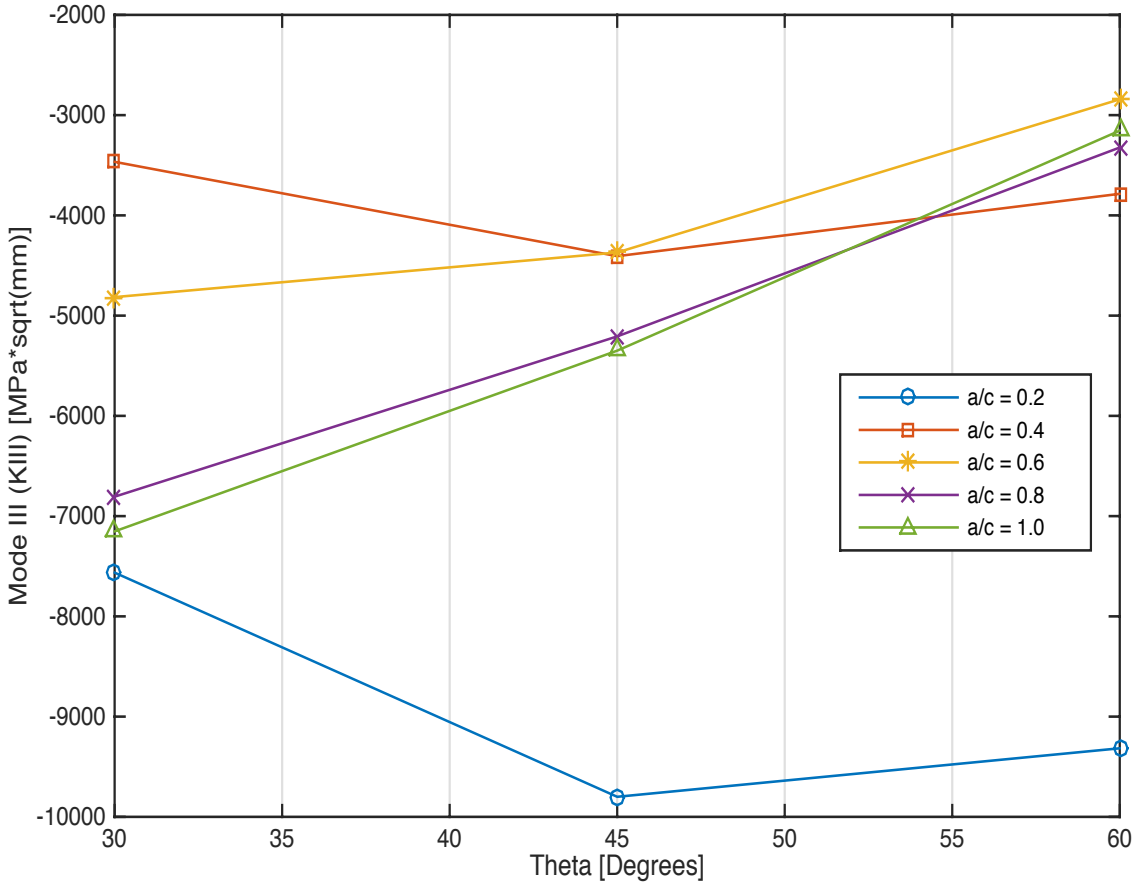

Figure 3.30 Mode III SIFs versus weld angle θ for different crack shape ratios for shear force loading.

For mode III fracture concerning the weld angle effect, it can clearly be seen that there is no general trend to describe the mode III behavior. As mentioned earlier, it should be noted that

for mode III SIFs, the smaller the crack shape ratio, the smaller the mode III SIFs whereas for increasing crack shape ratios generally leads to higher mode III SIFs. This behavior is observed throughout the mode III behavior regardless of the type of load applied and or for varying geometrical parameters. By comparing both the loading cases, it can be seen that for the normal stress loading (see Figure 3.17), there is a general trend present for the normal stress case which is that the mode III SIFs increase slightly as the weld angle is increased even if there is sudden dip for the weld angle of $\theta = 45°$ but the mode III SIFs continue to increase as the weld angle is increased. For the shear load application, there is no general trend present for the mode III fracture. For both the normal stress loading and shear stress loading cases, the mode I, II and III are SIFs highly dominant for the different geometrical cases because of the different yet pronounced trends observed for the mixed-mode SIFs. Mode II and mode III can sometimes be either positive or negative. The numerical results obtained for the mixed-mode SIFs especially for the shear loading case, negative mode II and mode III SIFs can be seen for the different geometrical parameters tested as shown in the tables above. Negative mode II and mode III SIFs simply mean that is just a matter of sign convention.

The T-butt joint weld root crack is an important analysis in this thesis. The reason is that the mixed-mode SIFs are affected by the variations in the geometry of the crack as well as the geometry of the weld toe. The effect of the crack depth ratio was mainly centered on changing the dimensions of the crack model to see how the crack propagates in the structure under different loading scenarios. As the crack depth *a* elongates in the *x*-direction, the crack length *c* will elongate in the *z*-direction. The crack length is both dependent on the crack shape ratio and the crack depth used. Larger mixed-mode SIFs for the crack depth ratio effect signifies that the joint is trying to resist fracture caused by the weld root crack which is expected since the crack is

slowly growing, the numerical plots further validate this expected behavior. The crack depth ratio effect does not require a change in the weld toe geometry as was the case for the other parameters tested, which involves altering the weld toe dimensions.

For the other parameters tested, for example, for the crack shape ratio, the weld angle was varied to study the crack shape ratio effect. For the weld leg ratio effect, the weld angle L was varied to study the impact of the weld leg ratio on the mixed-mode SIFs. To study the weld angle effect, obviously the weld angle θ had to be changed but this time with a different combination of fixed parameters for the T-butt joint. For the last three parameters tested, the weld toe geometry played a crucial role in the numerical evaluation of the mixed-mode SIFs. The reason why the weld toe geometry plays a major role is that when the rectangular base plate and rectangular vertical plate are adjoined, a single-fillet welding technique was used to construct the T-butt joint as stated earlier. The weld toe controls the outcomes of the mixed-mode SIFs under different loading cases for the weld root crack particularly because the weld toe geometry is what helps the structure resist fracture that is caused by the growing weld root crack.

As the crack propagates in both the x and z direction, the weld toe tries to maintain the contact between the base plate and the vertical plate by resisting the fracture caused by the propagating weld root crack, hence the outcome of all three dominant mixed-mode SIFs. It should also be noted that weld toe cracks can also form during the welding process for some cases and most cracks that are analyzed in the fracture and fatigue analysis of T-butt joints are due to the weld toe but in some cases weld root cracks are also possible during the same welding processes. In this numerical example, as the weld root crack propagates under different loading conditions, larger mixed-mode SIFs indicate that the structure is resisting the fracture caused by the weld root crack propagation.

3.2 Quarter-elliptical corner crack in square prismatic bar subjected to axial and torsional loading

The geometry of the square prismatic bar subjected to axial and torsional loading is shown in Figure 3.31. Six different loading scenarios are studied for the square prismatic bar and the SIFs are computed numerically using the SGBEM-FEM Alternating Method. The square prismatic bar has the following material properties: the Young's modulus is $E = 45000\ GPa$ and the Poisson's ratio is $\nu = 0.35$. A quarter-elliptical corner crack is located mid-length on one of the longitudinal edges of the square prismatic bar. Table 3.32 shows the different loading scenarios analyzed. All units of loading scenarios are given in *MPa*. The dimensions of the square prismatic bar and the quarter-elliptical corner crack are in millimeters.

Table 3.32 Axial and torsional loadings applied on the square prismatic bar.

Loading Case	*Torsion [MPa]*	*Axial [MPa]*
Case A	100	75
Case B	100	100
Case C	100	125
Case D	200	100
Case E	0	125
Case F	0	100

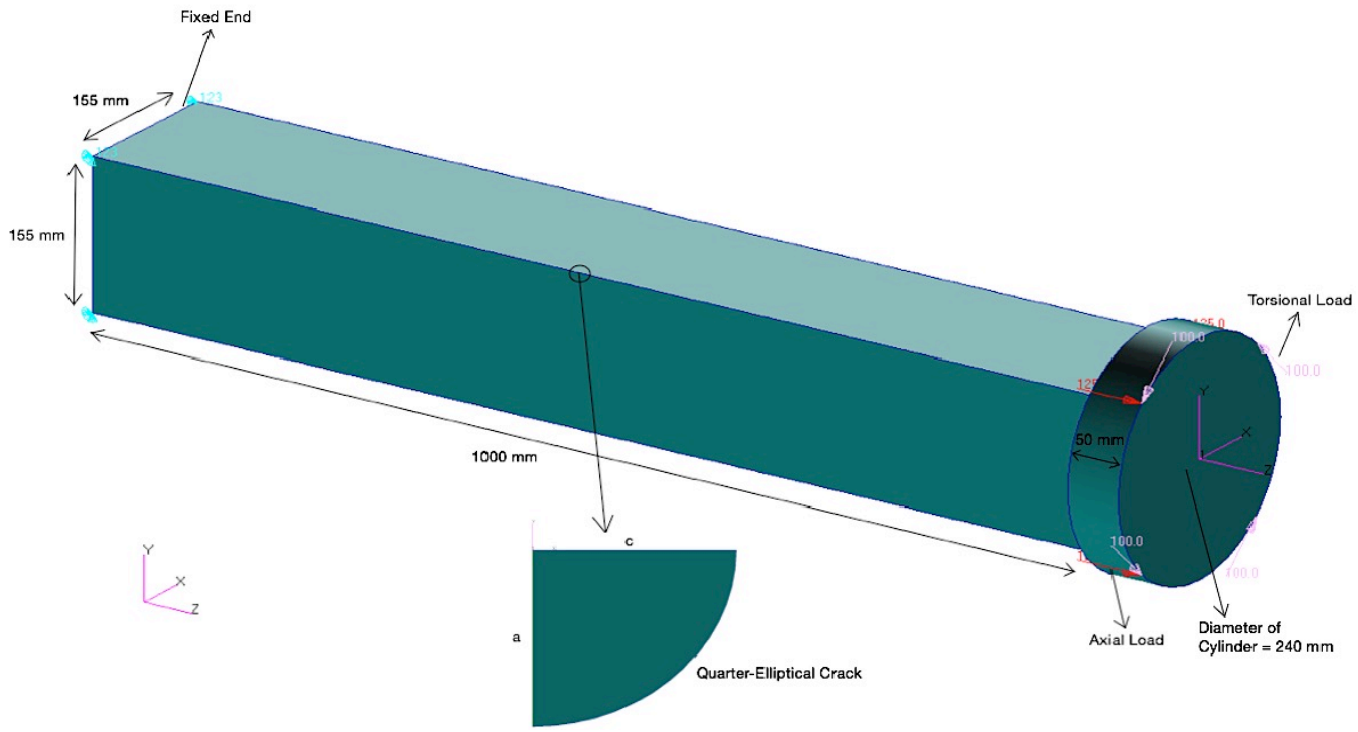

Figure 3.31 Dimensions of the square prismatic bar with quarter-elliptical corner crack subjected to axial and torsional loading.

As shown in Figure 3.31, the cylinder has a diameter $D_{Cylinder}$ = 240 mm and a height $H_{cylinder}$ = 50 mm. The length, width and height of the square bar are L = 1000 mm, W = 155 mm and $H_{square\ bar}$ = 155 mm. The quarter-elliptical corner crack has an initial crack depth of either a = 4 mm or a = 6 mm. Both crack depths are used to analyze the changes in SIFs. The FEM mesh for the un-cracked global structure and the BEM mesh for the crack surface are shown in Figure 3.32. The FEM mesh is constructed using 2912 10-noded tetrahedron elements and the BEM mesh is constructed using 8-noded quadrilateral elements. The BEM elements used for three different crack shape ratios are listed in Table 3.33 for the different initial crack depths.

Table 3.33 BEM elements for the different crack shape ratios with different crack depths.

Crack Shape Ratio	Initial Crack Depth of a = 4 mm	Initial Crack Depth of a = 6 mm
a/c = 0.66	BEM: 264	BEM: 264
a/c = 1.0	BEM: 173	BEM: 173
a/c = 1.5	BEM: 167	BEM: 167

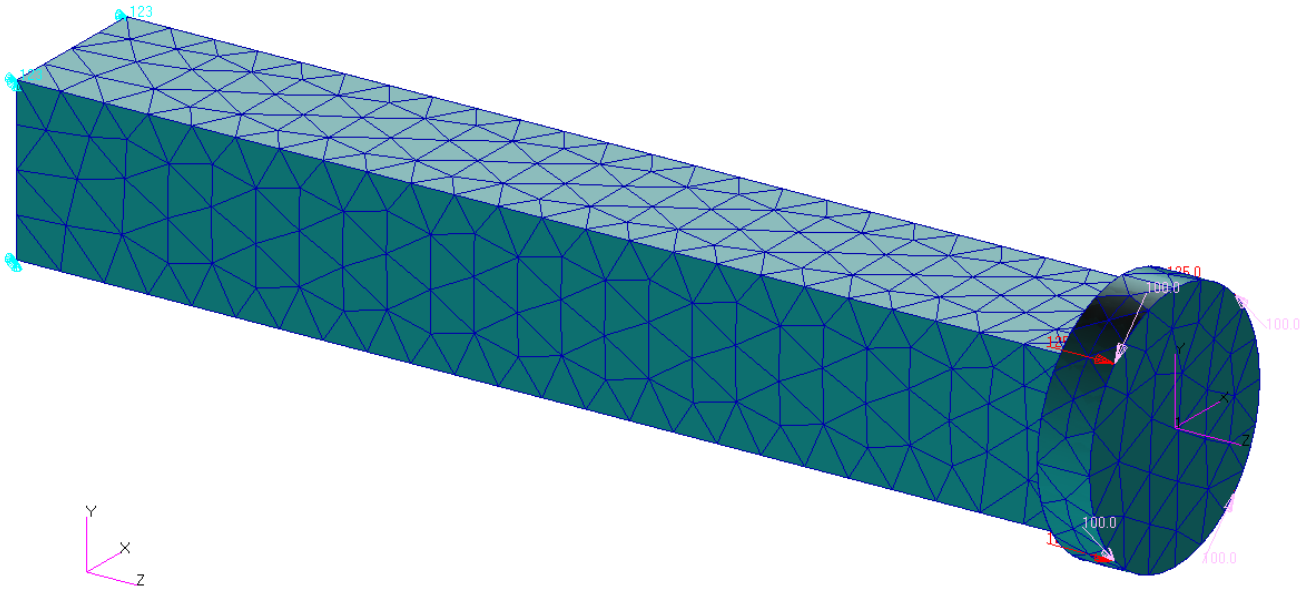

(a)

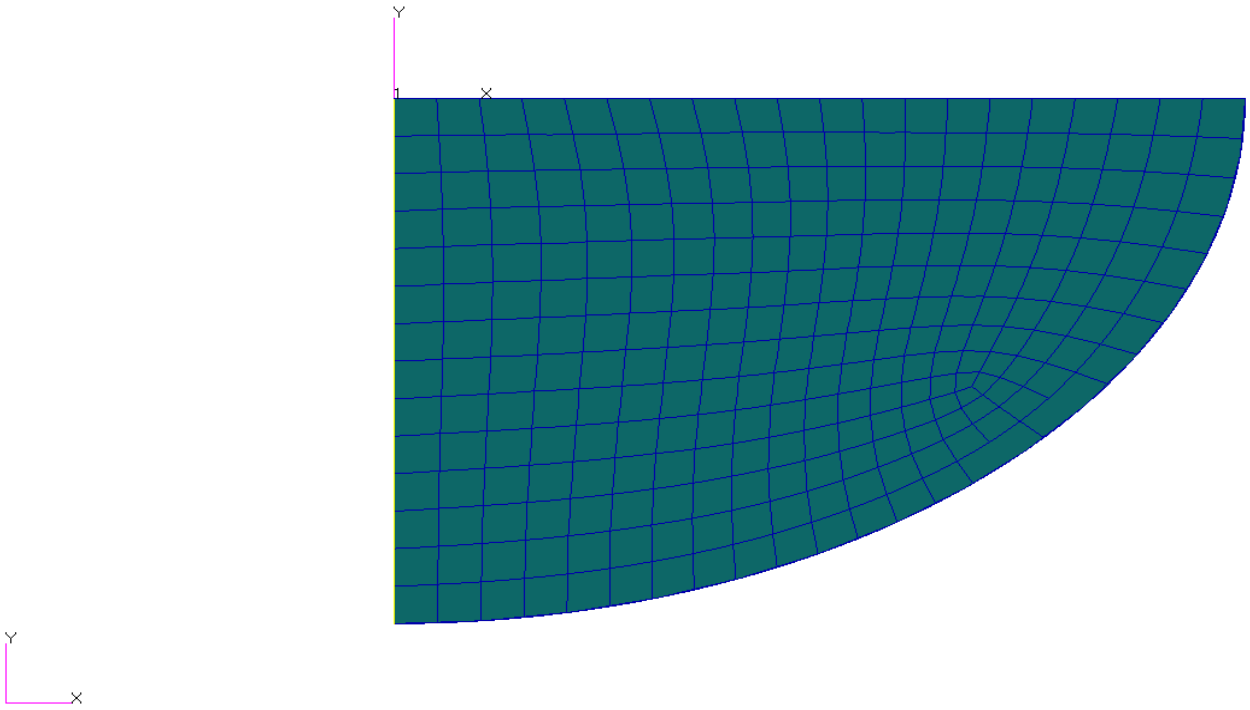

(b)

Figure 3.32 (a) Finite element mesh of un-cracked global structure modeled with 2912 10-noded tetrahedron elements, (b) Boundary element mesh for crack modeled with 8-noded quadrilateral elements (Boundary elements vary according to crack shape, see Table 3.33).

Note that the crack surface model shown in Figure 3.32 is resolved in the *x*-*y* plane, which is seen in Figure 3.32 (b). The FEM mesh is the same for all the different loading cases studied and the BEM mesh varies according to the crack shape ratio tested but notice that there is no change in the boundary elements for the different crack depths studied. The mode I SIFs and effective SIFs are plotted against the crack shape ratio for the loading cases with different initial crack depths. Table 3.34 and Figure 3.33 show the mode I SIFs obtained for the different loading cases and plotted against the crack shape ratios for an initial crack depth of a = 4 mm.

Table 3.34 Mode I SIFs for the loading cases with initial crack depth of a = 4 mm.

$K_I\ [MPa \cdot \sqrt{mm}]$						
	Case A	***Case B***	***Case C***	***Case D***	***Case E***	***Case F***
a/c						
0.66	394.55	531.41	650.15	553.69	655.26	520.68
1.0	383.50	494.84	611.76	477.79	633.12	487.10
1.5	327.93	436.85	548.46	440.20	538.97	431.31

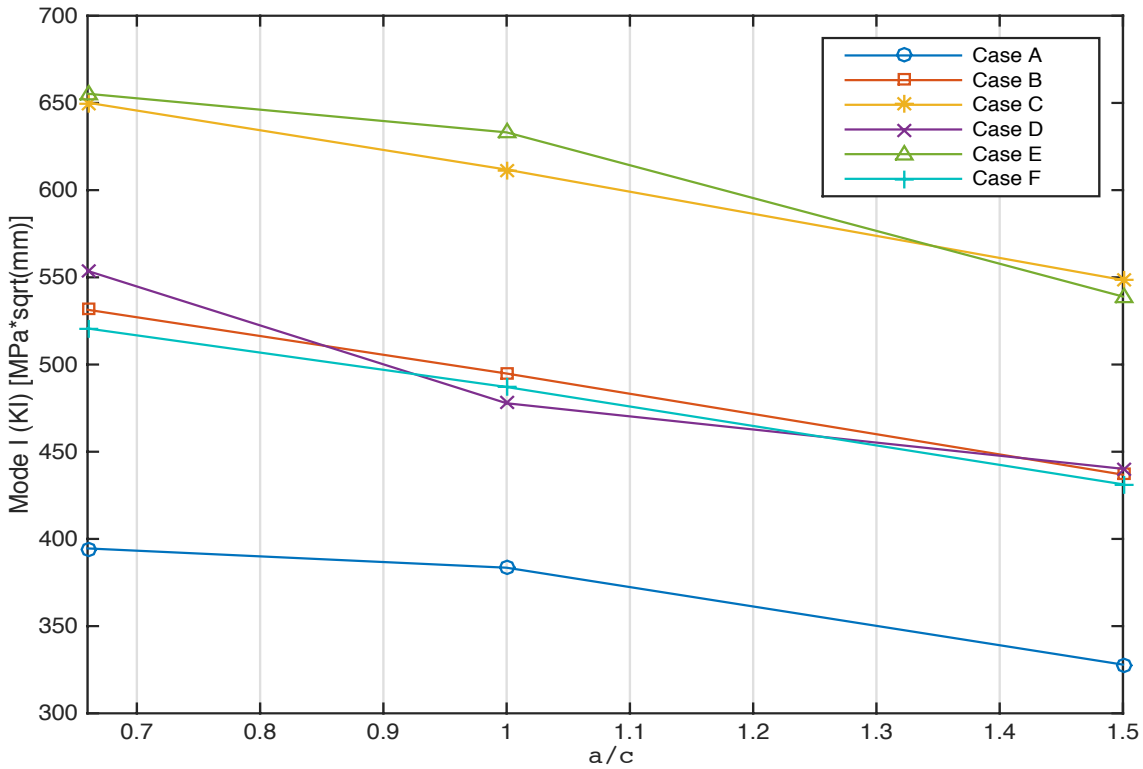

Figure 3.33 Mode I SIFs versus crack shape ratio for the loading cases with a = 4 mm.

It should be pointed out that the last two cases, Case E and Case F are purely in axial loading as shown in Table 3.32. It can be seen from Table 3.35 that the K_{eff} are the highest for Case C and Case D because Case C and D have larger combinations of axial and torsional loading than the other cases. Furthermore, Table 3.35 and Figure 3.34 show the effective stress intensity factors for an initial crack depth of a = 4 mm for the different loading cases plotted against the three crack shape ratios tested.

Table 3.35 K_{eff} for the loading cases with initial crack depth of a = 4 mm.

K_{eff} $[MPa \cdot \sqrt{mm}]$						
	Case A	***Case B***	***Case C***	***Case D***	***Case E***	***Case F***
a/c						
0.66	571.89	670.19	787.14	956.91	656.03	522.17
1.0	519.34	637.51	718.48	904.85	636.46	487.47
1.5	450.48	534.37	622.84	766.56	545.51	436.53

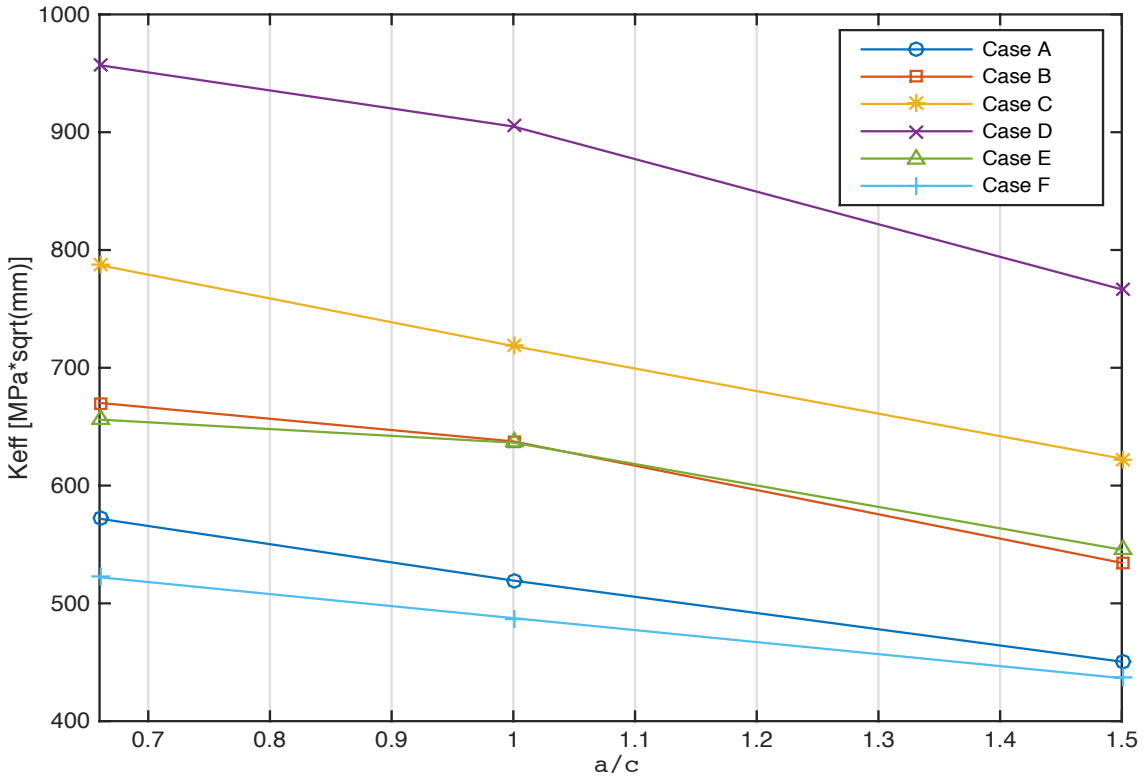

Figure 3.34 K_{eff} versus crack shape ratio for the different loading cases with an initial crack depth of a = 4 mm.

A noticeable trend for the mode I SIFs and the effective stress intensity factors with an initial crack depth of a = 4 mm is that increasing the crack shape ratio decreases the SIFs for all the different loading cases. Table 3.36 and Figure 3.35 show the mode I SIFs for an initial crack depth of a = 6 mm. For an initial crack depth of a = 6 mm, the mode I SIFs are relatively higher compared to the mode I SIFs for the initial crack depth of a = 4 mm as seen in Table 3.36 which is expected since larger crack depths tend to produce higher SIFs in general.

Table 3.36 Mode I SIFs for different loading cases for initial crack depth of a = 6 mm.

$K_I\ [MPa \cdot \sqrt{mm}]$						
	Case A	***Case B***	***Case C***	***Case D***	***Case E***	***Case F***
a/c						
0.66	507.30	656.24	847.89	629.55	802.29	684.70
1.0	512.75	569.23	841.62	707.67	750.26	600.50
1.5	392.09	529.89	663.25	522.84	666.56	534.95

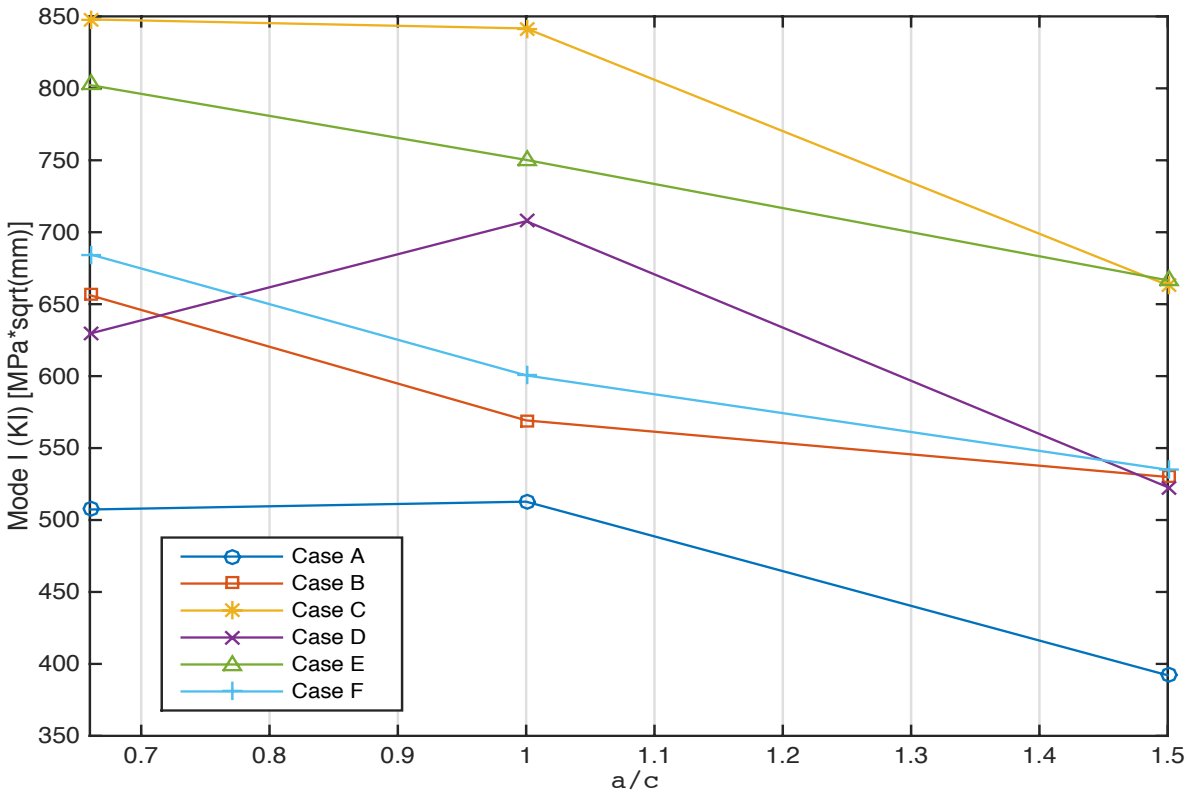

Figure 3.35 Mode I SIFs versus crack shape ratio for different loading cases with an initial crack depth of a = 6 mm.

The effective stress intensity factors are also numerically evaluated for studying the effect of the initial crack depth of a = 6 mm. Table 3.37 and Figure 3.36 show the effective stress intensity factors obtained and plotted against the three different crack shape ratios tested.

Table 3.37 K_{eff} for the different loading cases with initial crack depth of a = 6 mm.

K_{eff} $[MPa \cdot \sqrt{mm}]$						
	Case A	***Case B***	***Case C***	***Case D***	***Case E***	***Case F***
a/c						
0.66	729.08	855.19	1042.78	1232.84	802.84	735.09
1.0	695.37	779.78	1068.88	1284.36	750.57	600.68
1.5	577.64	679.97	799.33	996.83	689.23	553.04

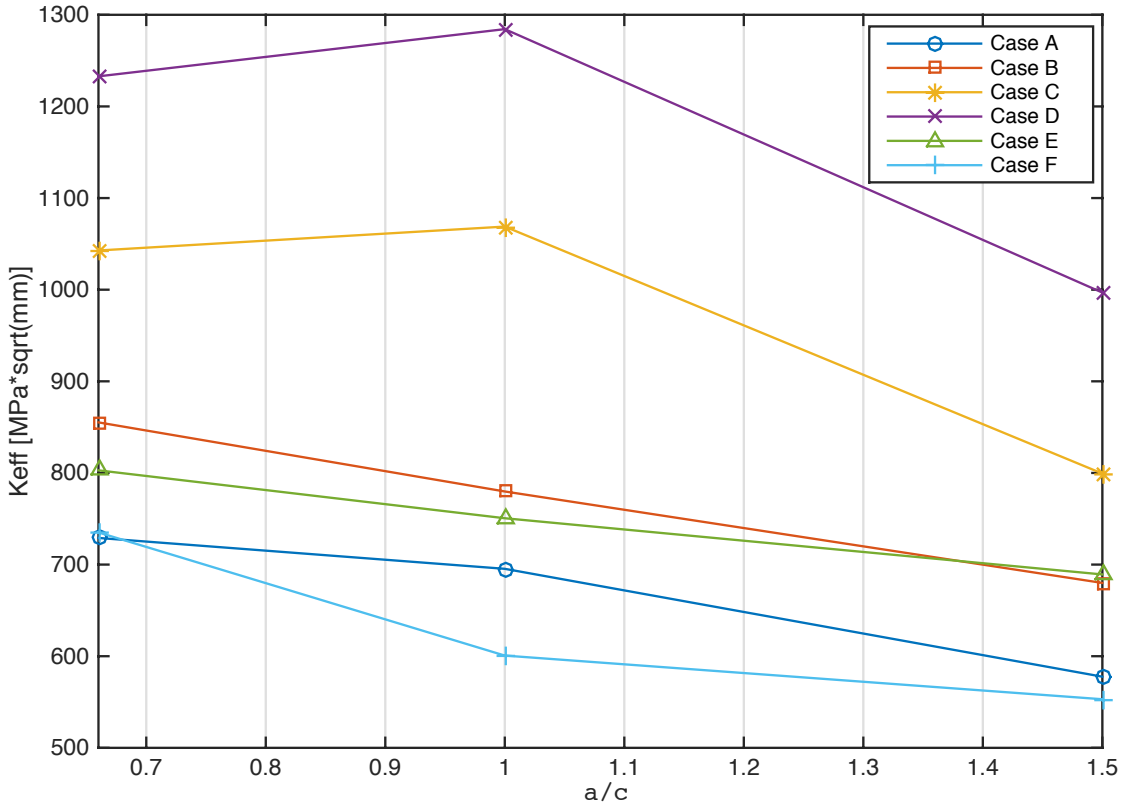

Figure 3.36 K_{eff} versus crack shape ratio for different loading cases with an initial crack depth of a = 6 mm.

From Figure 3.35, it can be seen that for mode I SIFs with an initial crack depth of a = 6 mm, as the crack shape ratio is increased, the mode I SIFs decrease for all the loading cases. It

can also be deducted from Figure 3.36 that as the crack shape ratio is increased, K_{eff} decreases for all the loading cases, which is identical to the observed behavior for an initial crack depth of a = 4 mm (see Figure 3.34). The effective stress intensity factors are also relatively higher compared to the K_{eff} of the initial crack depth of a = 4 mm. For Case C and Case D, the K_{eff} are the highest due to a combination of larger axial and torsional loading. Note that the mode II/III SIFs are not shown for this numerical example, this is because the mode II/III SIFs are very small compared to the mode I SIFs and the effective SIFs.

3.3 Slanted Edge Crack in I-Beam Subjected to Torsional Loading

In this section, an I-beam with a through-the-surface slanted edge crack will be studied for damage tolerance analysis. This I-beam numerical example is also part of the paper that has been submitted for publication to the journal of *Theoretical and Applied Fracture Mechanics* and is also part of this thesis research. The I-beam has the following material properties: Young's Modulus is $E = 206.8\ GPa$ and Poisson's ratio is $\nu = 0.29$. The through-the-surface slanted edge crack is located on the bottom flange of the beam and is slanted at a $45°$ angle. The top and bottom flanges have a thickness of 10 mm. The web has a thickness of 5 mm. The length and width of both the flanges and the web have dimensions of L = 200 mm and W = 200 mm. The top and bottom flanges are subjected to in-plane shear loads of $F = 10\ KN/m$ in opposite directions. The I-beam is fixed on one end and the application of the in-plane shear loads produces a resultant moment. The geometry of the I-beam is shown in Figure 3.37.

Two different meshes are constructed for the I-beam as shown in Figure 3.38 (a) and (b), both the meshes are coarse and the elements used are less than 5000. The crack surface meshes are shown in Figure 3.38 (c) and (d). The FEM mesh is designed using 10-noded tetrahedron elements and the BEM mesh is designed using 8-noded quadrilateral elements. The mixed-mode

and effective stress intensity factors for the I-beam are numerically computed and they are normalized and plotted against the different crack lengths a. Table 3.38 shows the mode I, mode II and the effective stress intensity factors for the I-beam with through-the-surface slanted edge crack.

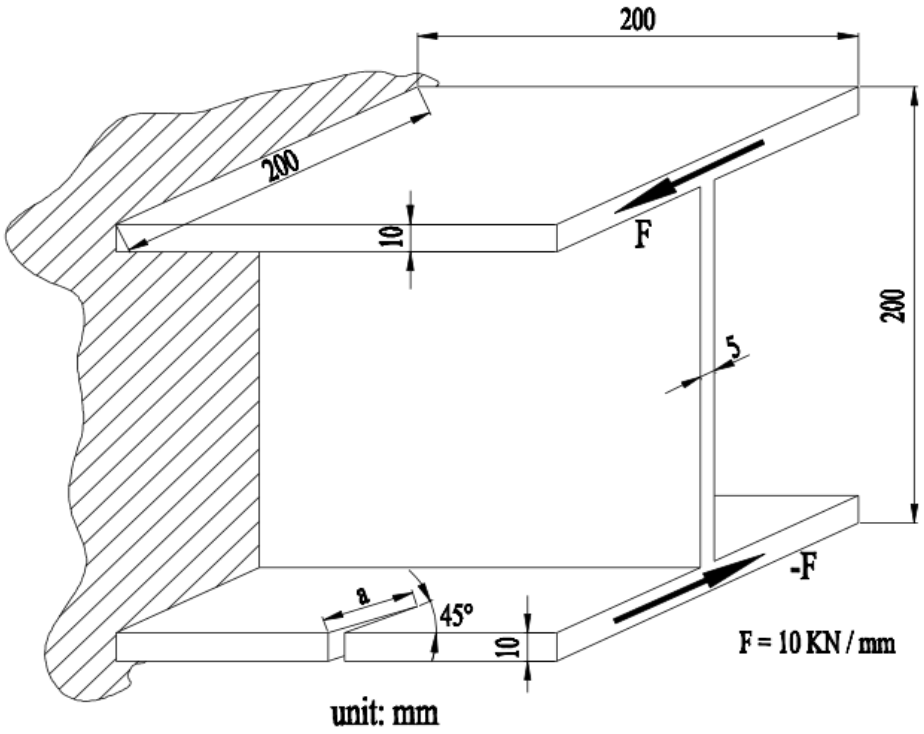

Figure 3.37 Geometry of the I-beam with through-the-surface slanted edge crack with in-plane shear loads.

A fatigue analysis is performed on the I-beam with a slanted edge crack for different initial crack lengths. The SGBEM-FEM Alternating Method is used for the simulation of the fatigue-crack-growth analyses as it is capable to assess the fatigue life of a structure using three different fatigue models such as Paris, Walker and NASGRO. For this example, Paris Law fatigue model will be used to evaluate the number of load cycles for different initial crack lengths. The material parameters for the Paris Law used for this I-beam are the following: $C = 3.6 \times 10^{-10}$, $n = 3.0$ and a stress ratio of $R = 0.10$. Two different initial crack lengths

($a_0 = 10\ mm$ and $a_0 = 40\ mm$) are tested for studying the fatigue-crack-growth analysis of the I-beam structure. Figure 3.40 (a) and (b) show the fatigue-crack-growth plotted against the number of load cycles for each initial crack length.

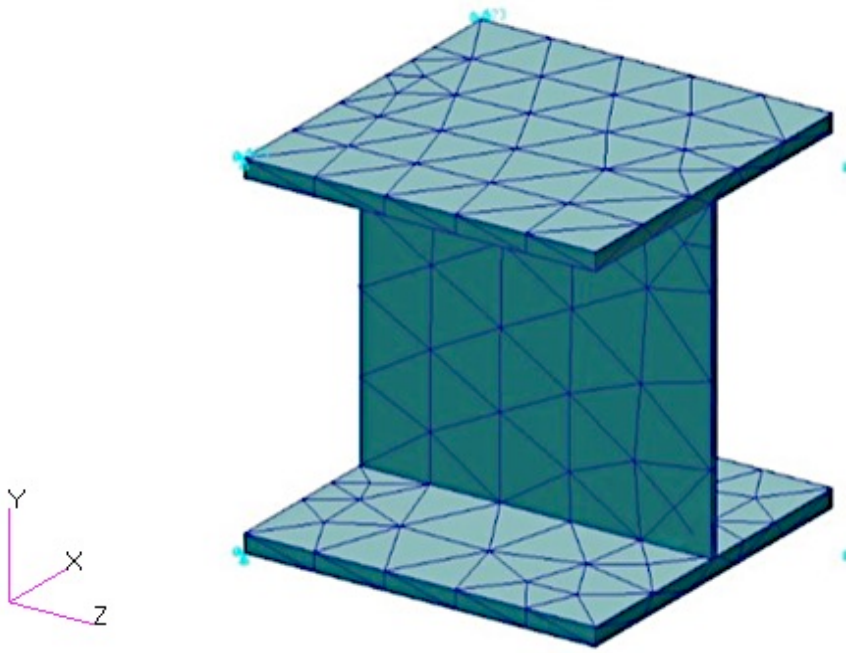

(a)

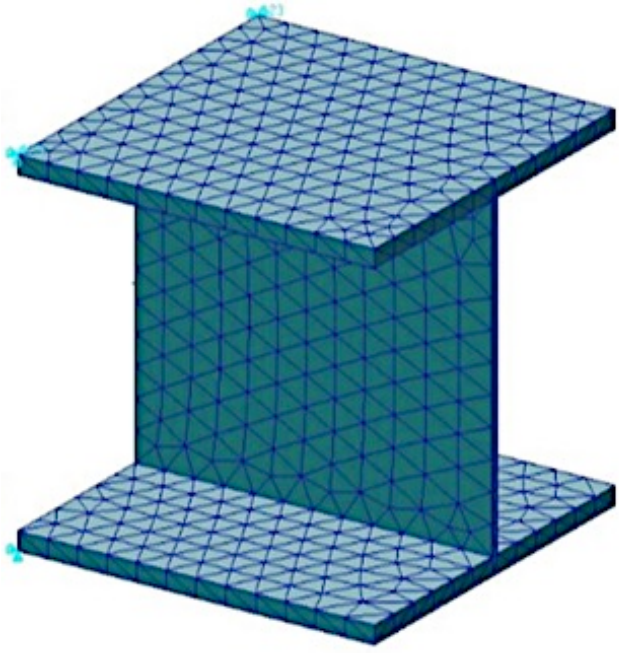

(b)

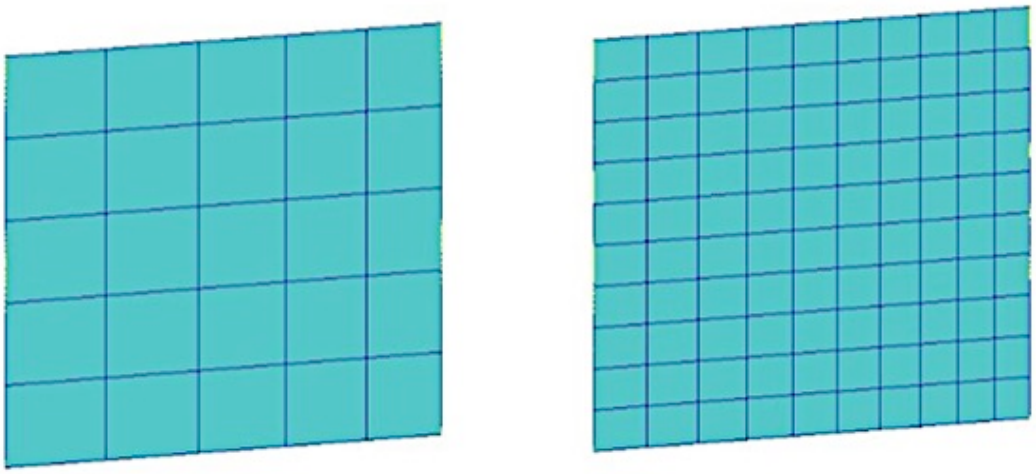

(c) (d)

Figure 3.38 (a) Finite element mesh for the un-cracked global structure modeled with 544 10-noded tetrahedron elements, (b) Finite element mesh for the un-cracked global structure modeled with 2660 10-noded tetrahedron elements, (c) Boundary element mesh for the slanted edge crack modeled with 25 8-noded quadrilateral elements for $a_0 = 10$ mm, (d) Boundary element mesh for the slanted edge crack modeled with 100 8-noded quadrilateral elements for $a_0 = 10$ mm.

The normalized mixed-mode and effective stress intensity factors are shown below for the I-beam with a slanted edge crack (see Table 3.38) for different mesh combinations with an initial crack length of a = 10 mm. Notice that a mesh combination of Figure 3.38 (b) and (c) produces the highest mixed-mode and the effective stress intensity factors whereas a mesh combination of Figure 3.38 (a) and (d) produces the lowest mixed mode and the effective stress intensity factors as shown in Table 3.38.

Table 3.38 Mixed-mode and K_{eff} SIFs for a crack length of a = 10 mm for the I-beam.

Mesh Combination	K_I	K_{II}	K_{eff}
Fig. 3.38 (a) and (c)	10796.11	5964.51	14119.99
Fig. 3.38 (b) and (d)	10907.66	6004.52	14248.38
Fig. 3.38 (a) and (d)	10618.79	5927.99	13938.81
Fig. 3.38 (b) and (c)	11098.95	6031.65	14433.79

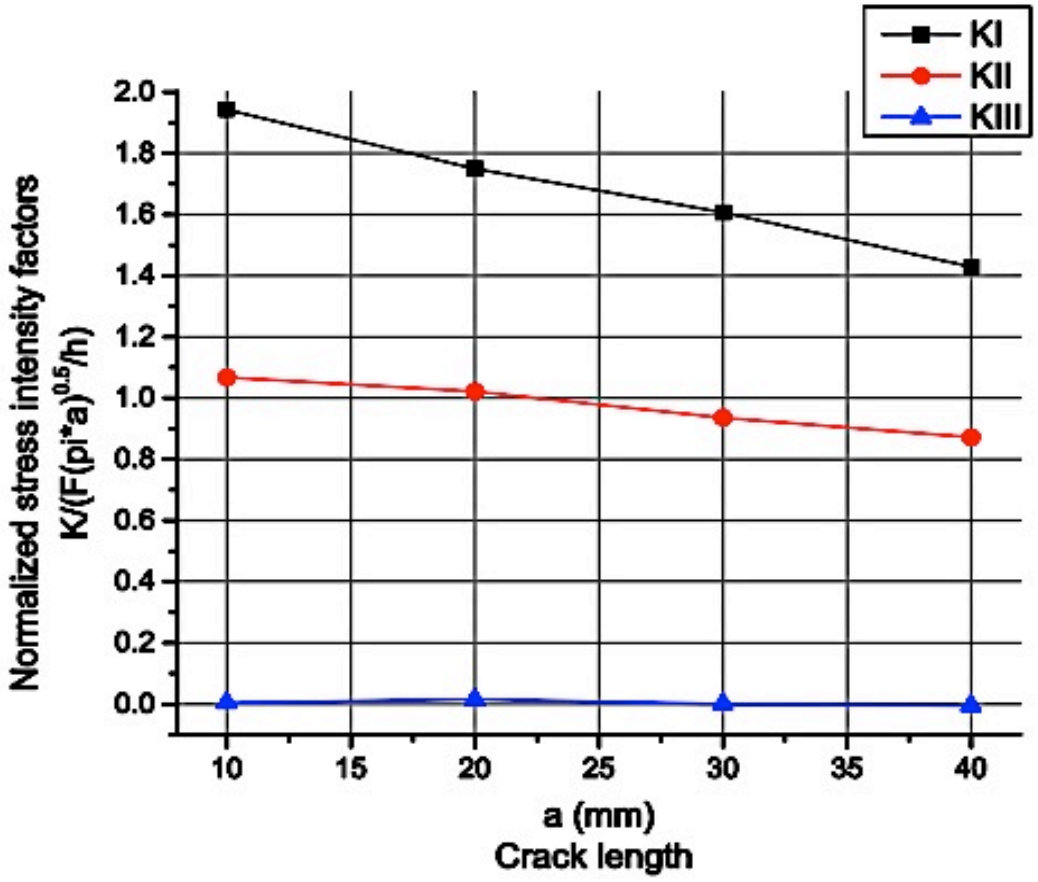

Figure 3.39 Mixed-mode normalized SIFs versus crack length for the cracked I-beam.

It can be seen from Figure 3.39 that four different initial crack lengths (a = 10 mm, 20 mm, 30 mm and 40 mm) are used to study the mixed-mode SIFs of the I-beam. The normalized SIF values for the other crack lengths are plotted in Figure 3.39. As the crack length is increased, the mode I and mode II SIFs decrease. The mode I and mode II stress intensity factors are highly dominant for the I-beam with a slanted edge crack compared to the insignificant mode III stress intensity factors.

As stated earlier, a fatigue analysis is performed for the cracked I-beam structure using the Paris Law (Eq. 8) to evaluate the fatigue-crack-growth using the SGBEM-FEM Alternating Method.

$$\frac{da}{dN} = C(\Delta K)^n \tag{8}$$

From Eq. (8), C and n are the material constants, which are 3.6×10^{-10} and 3.0 respectively, ΔK is in units of $MPa \cdot \sqrt{mm}$ and *da/dN* is the crack-growth-rate and is in units of mm/cycle. For each fatigue analysis step of the cracked I-beam, the SIFs are calculated along the crack-front by using the SGBEM-FEM Alternating Method. As stated earlier in Chapter 2, the crack-growth is modeled by adding a layer of additional elements at the crack-front to the existing crack model by using the *J*-integral as a criterion for determining the direction and magnitude of the crack advancement. To compute the fatigue life of this I-beam, Paris law from Eq.8 is used to get the following Eq. (9) for computing the number of load cycles [26], Eq. (9) is also numerically computed using the Trapezoidal rule:

$$N = \int_{a_0}^{a_f} \frac{1}{C(\Delta K)^n} da \tag{9}$$

It should be noted here that the maximum value of ΔK along the crack-front is obtained by using the SGBEM-FEM Alternating Method. Figure 3.40 (a) shows the fatigue life of the cracked I-beam structure for an initial crack length of a_0 = 10 mm and Figure 3.40 (b) shows the fatigue of the cracked I-beam structure for an initial crack length of a_0 = 40 mm.

It can be seen from Figure 3.40 (a) and (b) that for a smaller initial crack length, the fatigue life of a structure can endure more loading cycles as the crack length increases but for the case with an initial crack length of a_0 = 40 mm, as the crack length increases, the number of load cycles decreases because the initial crack length is much larger now.

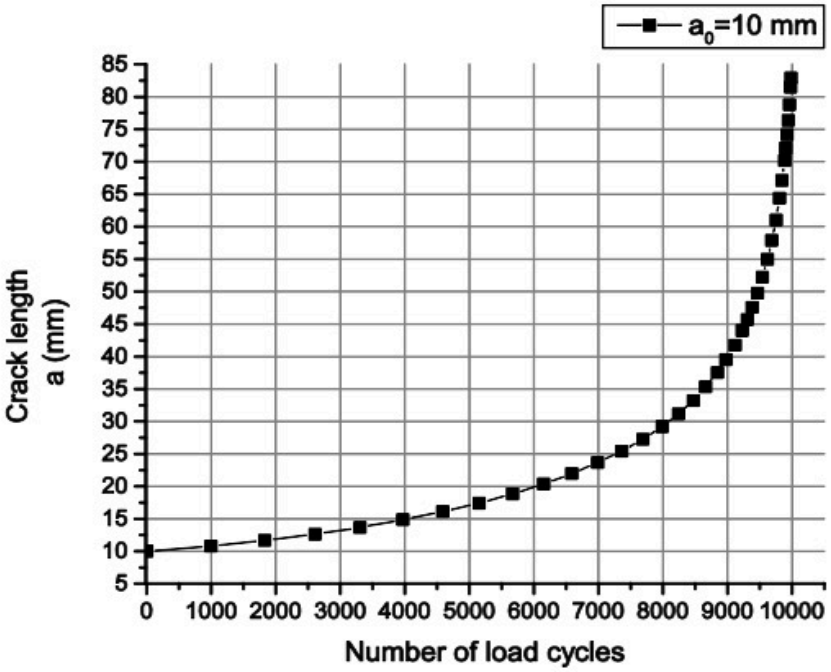

(a)

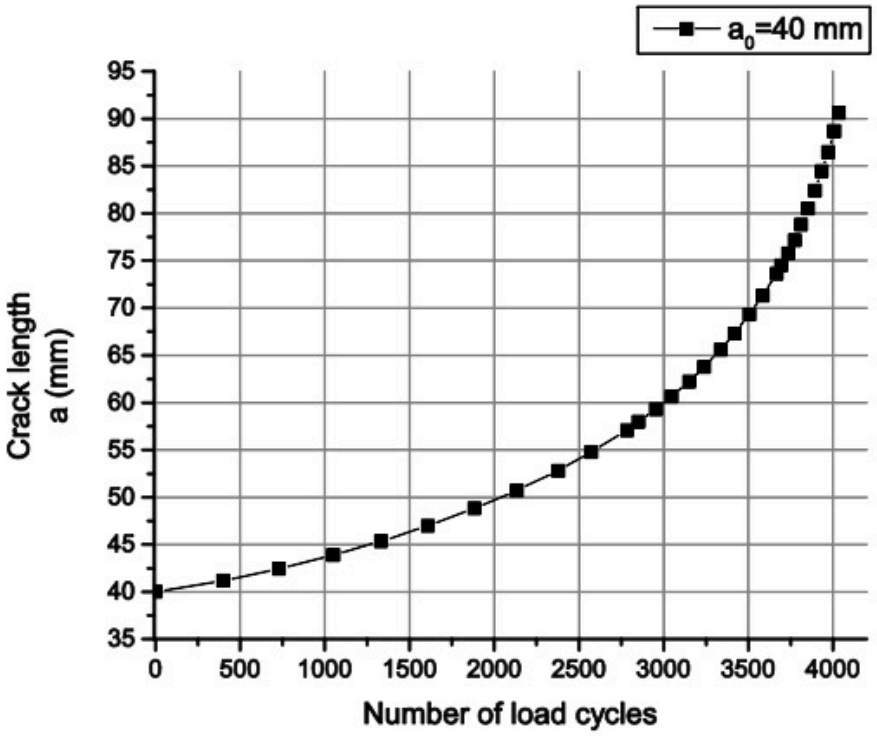

(b)

Figure 3.40 Crack length versus number of load cycles for (a) a_0 = 10 mm, (b) a_0 = 40 mm.

CHAPTER 4: CONCLUSION AND FUTURE WORK

In this thesis, several numerical examples were analyzed by employing the SGBEM-FEM Alternating Method. The SGBEM-FEM Alternating Method has several advantages that traditional Finite Element Method software lacks. Several advantages of the SGBEM-FEM Alternating Method is the ability to develop coarse meshes and obtain mixed-mode SIFs with accuracy compared to very fine meshes produced by traditional FEM software. Another advantage that makes the SGBEM-FEM Alternating Method more preferable over traditional FEM and dual BEM methods is that one can simply model the Finite element (un-cracked global structure) and Boundary element (crack surface) independently where most traditional FEM softwares lack this option.

When designing the 3D complex structures, it is crucial to treat the sharp edges and corners but with SGBEM-FEM Alternating Method, the sharp edges and corners can be avoided and the meshes do not have to be refined constantly for fracture mechanics analysis. Though there are several advantages of the SGBEM-FEM Alternating Method, there is also a downside for using this computational method. The SGBEM-FEM Method cannot be used to simulate 3D complex on a large multi-scale basis. The reason for this is because of the fully-populated coefficient matrix for the SGBEM as stated earlier in theory and formulation section of the SGBEM-FEM Alternating Method.

The numerical examples that were studied in this paper do not have empirical solutions that were readily available in the open literature. Therefore, by using the SGBEM-FEM Alternating Method to numerically evaluate the mixed-mode SIFs and estimating the fatigue life of the complex structures can serve as a reference for future studies involving the study of fracture and fatigue analyses of 3D complex structures. One of the simple advantages of using

the SGBEM-FEM Alternating Method that goes unnoticed most of the time is how fast the results are generated for pre-processing and post-processing analysis. General FEM software takes days to get a decent set of computational results whereas for the SGBEM-FEM Alternating Method, the results are produced in just matter of seconds for the fracture and fatigue analyses.

For future work, the idea is to expand the scope of using the SGBEM-FEM Alternating Method to multifunctional materials and smart structures and not just limited to simple isotropic materials. Currently, research is being conducted to expand the scope of SGBEM-FEM Alternating Method to understand the complex structures that are constructed by using multifunctional materials. An example for future studies could be such as understanding the nature of a composite wing with non-planar fatigue crack growth for future fracture and fatigue analyses of advanced aircraft structures that employ the use of multifunctional materials and smart materials. Another future study could be to understand the failure and fatigue of composite structures under different loading conditions for advanced aircraft structures using the SGBEM-FEM Alternating Method. Current FEM softwares are still used today but they do not always produce accurate results compared to the SGBEM-FEM Alternating Method.

REFERENCES

[1] Cisilino, A.P. and Aliabadi, M.H. (1999): Three- dimensional boundary element analysis of fatigue crack growth in linear and non-linear fracture problems. Engineering Fracture Mechanics, vol. 63, pp. 713-733.

[2] Mi, Y. and Aliabadi, M.H. (1994): Three-dimensional crack growth simulation using BEM. Computers & Structures, vol. 52, pp. 871-878.

[3] Bonnet, M., Maier, G., Polizzotto, C. (1998): Symmetric Galerkin boundary element methods. Applied Mechanics Reviews, vol. 51, pp. 669-704.

[4] Atluri, S.N. (1997). Structural integrity and durability, Tech Science Press, Forsyth.

[5] Sirtori, S. (1979). General stress analysis method by means of integral equations and boundary elements. Meccanica, vol. 14, pp. 210–218.

[6] Frangi A., Novati G. (2003). BEM–FEM coupling for 3D fracture mechanics applications. Computational Mechanics, vol. 32, pp. 415-422.

[7] Hsiao G.C. (1990). The coupling of boundary element and finite element methods. Journal of Applied Mathematics and Mechanics vol. 70, pp. 493–503

[8] Hsiao G.C., Khoromsky B.N., Wendland W.L. (2001). Preconditioning for boundary element methods in domain decomposition. Engineering Analysis with Boundary Elements, vol. 25, pp. 323–338

[9] Rungamornrat J. and Mear M.E. (2010). SGBEM–FEM coupling for analysis of cracks in 3D anisotropic media. International Journal for Numerical Methods in Engineering, vol. 86, pp. 224-248

[10] E.P. Stephan and W.L. Wendland (1990). A hypersingular boundary integral method for two-dimensional screen and crack problem. Archive for Rational Mechanics and Analysis, vol. 42, pp. 363-390.

[11] Frangi A, Novati G, Springhetti R, Rovizzi M. (2002). 3D fracture analysis by the symmetric Galerkin BEM. Computational Mechanics, vol. 28, pp. 220-232.

[12] Nikishkov, G. P., Park, J. H., and Atluri, S. N. (2001). SGBEM-FEM alternating method for analyzing 3D non-planar cracks and their growth in structural components. CMES: Computer Modeling in Engineering & Sciences, vol. 2, pp. 401-422.

[13] L. Tian, L. Dong, S. Bhavanam, N. Phan, S.N. Atluri, Mixed-Mode Fracture & Non-Planar Fatigue Analyses of Cracked I-beams, using a 3D SGBEM-FEM Alternating Method, Theoretical and Applied Fracture Mechanics (2014), doi: http://dx.doi.org/10.1016/j.tafmec. 2014.10.002

[14] P. Tong, T. H. H. Pian and S. J. Lasry (1973). A hybrid-element approach to crack problems in plane elasticity. International Journal for Numerical Methods in Engineering, vol. 7, pp. 297-308.

[15] S. N. Atluri, A. S. Kobayashi, and M. Nakagaki (1975). An assumed displacement hybrid finite element model for linear fracture mechanics. International Journal of Fracture, vol. 11, pp. 257-271.

[16] Henshell, R. D. and Shaw, K. G. (1975). Crack tip finite elements are unnecessary. International Journal for Numerical Methods in Engineering, vol. 9, pp. 495-507.

[17] Barsoum, R.S. (1976). Application of Triangular Quarter-Point Elements as Crack Tip Elements of Power Law Hardening Material. International Journal of Fatigue, vol. 12, pp. 463-446.

[18] Dong, L., and Atluri, S. N. (2012). SGBEM (Using Non-hyper-singular Traction BIE), and Super Elements, for Non-Collinear Fatigue-growth Analyses of Cracks in Stiffened Panels with Composite-Patch Repairs. CMES: Computer Modeling in Engineering & Sciences, vol. 89, pp. 417-458.

[19] Dong, L., Atluri, S. N. (2013a). SGBEM Voronoi Cells (SVCs), with Embedded Arbitrary-Shaped Inclusions, Voids, and/or Cracks, for Micromechanical Modeling of Heterogeneous Materials. CMC: Computers, Materials & Continua, vol. 33, pp. 111-154.

[20] Dong, L. T., and Atluri, S. N. (2013b). Fracture & Fatigue Analyses: SGBEM-FEM or XFEM? Part 1: 2D Structures. CMES-Computer Modeling in Engineering & Sciences, vol. 90, pp. 91-146.

[21] Dong, L. T., and Atluri, S. N. (2013c). Fracture & Fatigue Analyses: SGBEM-FEM or XFEM? Part 2: 3D Solids. CMES-Computer Modeling in Engineering & Sciences, vol. 90, pp. 379-413.

[22] Han, Z. D., and Atluri, S. N. (2003). On Simple Formulations of Weakly-Singular Traction & Displacement BIE, and Their Solutions through Petrov-Galerkin Approaches. CMES: Computer Modeling in Engineering & Sciences, vol. 4, pp. 5-20.

[23] Han, Z. D., and Atluri, S. N. (2007). A systematic approach for the development of weakly-singular BIEs. CMES: Computer Modeling in Engineering & Sciences, vol. 21, pp. 41-52.

[24] Okada, H., Rajiyah, H., and Atluri, S. N. (1988). A Novel Displacement Gradient Boundary Element Method for Elastic Stress Analysis with High Accuracy. Journal of Applied Mechanics, vol. 55, pp. 786-794.

[25] Okada, H., Rajiyah, H., and Atluri, S. N. (1989). Non-hyper-singular integral representations for velocity (displacement) gradients in elastic/plastic solids (small or finite deformations). Computational Mechanics, vol. 4, pp. 165-175.

[26] Paris, P.C., and Erdogan, F.A. (1963). A critical analysis of crack propagation laws. Journal of Fluids Engineering, vol. 85, pp. 528-533.